Stratospheric ozone and temperature evolution over the past decades

Lukas Brunner

August 2014

Wegener Center

UNI GRAZ

The **Wegener Center for Climate and Global Change** combines as an interdisciplinary, internationally oriented research institute the competences of the University of Graz in the research area "Climate, Environmental and Global Change". It brings together, in a dedicated building close to the University central campus, research teams and scientists from fields such as geo- and climate physics, meteorology, economics, geography, and regional sciences. At the same time close links exist and are further developed with many cooperation partners, both nationally and internationally. The research interests extend from monitoring, analysis, modeling and prediction of climate and environmental change via climate impact research to the analysis of the human dimensions of these changes, i.e., the role of humans in causing and being effected by climate and environmental change as well as in adaptation and mitigation. (more information at www.wegcenter.at)

Alfred Wegener (1880-1930), after whom the Wegener Center is named, was founding holder of the University of Graz Geophysics Chair (1924-1930). In his work in the fields of geophysics, meteorology, and climatology he was a brilliant scientist and scholar, thinking and acting in an interdisciplinary way, far ahead of his time with this style. The way of his ground-breaking research on continental drift is a shining role model—his sketch on the relations of continents based on traces of an ice age about 300 million years ago (left) as basis for the Wegener Center Logo is thus a continuous encouragement to explore equally innovative ways:
paths emerge in that we walk them (Motto of the Wegener Center).

Wegener Center Verlag • Graz, Austria

ISBN 978-3-9503608-6-8

August 2014

Contact: Lukas Brunner, MSc
lukas.brunner@edu.uni-graz.at

Wegener Center for Climate and Global Change
University of Graz
Brandhofgasse 5
A-8010 Graz, Austria
www.wegcenter.at

Master's thesis
to obtain the degree Master of Science
at the University of Graz

Stratospheric ozone and temperature evolution over the past decades

Lukas Brunner

August 9, 2014

Supervisor:

Priv.-Doz. Dr.rer.nat. Andrea K. Steiner

Co-supervisor:

Dr.rer.nat. Barbara Scherllin-Pirscher

Wegener Center for Climate and Global Change
University of Graz

Abstract

Investigating ozone and temperature related processes in the stratosphere is crucial for our understanding of the Earth's climate system. In recent decades satellite-based remote sensing has created new opportunities to measure physical properties of the free atmosphere with global coverage. Stratospheric ozone has been closely investigated since the postulation of anthropogenic induced ozone loss in the 1970s. The emission restrictions for ozone depleting substances implemented by the Montreal Protocol started to omit further ozone loss in the 1990s. Ozone and temperature evolution in the stratosphere are closely connected. The stratospheric temperature structure is mainly determined by the ozone concentration. But temperature changes also feed back, influencing ozone variability.

In this thesis stratospheric ozone evolution from three observational data sets, covering in total 34 years from 1979 to 2012, is investigated. Corresponding temperature changes are derived from radiosonde and GPS Radio Occultation (RO) measurements, covering 1979 to 2012 and 2002 to 2012, respectively. For comparison also ERA-Interim reanalysis fields for both, ozone and temperature are considered for 1979 to 2102. All data sets have high vertical resolution within the stratosphere allowing for distinction of trends in different altitudes.

Three different time periods are investigated, using multiple linear regression to separate trend signals from natural variability, accounting for El Niño–Southern Oscillation, the Quasi-Biennial Oscillation, and solar flux variations. From 1979 to 1996 decreasing ozone concentrations and statistically significant cooling are found in large regions of the stratosphere. For the period 1997 to 2012 ozone shows signs of recovery especially in mid latitudes, mitigating further cooling in most of the stratosphere. In the period 2002 to 2012, with RO data availability, no significant trends are found due to the large natural variability.

Zusammenfassung

Detaillierte Untersuchungen von Ozon und Temperatur in der Stratosphäre sind von entscheidender Bedeutung für unser Verständnis des globalen Klimasystems. In den letzten Jahrzehnten hat die satellitengestützte Fernerkundung neue Möglichkeiten eröffnet physikalische Größen in der freien Atmosphäre mit globaler Abdeckung zu messen.

Seit der Postulation von anthropogen verursachter Ozonzerstörung in den 1970er Jahren wurde insbesondere stratosphärisches Ozon intensiv beobachtet. Die Emissionsbeschränkungen mit denen Ozon zerstörende Substanzen im Zuge des Montreal Protokolls belegt wurden, verhinderten eine weitere Reduktion der Ozonkonzentration ab Mitte der 90er Jahre. Die stratosphärische Temperatur ist eng mit Ozon verknüpft, da Absorption von Strahlung durch Ozon die wichtigste Wärmequelle in der Stratosphäre darstellt. Andererseits beeinflussen Temperaturänderungen durch Rückkopplungen auch den Ozonzyklus.

Diese Arbeit untersucht die Entwicklung von stratosphärischem Ozon von 1979 bis 2012 basierend auf drei Beobachtungsdatensätzen. Die Temperaturdaten stammen von Radiosonden- (1979 bis 2012) und GPS Radiookkultationsmessungen (2002 bis 2012). Für einen weiteren Vergleich werden auch Ozon und Temperatur Reanalysen von ERA-Interim im gesamten Zeitraum untersucht. Alle Datensätze haben eine hohe vertikale Auflösung, was eine Unterscheidung von Trends in verschiedenen Höhen ermöglicht.

Mittels multipler linearer Regression werden in drei Zeitperioden Trends von natürlicher Variabilität, wie ENSO, QBO und Sonnenzyklus, getrennt. Von 1979 bis 1996 sank die Ozonkonzentration ebenso wie die Temperatur in weiten Teilen der Stratosphäre. Für den Zeitraum von 1997 bis 2012 zeigt Ozon Zeichen von Regeneration, insbesondere in mittleren Breiten was eine weitere Abkühlung der Stratosphäre größtenteils verhindert. Von 2002 bis 2012 wurden aufgrund der hohen natürlichen Variabilität keine statistisch signifikanten Trends gefunden.

Acknowledgments

Contents

Contents

Acronyms

ACE-FTS Atmospheric Chemistry Experiment–Fourier Transform infrared Spectrometer.

AEM-B Applications Explorer Mission-B.

BDC Brewer-Dobson Circulation.

CCI Climate Change Initiative.

CFC ChloroFluoroCarbon.

CHAMP CHAllenging Minisatellite Payload.

CLIPS2 CLImatology Processing System 2.

CPG Common Pressure Grid.

DOF Degrees Of Freedom.

DU Dobson Unit.

ECMWF European Centre for Medium-Range Weather Forecasts.

ENSO El Niño–Southern Oscillation.

ERA-Interim ECMWF ReAnalysis-Interim.

ERBS Earth Radiation Budget Satellite.

ESA European Space Agency.

EV Explained Variance.

F3C FORMOSAT-3/COSMIC.

GES DISC Goddard Earth Sciences Data and Information Services Center.

GHG GreenHouse Gas.

GOMOS Global Ozone Monitoring by Occultation of Stars.

Acronyms

GOZCARDS Global OZone Chemistry And Related trace gas Data Records for the Stratosphere.

GPS Global Positioning System.

GRACE Gravity Recovery And Climate Experiment.

HALOE HALogen Occultation Experiment.

HARMOZ HARMonized dataset of OZone profiles.

HDF Hierarchical Data Format.

IPCC AR5 5th Assessment Report of the Intergovernmental Panel on Climate Change.

LEO Low Earth Orbit.

LOS Line Of Sight.

LS Lower Stratosphere.

MEaSUREs Making Earth Science data records for Use in Research Environments.

MIPAS Michelson Interferometer for Passive Atmospheric Sounding.

MLS Microwave Limb Sounder.

MS Middle Stratosphere.

NAN Not A Number.

NASA National Aeronautic and Space Administration.

NetCDF Network Common Data Format.

NOAA National Oceanic and Atmospheric Administration.

ODS Ozone-Depleting Substance.

OPSv5.6 Occultation Processing System version 5.6.

OSIRIS Optical Spectrograph and InfraRed Imaging System.

PSC Polar Stratospheric Cloud.

QBO Quasi-Biennial Oscillation.

RICH Radiosonde Innovation Composite Homogenization.

RO Radio Occultation.

RS RadioSonde.

RV Residual Variance.

SAGE I Stratospheric Aerosol and Gas Experiment I.

SBUV Solar Backscatter UltraViolet.

SBUV/2 Solar Backscatter UltraViolet 2.

SBUVv8.6 SBUV algorithm version 8.6.

SCIAMACHY SCanning Imaging Absorption spectroMeter for Atmospheric CHartographY.

SMR Sub-Millimetre Radiometer.

SST Sea Surface Temperature.

TP Tangent Point.

TSI Total Solar Irradiance.

TV Total Variance.

UARS Upper Atmosphere Research Satellite.

UN United Nations.

US Upper Stratosphere.

UTC Coordinated Universal Time.

UV UltraViolet.

WEGC Wegener Center for Climate and Global Change.

WMGHG Well-Mixed GreenHouse Gas.

WMO World Meteorological Organization.

Introduction

Humans have been altering the composition of the Earth's atmosphere for many decades. Even though the change in total composition may seem low, it can have potentially large impacts on the climate system. The effects highly differ depending on the atmospheric region. It is commonly known that the increase of Well-Mixed GreenHouse Gases (WMGHGs) like carbon dioxide leads to a rise of surface temperatures, as, e.g., stated by the Working Group 1 contribution to the 5th Assessment Report of the Intergovernmental Panel on Climate Change (IPCC AR5) [IPCC 2013]. But WMGHGs also contribute to the cooling of higher regions of the atmosphere like the stratosphere. The emission of Ozone-Depleting Substances (ODSs) like ChloroFluoroCarbons (CFCs) is another example of anthropogenic influence on the natural balance in the stratosphere. Decreasing ozone concentrations led to a thinning of the stratospheric ozone layer for over three decades, until emission restrictions for ODSs started to prevent further loss in the mid 1990s [WMO 2011].

Since ozone is the main heat source in the stratosphere, a temperature response follows the ozone changes. This response is not easy to detect since it is overlaid by the WMGHG response [McLandress et al. 2010]. However, single forcing model studies suggest that the Lower Stratosphere (LS) cooling is mainly caused by ozone depletion, while the WMGHG signal dominates the Upper Stratosphere (US) [Polvani and Solomon 2012].

WMGHG induced cooling in the Middle Stratosphere (MS) and US accelerates ozone recovery and alters transport mechanisms, which further complicates the attribution of both, temperature and ozone changes [Eyring et al. 2010]. Finally some observations indicate that water vapor may also play a significant role in the LS cooling [Ramaswamy et al. 2001].

In the recent past ozone-temperature connections have been increasingly investigated as stratospheric climate change and its impacts to the troposphere came more and more into focus [Baldwin et al. 2007; Hegglin and Shepherd 2009; Seidel et al. 2011; Gerber et al. 2012].

This work surveys the changes in ozone, temperature, and water vapor over the past decades. Three ozone data sets, covering a total time range of 34 years from 1979 to 2012 are used. Emphasis is given to the period 2002 to 2012, for which temperature time series from Radio Occultation (RO) are available. A second temperature data

set, based on RadioSonde (RS) measurements, is used to cover earlier years. In addition a data set covering the stratospheric water vapor content is considered. European Centre for Medium-Range Weather Forecasts (ECMWF) reanalysis fields for all three parameters are used for comparison. All data sets in this work have a high vertical resolution, which allows for a good distinction of signals from different altitudes within the stratosphere.

This work is structured as follows: Chapter 1 describes the basic structure and composition of the Earth's atmosphere. This also includes recent changes from emissions of anthropogenic trace gases, focusing on the situation in the stratosphere. Furthermore, several important chemical and dynamical features are investigated. Chapter 2 surveys satellite based remote sensing techniques for atmospheric sounding. The different instruments, delivering observations for the data sets used in this study are described. The retrieval process as well as the spatial and temporal coverage of the data is also covered in this chapter. The mathematical basis for the trend analysis is given in chapter 3. The regression model and the significance tests applied to the data are described here. Chapter 4 presents the results of the regression study as well as a detailed comparison of the different data sets. The work concludes with a discussion and a summary of the results in chapter 5.

1. The Earth's atmosphere

1.1. Composition and layering

The main components of dry air are nitrogen (N_2, 78.08 % by volume), oxygen (O_2, 20.95 %), and argon (Ar, 0.93 %). Additionally a range of trace gases is present in the atmosphere but they contribute only fractions of % to the atmospheric composition. In the lowermost part of the atmosphere water vapor (H_2O) can reach up to 5 %, while it is nearly absent in the higher regions. Because of this very unequal distribution, mixing ratios in the atmosphere are always given with respect to dry air [Wallace and Hobbs 2006].

1.1.1. Trace gases

A common way to quantify the amount of a trace gas is the *parts-per* notation, i.e., parts per million (ppm), parts per billion (ppb), parts per trillion (ppt). However, there are several problems with this notation as stated, e.g., by Schwartz and Warneck [1995]. Ambiguity can especially arise because different conventions are in use, often without being specified. The parts-per mixing ratio can be given with respect to mass, volume, or moles. Therefore the convention used in this work is clarified below.

The atmosphere is in good approximation an ideal gas and therefore follows Avogadro's law, which states that at fixed temperature T and pressure p, one mol of any ideal gas has the same volume V:

$$\frac{V}{n} = \frac{RT}{p} = \text{const.},\tag{1.1}$$

where n is the number of moles and $R = 8.3145\,\mathrm{J\,K^{-1}\,mol^{-1}}$ is the universal gas constant [Wallace and Hobbs 2006]. This allows for a direct conversion from volume fraction into mole fraction

$$\frac{n_i}{n_{\mathrm{air}}} = \frac{V_i}{V_{\mathrm{air}}}.\tag{1.2}$$

The left hand side in Eq. (1.2) denotes the ratio of moles from an atmospheric component n_i to the total number of moles n_{air} in the same air parcel, while the right

hand side gives the corresponding volume fraction. The conversion into and from mass fraction needs more information about the components involved. Following the definition by the 5th Assessment Report of the Intergovernmental Panel on Climate Change (IPCC AR5) in this work, the parts-per notation is exclusively used with respect to moles, i.e.,

$$1\,\text{ppm} \equiv 1\,\mu\text{mol}\,\text{mol}^{-1} = 10^{-6}\,\text{mol}\,\text{mol}^{-1}$$
$$1\,\text{ppb} \equiv 1\,\text{nmol}\,\text{mol}^{-1} = 10^{-9}\,\text{mol}\,\text{mol}^{-1}$$
$$1\,\text{ppt} \equiv 1\,\text{pmol}\,\text{mol}^{-1} = 10^{-12}\,\text{mol}\,\text{mol}^{-1} \tag{1.3}$$
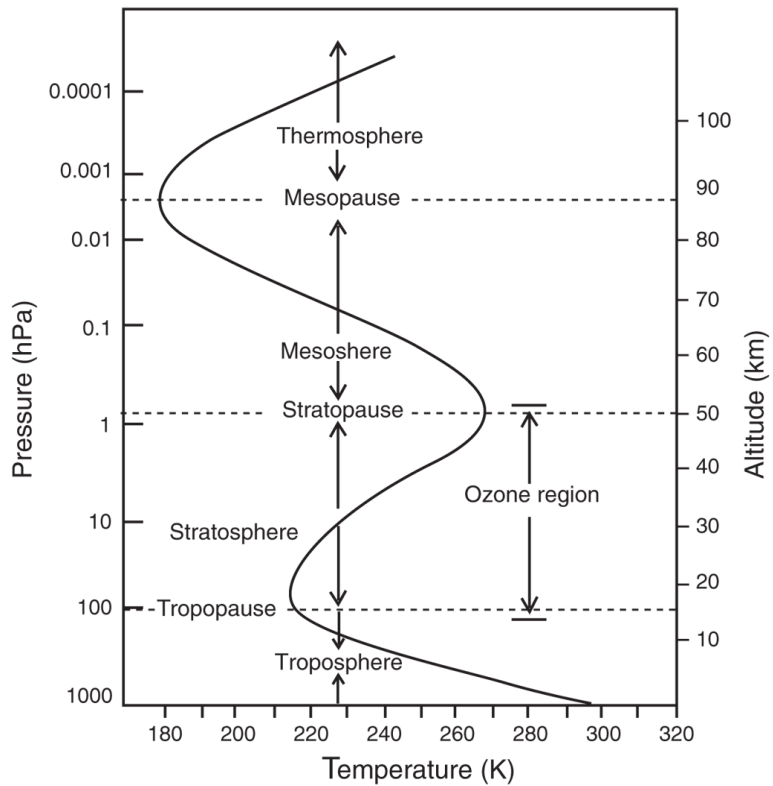
With this notation the most important trace gases with respect to their concentration in the atmosphere are carbon dioxide (CO_2) with 390.5 ppm, methane (CH_4) with 1.8 ppm, and nitrous oxide (NO_2) with 324.2 ppb as of 2011 [IPCC 2013].

1.1.2. Atmospheric layers

The major part of the constituents of dry air are well mixed below about 100 km altitude, a region called *homosphere* (in contrast to the *heterosphere* above 100 km, where the gases start to separate by molecular mass). Water vapor has already been mentioned as an example of a component which is not equally distributed and highly variable in space and time. Another prominent exception is ozone (O_3), which is most abundant in the *ozone layer* at about 30 km. Here, the concentrations reach up to 11 ppm, while near the Earth's surface mixing ratios below 100 ppb are already considered unhealthy [Weinhold 2008].

Beside the classification into homosphere and heterosphere there are also several other definitions, structuring the atmosphere into spheres. The classification due to the vertical temperature gradient leads to the most commonly know layers (Fig. 1.1). Note, that in this work the atmospheric temperature gradient will always be given from lower to higher altitudes (i.e. a negative gradient denotes a temperature decrease with height):

- The *troposphere* reaches from the surface to the tropopause at about 12 km in the global mean. Since the troposphere is heated mainly from the surface it has a negative temperature gradient of $-6\,\text{K}\,\text{km}^{-1}$ to $-10\,\text{K}\,\text{km}^{-1}$, i.e., temperature decreases with height. In this layer about 80 % of the atmospheric mass is concentrated and the highest water vapor concentrations are found. Strong vertical motions can occur and nearly all cloud and weather phenomena are restricted to this layer. Most anthropogenic emissions are injected to the troposphere and distributed from there, except for aircraft exhausts in the Lower Stratosphere (LS).

Figure 1.1.: Atmospheric layers (spheres) and their transition zones (pauses) classified by their vertical temperature gradient [Mohanakumar 2008].

- In the *stratosphere* the temperature gradient reverses since its main heat source is absorption of solar radiation by ozone in the upper part. The increasing temperature with increasing altitude leads to a very stable layering, preventing nearly all vertical motion. The rare clouds forming in the layer are called *Polar Stratospheric Cloud (PSC)* since they form only at high latitudes. The upper limit of the stratosphere is the stratopause at approximately 50 km.

- The *mesosphere* is defined by a negative temperature gradient as it is has only negligible ozone concentrations and is cooled by radiative emission from CO_2. At 80 km the mesopause marks the upper end with the lowest temperatures in the atmosphere, reaching about 180 K.

- In the *thermosphere* ionization by energy rich-radiation causes a positive temperature gradient again.

- Finally, the *Exosphere* marks the border of the Earth's atmosphere to the outer space.

1.1.3. The stratosphere

The stratosphere, the layer in focus of this work, is a special characteristic of the Earth's atmosphere, since it is restricted to planets with oxygen-rich atmospheres. Its positive temperature gradient results from the absorption of high-energy UltraViolet (UV) radiation by O_2 and O_3. The chemical processes involved will be explained in more detail in section 1.2.2 below.

At its lower border the stratosphere is separated from the troposphere by the tropopause. The tropopause is defined by the World Meteorological Organization (WMO) as the first level at which the temperature decreases less than $2\,\mathrm{K\,km^{-1}}$ and the averaged temperature gradient over the next $2\,\mathrm{km}$ does not exceed this value [WMO 1957]. The altitude of the tropopause varies from $8\,\mathrm{km}$ to $18\,\mathrm{km}$ (about $300\,\mathrm{hPa}$ to $70\,\mathrm{hPa}$). Lower tropopauses occur at high latitudes, whereas the highest tropopauses are found near the equator [e.g., Seidel and Randel 2006; Rieckh 2013]. Because the temperature in the troposphere decreases with height the low-latitude tropopause can reach a minimum temperature as low as $190\,\mathrm{K}$, compared to warmer $230\,\mathrm{K}$ near the poles [Mohanakumar 2008].

The lowest ∼10 km of the stratosphere are near-isotherm, while the temperature gradient is positive higher up. The temperature peaks at about $270\,\mathrm{K}$ at the stratopause, which marks the upper boundary of the stratosphere located at approximately $50\,\mathrm{km}$ (about $0.7\,\mathrm{hPa}$). Often an additional distinction between lower, middle, and upper parts of the stratosphere is made [e.g., IPCC 2013]. In this work three sub-regions are defined covering the following altitude (pressure) ranges:

- *Lower Stratosphere (LS)*: Tropopause to $25\,\mathrm{km}$ ($30\,\mathrm{hPa}$)

- *Middle Stratosphere (MS)*: $25\,\mathrm{km}$ to $40\,\mathrm{km}$ ($30\,\mathrm{hPa}$ to $3\,\mathrm{hPa}$)

- *Upper Stratosphere (US)*: $40\,\mathrm{km}$ to $50\,\mathrm{km}$ ($3\,\mathrm{hPa}$ to $0.7\,\mathrm{hPa}$)

Due to its non-negative temperature gradient, the stratosphere is vertically very stable. While vertical transport processes in the troposphere take place on time scales from hours to a few days, stratospheric motions take place on time scales from months up to a year. Together with the low water vapor concentration this leads to the suppression of cloud formation. Consequently there is hardly any precipitation in the stratosphere which could remove injected aerosols (e.g., by volcanic eruptions).

In the recent past the role of the stratosphere in the climate system has gained increasing attention. Seidel et al. [2011] reviewed the evolving understanding of stratospheric temperature trends from early model and observation studies in the 1960s to most recent findings. Baldwin et al. [2007] summarized some of the main

points of how the stratosphere will affect climate change. Connections between the stratosphere and surface weather patterns have been investigated by Gerber et al. [2012]. The recovery of the ozone layer in the stratosphere is expected to lead to a reduction of the UV radiation burden in the troposphere. It has been suggested that the stratospheric cooling by Well-Mixed GreenHouse Gases (WMGHGs) will lead to a super-recovery of ozone in some regions and an increased stratosphere-to-troposphere ozone flux [Hegglin and Shepherd 2009]. The increase in WMGHGs which leads to a negative temperature forcing in the stratosphere will be considered in the next section.

1.1.4. Anthropogenic greenhouse gases
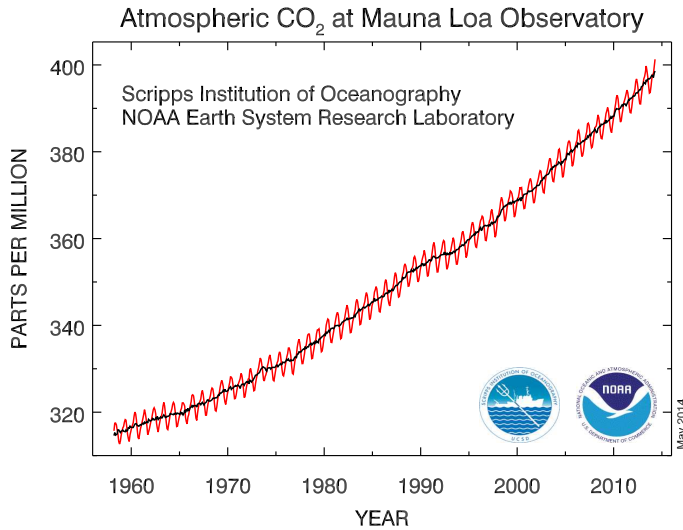
Anthropogenic GreenHouse Gases (GHGs) are man-made trace gases, influencing the atmospheric temperature. The molecules consist of three or more atoms and emit and absorb radiation in the thermal infrared range, thus altering the radiation budget of the atmosphere. In this work, *WMGHGs*, such as CO_2 and CH_4, are distinguished from unequally distributed GHGs like O_3 or H_2O. The latest IPCC AR5 states that

> "the atmospheric concentrations of carbon dioxide, methane, and nitrous oxide have increased to levels unprecedented in at least the last 800.000 years. Carbon dioxide concentrations have increased by 40 % since pre-industrial times, primarily from fossil fuel emissions and secondarily from net land use change emissions" [IPCC 2013].

The concentration changes in WMGHG are *extremely likely* ($> 99\,\%$ confidence) to be the dominant cause of the observed surface warming since the middle of the 20th century. An often used example for measurements of anthropogenic WMGHG emissions is the data record of the Mauna Loa observatory (Hawaii) shown in Fig. 1.2. It is one of the longest continuous records and shows the clear increase in surface CO_2 concentration. The distinct annual cycle is mainly due to the greening and photosynthesis of the terrestrial biosphere in the northern hemisphere spring and summer. The CO_2 concentration rose by about 25 % from under 320 ppm in the 1950s to just above 400 ppm in April 2014.

The *Kyoto Protocol to the United Nations (UN) Framework Convention on Climate Change* agreed upon in 1995, was the first attempt to reduce global GHG emissions. It entered into force in 2005 and obligates participating industrial nations to reduce their GHG emissions by at least 5 % with respect to 1990 levels in the *commitment period* from 2008 to 2012. In 2012 the *Doha Amendment* added a second commitment period covering 2013 to 2020. During the second period the aim is a reduction of GHG emissions by at least 18 % below 1990 levels [UN 1998; UN 2012].
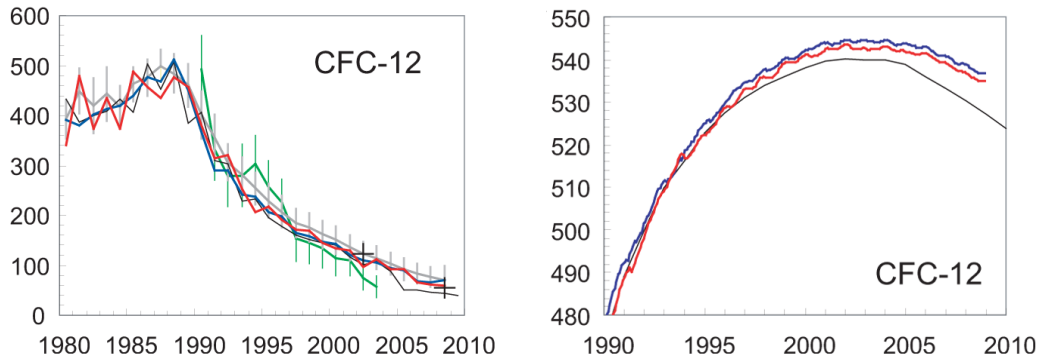
Figure 1.2.: CO_2 monthly (red) and de-seasonalized (black) mixing ratios at the Mauna Loa observatory (19°32′N, 155°34′W; 3400 m). Courtesy: P. Tans, NOAA/ESRL and R. Keeling, Scripps Institution of Oceanography (www.esrl.noaa.gov/gmd/ccgg/trends/, accessed May 2014).

1.2. The stratospheric ozone layer

The stratospheric ozone layer produces heat by absorbing high-energy UV radiation from the sun, hence shielding the Earths surface from the harmful effects of this radiation. In this section the most important chemical reactions involving stratospheric ozone are described. The main aim is on the one hand to explain the basic reactions leading to the formation and location of the ozone layer in the stratosphere and on the other hand to give examples for anthropogenic altering of these natural cycles. More elaborated descriptions can be found, e.g., in the textbooks by Jacob [1999] or by Mohanakumar [2008].

1.2.1. Anthropogenic ozone depleting substances

In the 1930s the search for new refrigerants led to the detection and increased synthesization of so called ChloroFluoroCarbons (CFCs). These substances were considered harmless to the environment since they are not toxic, unlike earlier used compounds. Therefore they quickly became widely used as refrigerants, propellants, and solvents. In 1973 however, studies showed that CFCs were spreading globally and further re-
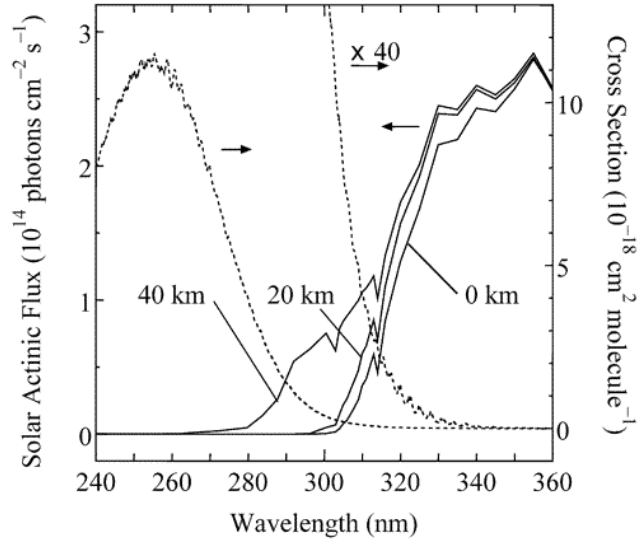
Figure 1.3.: Global emission estimates in $Gg\,yr^{-1}$ (left) and mean global surface mixing ratios in ppt (right) for CFC-12. The colors represent different observations and models. Note the different time periods covered by the figures. Adapted from WMO [2011].

search revealed that they have a lifetime of several hundred years in the troposphere. Such stable molecules can reach the stratosphere where their lifetime is significantly lower. As described in section 1.2.2 below energy-rich radiation *activates* the compounds releasing, e.g., atomic chlorine (Cl) and bromine (Br). The potential danger of this process to the ozone layer was suggested and established quite fast in the following years. The increasing awareness of the disastrous long term implications led to a series of agreements starting in 1985 with the *Vienna Convention for the Protection of the Ozone Layer*. Only two years later the *Montreal Protocol on Substances that Deplete the Ozone Layer* was agreed on. Together with its follow-up agreements amended in London (1990), Copenhagen (1992), Vienna (1995), Montreal (1997), Beijing (1999), and Montreal (2007) the Montreal Protocol is today the most widely ratified treaty in the history of the UN. Beside emission restrictions for all major Ozone-Depleting Substances (ODSs) the agreement demands a regular report on the status of the ozone layer: the Scientific Assessment of Ozone Depletion. The last update was published in 2011 [WMO 2011].

Because of their long lifetime in the troposphere, the tropospheric CFC concentration is a good proxy for their overall variability. In 2008 the tropospheric CFC concentration was about 2.08 ppb, which accounts for $\sim62\,\%$ of the total tropospheric chlorine. The main CFCs have the industrial names CFC-11, CFC-12, and CFC-113. CFC-12 is the most important type of CFC, accounting for roughly one third of their total concentration. Fig. 1.3 (left) shows different estimates of the global CFC-12 emissions in $Gg\,yr^{-1}$ from 1980 to 2010. The sudden decrease of the emission as response to the Montreal Protocol in 1987 is clearly visible. Fig. 1.3 (left) shows the evolution of CFC-12 surface concentrations in ppt, revealing a delayed response. This emphasizes the importance of the fast agreement and implementation of the

Figure 1.4.: Solar flux (solid lines, left ordinate) for 0 km, 20 km, and 40 km altitude and absorption cross-section of ozone (dotted lines, right ordinate), both as a function of the wavelength. The dotted lines represent the two main absorption bands in the UV range: the Hartley (left) and the Huggins (right) band. The Huggins band is scaled by a factor of 40 [Matsumi and Kawasaki 2003].
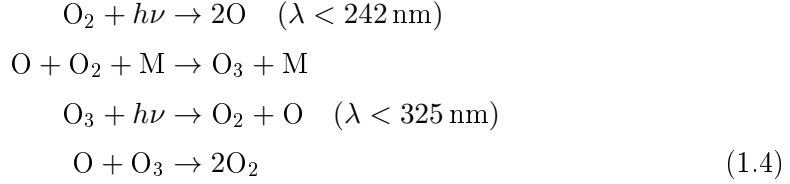
emission restrictions in the 1980s in order to protect the ozone layer [WMO 2011]. Newman et al. [2009] investigated what would have happened to the ozone layer if CFCs had not been regulated and found alarming results in a *world avoided* scenario (defined by constantly increasing ODSs). Based on model simulation they projected that 17 % of the globally averaged column ozone would be destroyed by 2020 and 67 % by 2065. This huge decline in the ozone concentration would be accompanied by changes in stratospheric temperature and dynamics as well as a severely increased UV burden on the surface.

1.2.2. Stratospheric ozone chemistry

Already in the late 18th century the existence of an ozone layer was proposed by W. N. Hartley. He measured solar radiation and found a sharp cut-off in the UV spectrum below 300 nm wavelength which he attributed to the absorption by ozone in the stratosphere [Frederick 2002]. Fig. 1.4 shows the solar flux as a function of wavelength for three different altitudes (solid lines, left ordinate). The cut-off around 300 nm for the surface and 20 km flux is clearly visible.

The first theory for the origin of the stratospheric ozone layer was proposed by S. Chapman in 1929 [Chapman 1929]. He developed the *Chapman mechanism*, a simple cycle for ozone formation and destruction by radiation:

$$O_2 + h\nu \rightarrow 2O \quad (\lambda < 242\,\text{nm})$$
$$O + O_2 + M \rightarrow O_3 + M$$
$$O_3 + h\nu \rightarrow O_2 + O \quad (\lambda < 325\,\text{nm})$$
$$O + O_3 \rightarrow 2O_2 \tag{1.4}$$
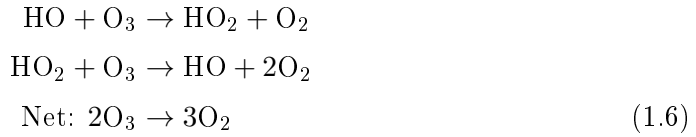
The radiation is expressed by its energy given as $h\nu$, where h is the Planck constant, ν the frequency, and λ the corresponding wavelength. Reactions 2 and 3 in Eq. (1.4) are much faster than reactions 1 and 4, which leads to a rapid cycling between O and O_3 (also known as the odd oxygen cycle) in the presence of O_2 and a third species M, which represents a collision partner not affected by the reaction. In the course of this cycle, energy in the form of radiation is absorbed by ozone in reaction 3 and set free again in the form of heat in reaction 2. This heat is then carried away by the reaction partner M.

Reaction 2 on the one hand is highly sensitive to the air density, since it needs three reaction partners. The probability for this reaction hence decreases with increasing altitude. On the other hand reaction 3 relies on the availability of UV radiation and therefore gets more improbable at lower altitudes. With that, the Chapman mechanism explains correctly the general vertical shape of the ozone layer, as well as its position in the stratosphere. However, it does not consider transport mechanisms like the Brewer-Dobson Circulation (BDC), which transports ozone from the troposphere to the stratosphere and from the equator (where production is highest due to the availability of sunlight) to higher latitudes. Moreover, the total ozone concentrations are overestimated by the Chapman mechanism alone.

This deficiency is accounted for by additional loss cycles. In the 1950s, for example, a loss cycle involving the hydrogen oxide radical HO was discovered. HO can be produced in the stratosphere by the reaction of an *excited atomic oxygen* O^* with water vapor:

$$H_2O + O^* \rightarrow 2HO \tag{1.5}$$

The HO radical can then catalyze the destruction of ozone:

$$HO + O_3 \rightarrow HO_2 + O_2$$
$$HO_2 + O_3 \rightarrow HO + 2O_2$$
$$\text{Net: } 2O_3 \rightarrow 3O_2 \tag{1.6}$$

11
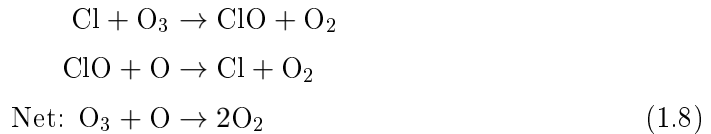
Eq. (1.6) leaves the HO concentration unchanged, so other reactions are needed to limit the availability of HO, like:

$$OH + HO_2 \rightarrow H_2O + O_2 \tag{1.7}$$
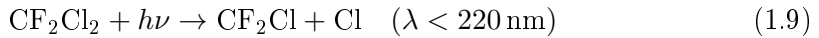
More complex loss cycles involve, for example, the nitric oxide radical NO. In 1970 P. Crutzen showed that N_2O is stable enough to reach the stratosphere where it is converted into its radical form [Crutzen 1970]. He also concluded that anthropogenic emissions of N_2O could ultimately fasten the NO based loss cycle, leading to additional ozone loss. So, while the natural state of the ozone layer was increasingly well understood, increasing amounts of ODSs had been injected into the troposphere since the 1930s. From there they were distributed to the stratosphere leading to new loss cycles as first suggested by Molina and Rowland [1974] and Crutzen [1974]. In 1995 Crutzen, Molina, and Rowland were awarded with the Nobel Price in Chemistry for their work on ozone loss.
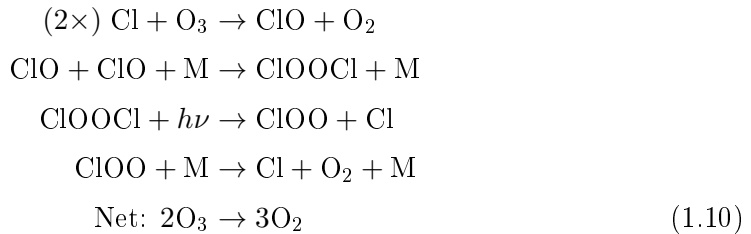
Once activated by UV radiation the CFCs release, e.g., chlorine which catalyzes ozone loss similar to that of HO:

$$Cl + O_3 \rightarrow ClO + O_2$$
$$ClO + O \rightarrow Cl + O_2$$
$$\text{Net: } O_3 + O \rightarrow 2O_2 \tag{1.8}$$
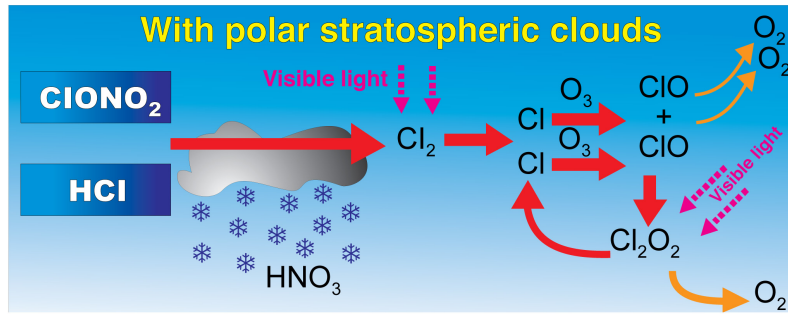
As example for the activation of a CFC in the stratosphere CFC-12 (CF_2Cl_2) is again used:

$$CF_2Cl_2 + h\nu \rightarrow CF_2Cl + Cl \quad (\lambda < 220\,\text{nm}) \tag{1.9}$$

It was only in the late 1980s that the even more effective loss mechanism given in Eq. (1.10) was detected:

$$(2\times)\ Cl + O_3 \rightarrow ClO + O_2$$
$$ClO + ClO + M \rightarrow ClOOCl + M$$
$$ClOOCl + h\nu \rightarrow ClOO + Cl$$
$$ClOO + M \rightarrow Cl + O_2 + M$$
$$\text{Net: } 2O_3 \rightarrow 3O_2 \tag{1.10}$$
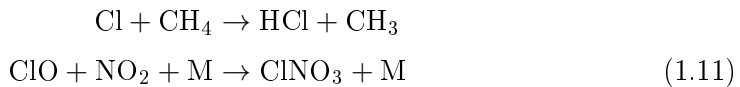
This mechanism involves the self reaction of ClO and is based on the fact that radiation does not split the ClOOCl dimer at the O-O bond. This would turn reactions 2 and 3 in Eq. (1.10) into a *null cycle*. Instead atomic chlorine is produced, leading to the most effective depletion mechanism for ozone. The reactions described in

Figure 1.5.: Activation of chlorine from reservoirs species and ozone loss in the presence of Polar Stratospheric Clouds (PSCs). Adapted from WMO [2013].

Eq. (1.10) are responsible for about 70 % of the ozone destruction leading to the annual Antarctic *ozone hole*. Cl and ClO can be deactivated into non-radical *reservoir species*, hence terminating Eq. (1.8) and Eq. (1.10):

$$Cl + CH_4 \rightarrow HCl + CH_3$$
$$ClO + NO_2 + M \rightarrow ClNO_3 + M \qquad (1.11)$$

The reservoir species can then either cycle back to active radicals or be removed from the stratosphere by deposition. Still more complex loss cycles involving, e.g., bromide will not be discussed here [Jacob 1999; Mohanakumar 2008].

1.2.3. The ozone hole

In the Antarctic winter and spring season special atmospheric conditions favor the destruction of large amounts of ozone, leading to the annual build up of the ozone hole. The ozone hole is defined as the region where the *total column ozone* (vertically integrated ozone over the entire atmosphere) is below a threshold of 220 Dobson Units (DU). One DU corresponds to 2.69×10^{16} molecules cm^{-2} or a layer $10 \, \mu m$ thick under standard temperature and pressure (273 K, 1013.25 hPa).

During the polar night at high southern latitudes the absence of sunlight leads to a strong temperature decrease in the stratosphere. The build up of the *polar vortex*, a strong wind system circling the Antarctic continent in the stratosphere, additionally isolates the air inside it. Within the vortex the temperatures can drop as low as 190 K, hence allowing the formation of PSCs. These clouds consist of ice and nitric acid (HNO_3) particles [WMO 2013].

Fig. 1.5 shows an example ozone loss cycle in the presence of PSCs. The clouds have two negative impacts: On the one hand chlorine bound in reservoir species (cf. Eq. (1.11)) is activated on the surface of the cloud particles. On the other hand

HNO_3 is removed from the stratosphere as precipitation limiting the amount of NO_2 available for the deactivation of chlorine into reservoir species.

The main ozone destruction occurs in spring, since the loss cycles depend on the availability of sunlight (right hand side of Fig. 1.5). However, the sun also heats the polar stratosphere, dissipating the PSCs and reducing the strong temperature gradient to lower latitudes. This ultimately leads to the breakdown of the polar vortex in late spring. Ozone rich air from outside the vortex can now mix with polar air and the ozone hole dissolves.
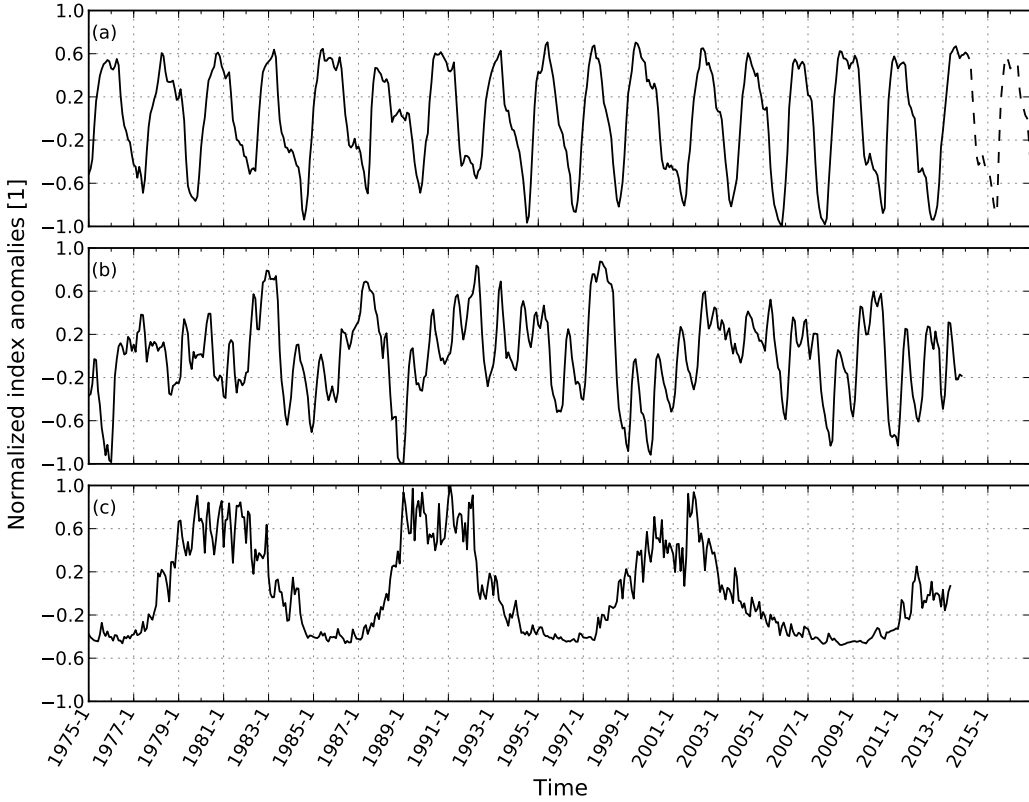
1.3. Stratospheric variability

In this section the most important processes leading to *natural variability* in atmospheric variables such as temperature and ozone are discussed. Natural variability comprises periodic, quasi-periodic or even sudden changes in the climate system which are not caused by humans. These changes can be externally forced (e.g., the annual cycle caused by solar irradiance variations) or develop within the system (e.g., the Quasi-Biennial Oscillation (QBO) or volcanic eruptions). It is essential to account for these natural signals when investigating anthropogenic induced atmospheric trends.

1.3.1. The annual cycle

The annual or seasonal cycle is caused by the tilting of the Earth's axis against the ecliptic. The total amount of sunlight reaching the surface of the Earth at a given latitude is changing with season, influencing the temperature. This change is more distinct at higher latitudes. Since the troposphere is mainly heated from the ground its air temperature strongly follows the seasonal cycle. In the stratosphere the situation is more complex as indirect effects have to be considered.

The annual ozone hole is a phenomenon which follows in principle the seasonal cycle. But feedback mechanisms amplify the extend of the annual variation. During the polar night at both, high northern and southern latitudes, the polar vortex builds up. This atmospheric wind pattern prohibits the exchange of polar air with lower latitude air, hence leading to even lower temperatures during the winter months. In spring the weakening of the polar vortex leads to *sudden stratospheric warming* events or to a so called *final warming* if the vortex breaks down entirely. The final warming itself happens very fast (within several days). The possible time range in which it can occur is rather long (several months). Thus, the date of the final warming strongly influences the annual cycle of stratospheric temperature. Moreover, the ozone cycle is also severely impacted. It is currently under discussion if the climate change may

Figure 1.6.: Normalized indices of some main sources of atmospheric natural variability. The time resolution is 1 month. (a) 30 hPa zonally averaged wind speed representing QBO, (b) Sea Surface Temperature (SST) for the Nino3.4 region representing El Niño–Southern Oscillation (ENSO), and (c) 10.7 cm solar flux index representing solar activity.
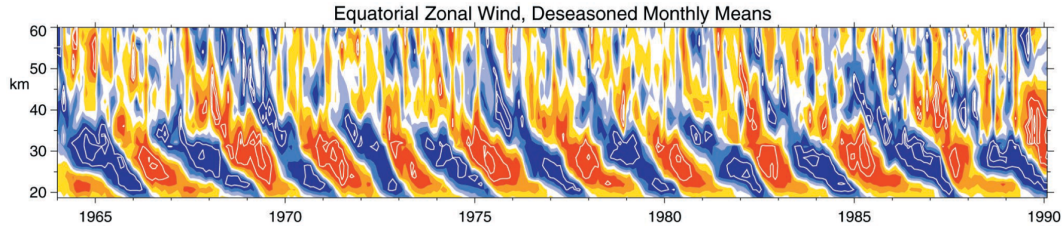
feed back into the vortex evolution and, e.g., favor a later vortex break down, which would lead to a further cooling of the polar stratosphere and additional ozone loss [Rex et al. 2004; Hitchcock et al. 2009; Manney et al. 2011; Rieder and Polvani 2013].

1.3.2. The Quasi-Biennial Oscillation

The QBO is an important mode of internal natural variability in the tropical stratosphere. It is characterized by changes in the wind speed and associated temperature and ozone variations. As indicated by its name the QBO has a periodicity of approximately 2 years [Baldwin et al. 2001].

The QBO induced westerlies (winds from the west) have a maximum amplitude of about $15\,\mathrm{m\,s^{-1}}$, while the easterlies (winds from the east) reach up to twice that value [Dunkerton 2002]. The QBO has a period of 24 to 30 months with a mean period of 28.2 months from 1953 to 1995. It is influenced but not synchronized to the annual

Figure 1.7.: De-seasonalized equatorial winds as function of time and altitude from 1964 to 1990. The shading interval is $6\,\mathrm{m\,s^{-1}}$, with $\pm 3\,\mathrm{m\,s^{-1}}$ unshaded, red shading representing positive (westerly) winds, and blue shading representing negative (easterly) winds. The data are merged from different observations near the equator. Adopted from Baldwin et al. [2001].

cycle, as the change between westward and eastward winds tends to happen in the northern hemisphere late spring and early summer [Baldwin et al. 2001]. The QBO reaches its largest amplitude between $10\,\mathrm{hPa}$ ($32\,\mathrm{km}$) and $30\,\mathrm{hPa}$ ($24\,\mathrm{km}$) directly at the equator. At higher and lower altitudes the amplitude decreases and moreover the phase of the QBO is shifted about one month per kilometer altitude (i.e., a certain state occurs earlier at higher latitudes and propagates downwards with time). This is seen in Fig. 1.7 which shows de-seasonalized winds at the equator. Towards higher latitudes the amplitude of the QBO follows roughly a equator centered normal distribution with a half width of approximately $12°$. More theoretical background on the development of the QBO is provided, e.g., by Holton and Hakim [2013].
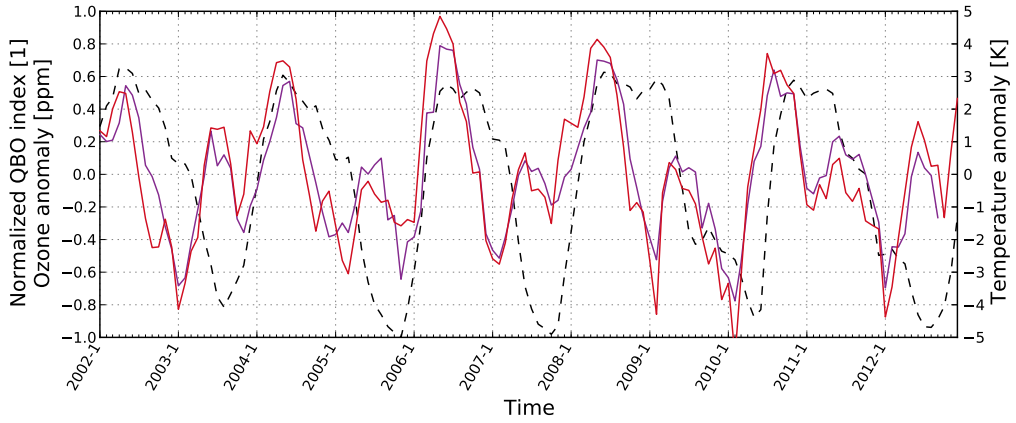
QBO index

As proxy for the QBO variability the $30\,\mathrm{hPa}$ zonal averaged monthly averaged wind at the equator is used. The time series was downloaded from a regularly updated online data set calculated from NCEP reanalysis data provided by the NOAA/OAR/ESRL PSD, Boulder, Colorado, USA.[1] Fig. 1.6a shows a representation of the $30\,\mathrm{hPa}$ zonally averaged wind at the equator. The measurement time series reaches from January 1975 to March 2014 (solid line).

For this thesis I extended the time series into the future (dashed line until 2016) by appending the April 2009 to December 2011 cycle. It is used as estimate for the future QBO evolution because it can be considered a typical representation of the variability in the last decade. Moreover the March 2014 value and the March 2009 value agree within $2\,\%$. The extension into the future is necessary for use of the

---

[1] www.esrl.noaa.gov/psd/data/correlation/qbo.data, accessed April 2014

Figure 1.8.: De-seasonalized temperature (red) and ozone (violet) as well as QBO index (black, dashed) for the 0°N to 10°N latitude band at the 30 hPa level. Ozone and QBO index are denoted on the left axis, temperature on the right axis.

index regression because the downward propagation of the QBO can lead to shifts of over 30 months between the wind index at 30 hPa and ozone or temperature.

The original data have been normalized following Eq. (1.12):

$$x_{\text{normalized}} = \frac{x_{\text{original}} - \bar{x}}{\max\left(|x_{\text{original}} - \bar{x}|\right)}, \tag{1.12}$$

where $\bar{x}$ is the mean of x computed by averaging over all available data from January 1975 onwards. The denominator represents the maximal amplitude appearing in the time series. This normalization is applied to the ENSO and solar flux indices as well and is intended to simplify inter-comparison of the regression coefficients.

Influence on temperature and ozone

In the stratospheric equatorial region the QBO is beside the annual cycle the most important phenomenon causing natural temperature and ozone variations. Fig. 1.8 shows de-seasonalized temperature and ozone data as well as the normalized QBO index for the 30 hPa level in the 0°N to 10°N latitude band. The quasi two-year period is clearly visible for all variables. The maximum amplitude of de-seasonalized ozone and temperature is approximately 0.8 ppm and 5 K, respectively. The QBO accounts for about 0.6 ppm and 4 K, respectively, of this variability.

The second obvious feature is a phase shift between temperature, ozone and QBO index. This *lag* will be analyzed in more detail in section 3.3.

1.3.3. El Niño–Southern Oscillation

El Niño is a phase of warm SST anomalies in the tropical eastern Pacific. It is closely connected to the *Southern Oscillation*, a change in the surface pressure. For the whole phenomenon the name El Niño–Southern Oscillation (ENSO) was established.
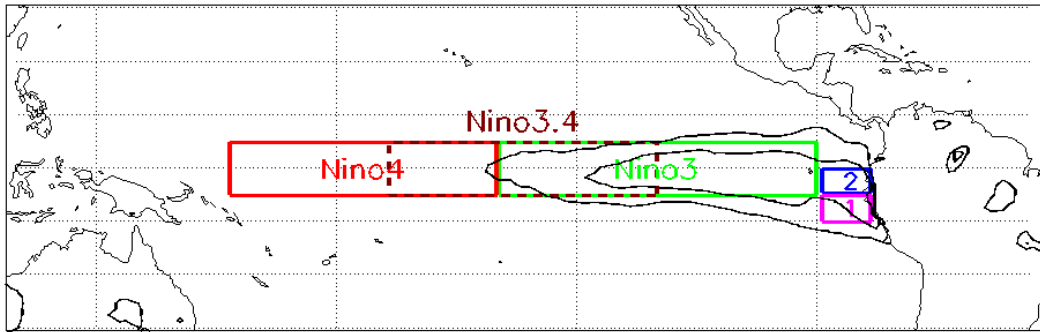
During ENSO neutral conditions easterly winds in the eastern Pacific move warm surface water away from the South American west coast. This water is than replaced by colder water from the deeper ozean — a process called upwelling. This process causes a temperature gradient of several Kelvin between the eastern and western Pacific. This gradient is accompanied by different weather patterns, since warmer oceans favor heavy precipitation in the tropics.

The El Niño or ENSO warm phase starts with an initial rise in the east Pacific SST. This weakens the easterlies, which then feeds back, further warming the ocean. Depending on the magnitude of the El Niño event the temperature gradient between the eastern and western Pacific can completely disappear. The weaker easterlies also lead to the build up of a high pressure region over Oceania. More information can be found in the book *Atmospheric Science* by Wallace and Hobbs [2006]. The opposite ENSO cold phase is called *La Niña*. The main characteristics of El Niño compared with neutral or La Niña conditions are:

- Weaker easterlies along the equator.

- Lower SST in the eastern Pacific.

- The surface pressure in the western Pacific and over Australia and Oceania is higher.

- Slight rise (lowering) of the eastern (western) Pacific sea level.

Although ENSO is a local phenomenon in the tropical Pacific it impacts atmospheric weather patterns globally. For example the 1877 El Niño caused sever droughts in India, China, Australia, and other countries, which led to the discovery of the Southern Oscillation [Chang and Zebiak 2002; Wallace and Hobbs 2006].

Modern remote sensing techniques and RadioSonde (RS) measurements allow a detection of ENSO associated variability also in the upper troposphere and stratosphere as described e.g. by Reid et al. [1989] and Free and Seidel [2009]. Calvo et al. [2008] give an update on the scientific understanding of the ENSO propagation into the stratosphere and Randel et al. [2009] discuss its influence on temperature and ozone.

Figure 1.9.: Reference regions for different ENSO indices in the tropical Pacific. The Nino3.4 region (dashed, brown) lies between 5°N and 5°S and 120°W and 170°W. Graphic by W. M. Connolley (CC BY).

ENSO index

To identify ENSO associated atmospheric variability the Nino3.4 index[1] (Fig. 1.6b) is used. It utilizes the SST in the tropical Pacific from 5°N to 5°S and 120°W to 170°W as proxy for the ENSO phases. Fig. 1.9 shows different reference regions used for SST measurements.

1.3.4. Solar flux

The Sun is the Earth's most important energy source. The Total Solar Irradiance (TSI) or total radiative energy reaching the Earth changes over time.

This change happens on several different time scales. During the Earth's history (comprising several billion years) the Sun's luminosity has increased by 25 % to 30 %, having huge impacts on climate on Earth [Rosing et al. 2010]. The 11 year solar cycle leads to luminosity changes on a decadal scale. On an annual basis the largest amount of change is attributable to the elliptic orbit geometry of the Earth, leading to varying distances to the Sun.

For the time spans investigated in this work the Sun's long term luminosity trend is negligible. The IPCC AR5 does not find any significant contribution of solar irradiance changes to the radiative forcing trend since 1750 [IPCC 2013]. The second source of luminosity changes is the 11 year cycle in solar activity. While the corresponding total variability in TSI is below 0.1 %, the changes in the UV range exceed 4 %. This makes the stratosphere especially sensible to the solar cycle, showing, e.g., temperature differences of $\sim 2\,\mathrm{K}$ between solar minimum and maximum. About half of this response is estimated to result direct from TSI changes, while the other half is

---

[1] www.esrl.noaa.gov/psd/data/correlation/nina34.data, accessed April 2014

due to ozone feedback mechanisms [Gray et al. 2010]. The changes connected to the Earth's orbit geometry are not further discussed here since they are removed with the seasonal cycle.

Solar flux index

Fig. 1.6c shows the normalized 10.7 cm radio flux[1] used as proxy for the solar activity. The response of temperature and ozone to TSI changes is considered to be immediate, hence zero lag is used in the entire stratosphere. A detailed review of the solar influence on climate can be found e.g. in Gray et al. [2010].

---

[1] www.esrl.noaa.gov/psd/data/correlation/solar.data, accessed April 2014

2. Data sets
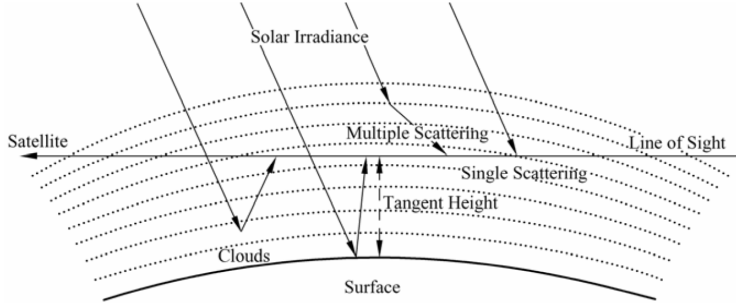
2.1. Satellite remote sensing

Global observations of the higher atmosphere rely mainly on remote sensing techniques. In contrast to in-situ measurements remote sensing acquires information about the atmosphere without being in direct contact with it [Elachi and Zyl 2006]. All observations used in this work are based on satellite remote sensing except the RS data which are in situ measurements.

The higher up in the atmosphere a region of interest lies, the harder it is to measure with ground-based systems or in-situ instruments. The reason for the former is the exponential decay of air density with altitude. When measuring, for example, stratospheric properties from the ground the much denser troposphere can pose a huge source of disturbance for the signal from above. In-situ measurements of the free atmosphere are limited by the delivering system. RSs for instance rely on weather balloons to reach higher altitudes and therefore measure in the troposphere and lower stratosphere, since the balloons burst due to the low pressure at higher altitudes [DuBois et al. 2002]. Satellite based remote sensing overcomes this restrictions by measuring the atmosphere from above. Satellite based remote sensing can be performed in different measurement geometries. In this work three different techniques are distinguished:

- *Limb-looking* instruments observe the atmosphere by looking across it parallel to the surface. This allows for a high vertical resolution but restricts horizontal localization of the received information. Fig. 2.1 shows a schematic limb geometry. The black lines represent paths of photons emitted from the sun before they are scattered into the Line Of Sight (LOS) of the satellite. The exponential decay of density with altitude plays an important role in assigning a measured signal to a certain area. At the Tangent Point (TP) the LOS is exactly parallel to the surface, the distance is minimal and the density therefore maximal. As a result the area close to the TP has the largest impact to the overall signal.

- *Occultation* instruments are limb-sounding systems. The use a radiation source at the far end of the LOS. This can either be an artificial signal from a second

Figure 2.1.: Schematic limb geometry. The solid black lines represent possible photon paths, before they are scattered into the LOS of the receiver satellite. The TP is located on the LOS above the tangent height (point of minimal distance between surface and LOS at a given time) [Qu et al. 2006].

satellite, as in the case of Radio Occultation (RO) or a natural source, such as a star, as in the case of the Global Ozone Monitoring by Occultation of Stars (GOMOS) instrument. During an *occultation event* the signal source either sets or rises from the perspective of the sensor. In this process the LOS scans through the entire atmosphere from the top down (setting event) or from bottom up (rising event). A schematic RO setting event geometry is shown in Fig. 2.2a. A huge advantage of occultation methods is the self calibrating nature. Regardless of the radiation source, every event can be calibrated by the original signal, which is defined as the undisturbed sensor reading above the top of the atmosphere.
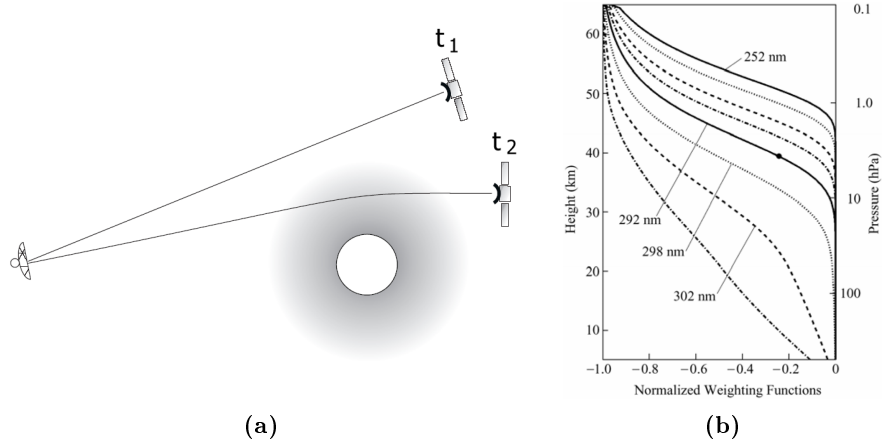
- *Down-looking* (or nadir-looking) systems measure the atmosphere directly beneath them. They have a high horizontal resolution but can provide only limited vertical differentiation. Therefore they are for example used to measure total column ozone or other integrated properties. It is however possible to achieve information from different atmospheric layers by using a priori information and carefully selected weighting functions as shown in Fig. 2.2b for the Solar Backscatter UltraViolet 2 (SBUV/2) instrument. The curves represent different wavelengths, which provide information from different altitude layers. Note, the dot on the 292 nm line at 40 km altitude and at a weighting function value of 0.25. It denotes that the channel will response to changes at 40 km by a factor 0.25 less than it would to changes on the top of the atmosphere [Qu et al. 2006]. Or in other words: 75 % of the back-scattered photons at this wavelength are from above 40 km.

Tab. 2.1 gives an overview of all data sets used in this work. A more detailed description of all data sets is given in the following.

Table 2.1.: Overview of all data sets used in this study. The information is based on the original data.

Data set	Parameter (unit)	Time range	Horizontal resolution	Pressure levels (hPa)
RO	Temperature (K)	2002 to 2012	5° latitude bands, −50° to 50°	..., 100, 99, 97, 95, 93, 92, 90, 89, 87, 85, 84, 82, 81, 80, ...
RS	Temperature (K)	1950 to 2012	10° latitude bands, −90° to 90°	850, 700, 500, 400, 300, 250, 200, 150, 100, 70, 50, 30
HARMOZ	O_3 (mol mol^{-1})	2001 to 2012	10° latitude bands, −90° to 90°	450, 400, 350, 300, 250, 200, 170, 150, 130, 115, 100, 90, 80, 70, 50, 40, 30, 20, 15, 10, 7, 5, 4, 3, 2, 1.5, 1, 0.7, 0.5, 0.4, 0.3, 0.2, 0.15, 0.1, ...
GOZCARDS	O_3 (mol mol^{-1}) H_2O (mol mol^{-1})	1979 to 2012	10° latitude bands, −90° to 90°	1000, 681, 464, 316, 215, 146, 100, 68, 46, 31, 21, 14, 10, 6.8, 4.6, 3.1, 2.1, 1.4, 1.0, 0.68, 0.46, 0.31, 0.21, 0.14, 0.10
SBUV	O_3 (ppm)	1979 to 2012	5° latitude bands, −90° to 90°	0.5, 0.7, 1, 1.5, 2, 3, 4, 5, 7, 10, 15, 20, 30, 40, 50
ERA-Interim	Temperature (K) O_3 (kg kg^{-1}) H_2O (kg kg^{-1})	1979 to 2012	0.75° × 0.75° grid, −90° to 90° latitude, 0° to 360° longitude	1, 2, 3, 5, 7, 10, 20, 30, 50, 70, 100, 125, 150, 175, 200, 225, 250, 300, 350, 400, 450, 500, 550, 600, 650, 700, 750, 775, 800, 825, 850, 875, 900, 925, 950, 975, 1000

(a)   (b)

Figure 2.2.: (a) Schematic geometry of an RO setting event. At the time t_1 the undisturbed signal reaches the receiver satellite. At a later time t_2 the ray path is bend due to the density of the atmosphere. (b) Possible weighting functions for different wavelengths of a nadir looking system [Qu et al. 2006].

2.2. Temperature measurements

2.2.1. Radio occultation data

The Wegener Center for Climate and Global Change (WEGC) RO retrieval delivers global temperature profiles with high vertical resolution. In this work the data are used from 2002 to 2012 for the stratosphere. The data are based on RO sensors aboard different Low Earth Orbit (LEO) satellite missions including the CHAlleng-ing Minisatellite Payload (CHAMP), Gravity Recovery And Climate Experiment (GRACE), and FORMOSAT-3/COSMIC (F3C). For the retrieval of the temper-ature profiles the WEGC Occultation Processing System in its latest version 5.6 (OPSv5.6) is used [Schwärz et al. 2013].

RO measures are performed in limb sounding mode, using artificial sources of elec-tromagnetic waves. The satellites mentioned above receive radiation from the two Global Positioning System (GPS) frequencies (with wavelengths of several centime-ters, hence radio-waves). During an occultation event the signals pass through the Earth's atmosphere and get bend due to the Earth's density gradients. This bending is measured as a *phase-shift* with respect to the undisturbed signal. This measure-ment is based on synchronized, high-precise atomic clocks on both satellites.
In the further course of the retrieval unwanted altering is removed. This includes the Doppler-shift due to the movement of both, the emitter and receiver satellite and the ionospheric influence on the measurement. The latter is eliminated by a combination

of the two GPS frequencies [Liu et al. 2013]. The Doppler-shift correction utilizes precise orbit information (position and velocity of emitter and receiver satellite), which is in the next step also used to calculate the *bending angle* from the phase-shift.

An inverse Abel integral is then applied to receive the *refractivity* as a function of altitude. Due to low signal-to-noise ratio at high altitudes the WEGC OPSv5.6 RO data are initialized using short-range forecast profiles of the European Centre for Medium-Range Weather Forecasts (ECMWF). As a result the RO products are not entirely independent from ECMWF, although RO information dominates the retrieval below about 40 km [Schwärz et al. 2013].

Dry atmospheric parameters (e.g., dry temperature) follow from the refractivity in the next step of the retrieval. Using additional information (e.g., the vater vapor concentration) also physical parameters (e.g., temperature) can be obtained. In this work the dry parameters are used in the stratosphere since they are highly consistent with their physical counterparts due to the low water vapor content. The vertical resolution of the RO temperature profiles is about 1 km. A detailed description of the WEGC OPSv5.6 retrieval can be found in Schwärz et al. [2013].

WEGC RO temperature data are highly consistent between different receiver satellites due to the self-calibrating nature of the measurements [Foelsche et al. 2011]. Therefore they can be combined to a single climate record without any calibration or homogenization. RO measurements show high accuracy in the upper troposphere and LS [Scherllin-Pirscher et al. 2011a; Scherllin-Pirscher et al. 2011b]. Structural uncertainty was found to be lowest within $\pm 50°$ latitude and below 25 km [Steiner et al. 2013a]. The GPS satellites have a fixed inclination of $55°$ and therefore the distribution of occultation events depends on the receiver orbit. All receiver satellites used in this work are in near polar orbits, hence providing global coverage.

The newly reprocessed data based on the OPSv5.6 are not yet available for public, but the products of the former version (v5.4) can be found online in the Network Common Data Format (NetCDF).[1] For this study monthly means merged to $5°$ latitude bands are used. Each band was area weighted with the cosine of the latitude. An additional averaging was performed to obtain $10°$ zonal bands in order to compare to the other data sets. Note that the sampling error due to unequal sampling in space and time [Scherllin-Pirscher et al. 2011b] is not considered in this work. The time series of RO temperature are shown in the appendix (Fig. A.1).

---

[1] www.globclim.org

2.2.2. Radiosonde data

Radiosonde Innovation Composite Homogenization (RICH) is a temperature data set obtained from RS measurements, covering the time period 1950 to 2012. In this study I use the data from 1979 onward. RSs perform in-situ measurements of temperature and other atmospheric properties in the troposphere and LS. RICH is provided by L. Haimberger, University of Vienna, Austria [Haimberger et al. 2012].

RICH is based on data from a global RS measurement network with over 1000 stations. The coverage is however very unequal and limited to the continents. A high station density in the northern hemisphere industrialized areas faces sparse measurements in the southern hemisphere.
RS measurements are synchronized using the Coordinated Universal Time (UTC). Usual the starting times are 00 UTC and 12 UTC [Haimberger et al. 2008; Ladstädter et al. 2011]. Over the years many different RS types have been in use. Blaschek [2009] gives an overview on the most important instruments and their global distribution. In order to merge RS data from different instruments over time to a consistent climate record RICH uses advanced homogenization techniques [Haimberger et al. 2012]. The sondes are transported to higher altitudes by weather balloons but if compared to satellite measurements they have a restricted vertical coverage. RICH provides data up to an altitude of about 22 km ($\sim$15 km at high southern latitudes). The data set is available online as NetCDF.[1] RS time series and their coverage are shown in the appendix (Fig. A.2).

2.3. Ozone and water vapor measurements

2.3.1. Harmonized dataset of ozone profiles

The HARMonized dataset of OZone profiles (HARMOZ) provides ozone data from a series of different instruments on different satellites. It includes data from the GOMOS, the Michelson Interferometer for Passive Atmospheric Sounding (MIPAS), and the SCanning Imaging Absorption spectroMeter for Atmospheric CHartographY (SCIAMACHY) instruments on Envisat. Furthermore data are used from the Optical Spectrograph and InfraRed Imaging System (OSIRIS) and the Sub-Millimetre Radiometer (SMR) instruments on Odin as well as from the Atmospheric Chemistry Experiment–Fourier Transform infrared Spectrometer (ACE-FTS) on SCISAT. HARMOZ covers the upper troposphere up to the mesosphere for the years 2001 to 2012 and was created in the course of the European Space Agency (ESA) Climate

---

[1]ftp://srvx7.img.univie.ac.at/pub/v1.5.1, accessed January 2014

Change Initiative (CCI) project [Sofieva et al. 2013].

For the trend analysis in this thesis only four of the six instruments included in the HARMOZ data set are used. The selection process follows the comparison performed by Tegtmeier et al. [2013] as well as the data agreement tables provided by Sofieva et al. [2013]. The aim was to use only those instruments which show high consistency in the stratosphere. The used instruments are:

- **GOMOS, Envisat:** GOMOS uses the occultation of stars to measure the global night-time concentrations of ozone and related trace gases in an altitude range between 15 km and 100 km with a vertical resolution of 2 km to 3 km. The GOMOS instrument was operational on Envisat from 2002 to 2012 [Kyrölä et al. 2004].

- **MIPAS, Envisat:** Also payload on Envisat, MIPAS covers the same time period as GOMOS. In 2004 a change in the measurement mode had to be made for technical reasons [Clarmann et al. 2009]. MIPAS is a Fourier transform spectrometer, operating in limb mode. It measures ozone and a range of other trace gases from about 5 km to 150 km altitude. Its vertical resolution changes with height, but is generally better than 3 km [Eckert et al. 2013].

- **OSIRIS, Odin:** Launched in 2001 on board the Odin spacecraft, OSIRIS is still operational. Its global coverage is restricted due to the sun-synchronous orbit of Odin. OSIRIS operates in limb mode, measuring ozone from approximately 10 km to 100 km altitude, with a resolution of 2 km to 3 km [Llewellyn et al. 2004].

- **ACE-FTS, SCISAT:** ACE-FTS measures ozone using solar occultation. It covers the atmosphere from the top of the clouds at around 10 km up to 150 km with a vertical resolution of $\sim$3 km. The instrument was launched aboard the Canadian SCISAT satellite in 2003 and is still operational [Dupuy et al. 2009].

Sofieva et al. [2013] investigated the relative biases from GOMOS, OSIRIS, and ACE-FTS with respect to MIPAS and found a difference below 5 % in most of the stratosphere. Larger discrepancies appear especially in the US above 40 km and in the LS below 20 km. In the study by Tegtmeier et al. [2013] the difference is taken to a multi-instrument mean and generally good agreement is found for the tropical and mid-latitude MS and US. In the LS, GOMOS and OSIRIS show larger disagreement up to 50 %. At high latitudes the situation is similar and differences up to 50 % with respect to the multi-instrument mean occur. In a recent study by Eckert et al. [2013] drifts and trends from MIPAS, OSIRIS, and ACE-FTS are compared to each other.

The HARMOZ data are provided as NetCDF on the ESA CCI homepage.[1] The temporal and spatial data coverage of the time series is generally good for the whole period. At high southern latitudes some months of data are missing before 2004. The overall coverage can be seen in the time series plotted in the appendix (Fig. A.3).

The common pressure grid

All instruments deliver their measurements on varying altitude or pressure grids, so that an interpolation to a Common Pressure Grid (CPG) is necessary in order to compare the different data sets. In this work the pressure grid introduced by Sofieva et al. [2013] is used as CPG for all data sets. It has a vertical resolution of about 1 km below 20 km and of 2 km to 3 km above. The transformation from other grids is done by linear interpolation of the logarithmic pressure coordinate. Additionally each pressure level is allocated to a corresponding altitude z in km, which is estimated using a fixed scale height:

$$z = 16 \log_{10} \left(\frac{1013}{p} \right), \tag{2.1}$$

where p is the pressure in hPa. In this work pressure (altitude) ranges from 250 hPa to 0.4 hPa (10 km to 55 km). Following Sofieva et al. [2013] the pressure levels [hPa] and corresponding approximate altitudes [km] within this range are:

Table 2.2.: Pressure (altitude) levels in hPa (km)

250 (9.72)	70 (18.57)	4 (38.46)
200 (11.27)	50 (20.91)	3 (40.46)
170 (12.4)	40 (22.46)	2 (43.27)
150 (13.27)	30 (24.46)	1.5 (45.27)
130 (14.27)	20 (27.27)	1 (48.09)
115 (15.12)	15 (29.27)	0.7 (50.57)
100 (16.09)	10 (32.09)	0.5 (52.91)
90 (16.82)	7 (34.57)	0.4 (54.46)
80 (17.64)	5 (36.91)	

2.3.2. The solar backscatter ultraviolet instruments

The Solar Backscatter UltraViolet (SBUV) spectrometers are a series of National Aeronautic and Space Administration (NASA) instruments designed to monitor the

---

[1]http://www.esa-ozone-cci.org/?q=node/161, accessed November 2013

vertical distribution and the total amount of ozone in the free atmosphere. The first instrument was launched on the Nimbus-7 satellite in 1978. Until now several follow-up missions have been carried out and the time series covers a 34-year period until 2012. Though the instruments were designed to measure ozone on a daily basis (and therefore need careful inter-calibration and drift correction) the length of the data set makes it interesting to be used as a climatology. The National Oceanic and Atmospheric Administration (NOAA) has created such a climatology using the SBUV algorithm version 8.6 (SBUVv8.6) [Bhartia et al. 2013].

The quantity measured for the ozone retrieval is the ratio of radiance emitted from the earth with respect to to solar irradiance. This is done at 12 wavelengths between 250 nm and 340 nm by a nadir-looking geometry. The SBUV instruments receive solar UV radiation back scattered from the Earth's atmosphere and surface. Typically about once a week a diffuser is used to channel direct sunlight into the down-looking instruments for irradiance measurements and long-term calibration. The list below gives an overview of all SBUV instruments which provided data to the climatology used in this work.

- **SBUV, Nimbus-7:** October 1978 until June 1990

- **SBUV/2, NOAA satellites:** The SBUV/2 instruments continued the ozone measurements from SBUV. They had an additional mercury lamp aboard to track the reflectivity changes in the diffuser. Until today there have been several identically constructed instruments on different satellites:
    - **NOAA-9:** February 1985 until January 1998
    - **NOAA-11:** January 1989 until March 2001
    - **NOAA-14:** March 1995 until September 2006
    - **NOAA-16:** October 2000 until present
    - **NOAA-17:** August 2002 until April 2013
    - **NOAA-18:** January 2005 until present
    - **NOAA-19:** March 2009 until present

For a more detailed description of the instruments see the *README Document* by Johnson et al. [2012]. The SBUVv8.6 uses an inverse model based on an optimal estimation approach to retrieve ozone information. More detailed information can be found in the corresponding publications, e.g., Bhartia et al. [1996], McPeters et al. [2007], McPeters and Labow [2012], Johnson et al. [2012], Bhartia et al. [2013], and Kramarova et al. [2013].

Different ozone products are provided by NOAA. In this work ozone mixing ratios in ppm are used. These data cover a pressure range from 50 hPa to 0.5 hPa, which corresponds to an altitude range from about 21 km to 53 km. The vertical resolution is comparable to the CPG so that the data can be interpolated to this grid without any further adaptation. The data are provided in the Hierarchical Data Format (HDF) at the Goddard Earth Sciences Data and Information Services Center (GES DISC) homepage.[1] As stated above and shown e.g. by Bhartia et al. [2013] some of the SBUV/2 instrument overlap in time. To create a merged ozone time series the average of the overlapping periods was computed. Moreover the 5° latitudinal bands were merged to 10° bands to match the horizontal resolution of the other data sets. The SBUV data are nearly continuously available at middle and low latitudes for the whole 1979 to 2012 period. Towards high latitudes (polewards of 55°S and of 65°N, respectively) data are missing in the winter months. For the ±85° bands no data are available. An overview of the SBUV time series of all latitude bands is given in Fig. A.4 in the appendix.

2.3.3. Global ozone chemistry and related trace gas data records for the stratosphere
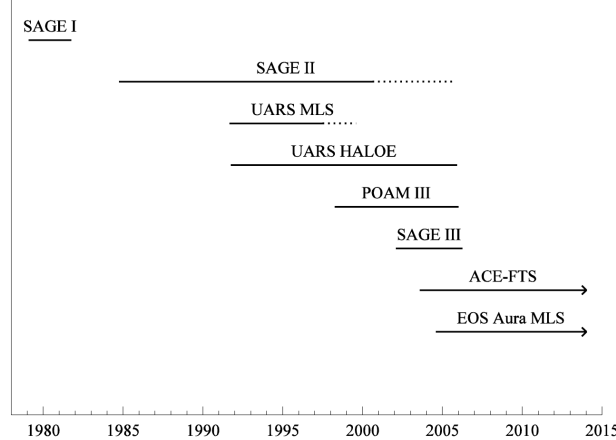
The Global OZone Chemistry And Related trace gas Data Records for the Stratosphere (GOZCARDS) project is part of the NASA Making Earth Science data records for Use in Research Environments (MEaSUREs) program and delivers among other atmospheric trace gases also ozone and water vapor profiles. The data sets are merged together based on a range of different sources and cover a 28 year period from 1985 to 2012 (some measurements reach back to 1979) [Froidevaux et al. 2013]. Fig. 2.3 shows the different missions contributing to the GOZCARDS data set between 1979 and 2012. A more detailed description of the instruments and processing versions can be found in Froidevaux et al. [2013] and references therein. A detailed comparison of the different data sets was done by Tegtmeier et al. [2013] for ozone and by Hegglin et al. [2013] for water vapor. Here only a short summary of the instruments used for the GOZCARDS data set is given:

- **SAGE I, AEM-B:** The Stratospheric Aerosol and Gas Experiment I (SAGE I) was an instrument aboard the Applications Explorer Mission-B (AEM-B) satellite. It measured ozone from 1979 to 1981 using solar occultations.

---

[1] `disc.sci.gsfc.nasa.gov/datareleases/MEaSUREs-SBUV-Ozone`, accessed November 2013

Figure 2.3.: Temporal coverage of measurements considered for the GOZCARDS project. The dotted lines towards the end of the SAGE II and UARS MLS coverage indicate degradation in the coverage [Froidevaux et al. 2013].

- **SAGE II, ERBS:** SAGE II, the successor of SAGE I was launched in 1984 on the Earth Radiation Budget Satellite (ERBS) and was measuring ozone until 2005.

- **HALOE, UARS:** Payload on the Upper Atmosphere Research Satellite (UARS) satellite, the HALogen Occultation Experiment (HALOE) measured ozone and water vapor using the solar occultation technique. It was operational from 1991 to 2005.

- **MLS, UARS:** The Microwave Limb Sounder (MLS) on UARS delivered ozone data from 1991 to 1997 and water vapor data until 1995.

- **MLS, Aura:** The MLS instrument aboard the Aura satellite delivers ozone and water vapor measurements from 2004 onwards.

- **ACE-FTS, SCISAT:** ACE-FTS on SCISAT contributes ozone and water vapor data to GOZCARDS, from 2004 onwards.

The merged GOZCARDS ozone and water vapor time series are available online as NetCDF.[1]

---

[1] disc.sci.gsfc.nasa.gov/datareleases/measures-gozcards-data-now-available, accessed September 2013

2.4. Reanalysis fields

The ERA-Interim fields are used in this work for comparison to the temperature, ozone and water vapor observationl data sets. A reanalysis combines numerical forecast models and observations. ERA-Interim is updated in near-real time and covers the time period from 1979 to present[1] [Simmons et al. 2007; Dee et al. 2011]. All files were downloaded from the ECMWF homepage.[2] In this work *monthly means of daily mean fields* on pressure levels are used. For ozone and water vapor an additional conversion is necessary since the concentrations are given as mass mixing ratio. Using that the mass m of a gas equals its mol mass M times the *number of its moles n* allows to rewrite Eq. (1.2) into:

$$\frac{n_i}{n_{\text{tot}}} = \frac{m_i}{M_i}\frac{M_{\text{tot}}}{m_{\text{tot}}} = \frac{m_i}{m_{\text{tot}}}\frac{M_{\text{tot}}}{M_i} = \frac{V_i}{V_{\text{tot}}} \tag{2.2a}$$

Using the mol mass of dry air $M_{\text{air}} = 28.97\,\text{g}\,\text{mol}^{-1}$, the mol mass of ozone $m_{\text{ozone}} = 48.00\,\text{g}\,\text{mol}^{-1}$, as well as the mol mass of water vapor $m_{\text{water}} = 18.02\,\text{g}\,\text{mol}^{-1}$ yields [Wallace and Hobbs 2006]:

$$\frac{V_{\text{ozone}}}{V_{\text{air}}} = 0.60\frac{m_{\text{ozone}}}{m_{\text{air}}} \tag{2.2b}$$

$$\frac{V_{\text{water}}}{V_{\text{air}}} = 2.88\frac{m_{\text{water}}}{m_{\text{air}}} \tag{2.2c}$$

The reanalysis has a horizontal resolution of 0.75° times 0.75°. The WEGC CLImatology Processing System 2 (CLIPS2) was used compute 10° zonal means. In the process each latitude band was area-weighted with the cosine of the latitude [Ladstädter 2014]. The vertical pressure coordinate was interpolated to the CPG to match the other data sets. For more information about ERA-Interim see, e.g. Poli et al. [2010], Dee et al. [2011], and Simmons et al. [2014].

---

[1]information about the coverage can be found at www.ecmwf.int/research/era

[2]http://apps.ecmwf.int/datasets/, accessed January 2014

3. Methods

3.1. Notation and basic equations

This section introduces the mathematical notation used in the rest of the work. Moreover it covers the equations needed for the further processing of the data. The notation is based on the conventions of the programming language *Python*, which was used for computation (i.e. all indices start with 0). The *measurand X* (i.e. an ozone, temperature, or water vapor data set) depends on three independent variables, the *latitude* ϕ, the *pressure p*, and the *time t*. All three variables are discrete, hence

$$\phi \to \phi_i = -85°, -75°, \ldots \quad \text{for } i = 0, 1, \ldots$$
$$p \to p_j = 450\,\text{hPa}, 400\,\text{hPa}, \ldots \quad \text{for } j = 0, 1, \ldots$$
$$t \to t_k = 1979\text{-Jan}, 1979\text{-Feb}, \ldots \quad \text{for } k = 0, 1, \ldots \tag{3.1}$$

where ϕ_i is the center of a latitude band (negative values represent southern latitudes), p_j is a pressure level, and t_k is a time step. The *discretised dependent variable* $X_{\phi,p,t}$ is then given by:

$$X(\phi, p, t) \to X(\phi_i, p_j, t_k) \equiv X_{\phi,p,t} \tag{3.2}$$

Handling missing data

As discussed in chapter 2 not all data sets cover the entire altitude, latitude, and time range. Within *Python* missing data are marked as Not A Number (NAN) which are omitted in calculations. In the following the *number of available measurements N* will be used. E.g. $N_{\phi,p}$ is the number of time steps minus the number of time steps marked as NAN at a certain ϕ and p.

Temporal means

The time is different from the other two independent variables as it runs over three different periods. This will be described in more detail in the next chapter and the time period over which t runs is not specified here. Note however that all variables,

which depend on the sum over a certain time range, depend on the selection of this range.

The time average or *climatology* $X_{\phi,p}^{\text{Clim}}$ of a mesurand is given by:

$$X_{\phi,p}^{Clim} = \frac{1}{N_{\phi,p}} \sum_t X_{\phi,p,t}, \tag{3.3}$$

where $X_{\phi,p}^{\text{Clim}}$ gives the mean state of $X_{\phi,p,t}$ within a selected time range. It is obvious that the climatology depends on this range and changes when, e.g., running from 1979 to 1996 instead of 1997 to 2012. This is especially true under changing climate conditions.

A special form of $X_{\phi,p}^{\text{Clim}}$ is the *mean annual cycle* $X_{\phi,p,t''}^{\text{AnnCycle}}$. To calculate it t is split in two variables, namely the *years* t_l' and the *months* t_m'':

$$t_k = \begin{cases} t_l' = 1979, 1980, \ldots & \text{for } l = 0, 1, \ldots \\ t_m'' = \text{Jan}, \text{Feb}, \ldots, \text{Dec} & \text{for } m = 0, 1, \ldots, 11 \end{cases} \tag{3.4}$$

and with this the annual cycle is given by:

$$X_{\phi,p,t''}^{\text{AnnCycle}} = \frac{1}{N_{\phi,p,t''}} \sum_{t'} X_{\phi,p,t',t''}, \tag{3.5}$$

where $N_{\phi,p,t''}$ represents the number of available measurements at a certain latitude, pressure level, and month.

Differences

Subtracting the mean annual cycle from the data yields the *de-seasonalized time series* $X_{\phi,p,t}^{\text{Deseas}}$:

$$X_{\phi,p,t',t''}^{\text{Deseas}} = X_{\phi,p,t',t''} - X_{\phi,p,t''}^{\text{AnnCycle}} \quad \text{for each } t' \tag{3.6}$$

In Eq. (3.6) the mean annual cycle is removed from the mesurand for each year t' separately. This eliminates the first main source of natural variability. $X_{\phi,p,t}^{\text{Deseas}}$ will be used for all subsequent calculations.

To detect systematic differences between the data sets they are compared to each other. This is done for different products such as the climatology or the de-seasonalized time series. Generally, the *difference* X^{Diff} of a variable X *with respect to* a variable Y is defined as (all dependencies are omitted here):

$$X^{\text{Diff}} = X - Y \tag{3.7}$$

3.2. Multiple linear regression

For the trend estimation a multiple linear regression model is used, which includes a constant and a linear term as well as main sources of natural variability, such as the QBO, the ENSO, and the solar flux (c.f. section 1.3). Natural variability is represented by proxies, i.e., the $30\,\mathrm{hPa}$ zonally averaged monthly averaged wind at the equator Q representing the QBO, the Nino3.4 index E representing ENSO, and the $10.7\,\mathrm{cm}$ radio flux index F representing the solar flux. The *regression model* $X_{\phi,p,t}^{\mathrm{Mod}}$ is then defined by:

$$X_{\phi,p,t}^{\mathrm{Mod}} = a_{\phi,p}^{\mathrm{const}} + a_{\phi,p}^{\mathrm{linear}}\, t + a_{\phi,p}^{\mathrm{QBO}}\, Q_{t+\Delta t_{\phi,p}} + a_{\phi,p}^{\mathrm{ENSO}}\, E_{t-3} + a_{\phi,p}^{\mathrm{Flux}}\, F_t, \qquad (3.8\mathrm{a})$$

where $a_{\phi,p}^{\mathrm{const}}$, $a_{\phi,p}^{\mathrm{linear}}$, $a_{\phi,p}^{\mathrm{QBO}}$, $a_{\phi,p}^{\mathrm{ENSO}}$, and $a_{\phi,p}^{\mathrm{Flux}}$ are the regression coefficients (generally $a_{\phi,p}^{s}$ hereafter). Note that not all terms on the right hand side are at the same time step t due to the QBO and the ENSO lags. The *QBO lag* $\Delta t_{\phi,p}$ depends on latitude and altitude as indicated by the indices. The selection of the lags will be discussed in section 3.3 below.

The water vapor regression uses a simplified model, containing only the constant and the trend term, hence:

$$X_{\phi,p,t}^{\mathrm{Mod}} = a_{\phi,p}^{\mathrm{const}} + a_{\phi,p}^{\mathrm{linear}}\, t \qquad (3.8\mathrm{b})$$

Subtracting the model from the de-seasonalized time series yields the *residuum* $r_{\phi,p,t}$:

$$r_{\phi,p,t} = X_{\phi,p,t}^{\mathrm{Deseas}} - X_{\phi,p,t}^{\mathrm{Mod}} \qquad (3.9)$$

Now the regression coefficients are determined by a least squares approach

$$\mathrm{RV}_{\phi,p} = \sum_t r_{\phi,p,t}^2 \xrightarrow{a_{\phi,p}^s} \min!, \qquad (3.10)$$

where RV is the *Residual Variance*. Eq. (3.10) varies the regression parameter in oder to minimize RV. Practically the $a_{\phi,p}^s$ are computed using the `OLS` (ordinary least squares) function of the Python module `statsmodels` (version 0.5.0).[1] In the next chapter also relative coefficients will be used, hence:

$$a_{\phi,p}^{s,\mathrm{rel}} = \frac{a_{\phi,p}^s}{X_{\phi,p}^{Clim}} \qquad (3.11)$$

---

[1]A documentation as well as the current version can be found online under http://statsmodels.sourceforge.net/.

Validity of the model

A simple quality check of the regression model is achieved by computing *Explained Variance (EV)* and the not explained RV of the *Total Variance (TV)*:

$$\underbrace{\sum_t \left(X_{\phi,p,t}^{\mathrm{Deseas}} - X_{\phi,p}^{\mathrm{Clim}}\right)^2}_{\mathrm{TV}_{\phi,p}} = \underbrace{\sum_t \left(X_{\phi,p,t}^{\mathrm{Mod}} - X_{\phi,p}^{\mathrm{Clim}}\right)^2}_{\mathrm{EV}_{\phi,p}} + \underbrace{\sum_t \left(X_{\phi,p,t}^{\mathrm{Deseas}} - X_{\phi,p,t}^{\mathrm{Mod}}\right)^2}_{\mathrm{RV}_{\phi,p}} \quad (3.12)$$

The *coefficient of determination* $R_{\phi,p}^2$ is then:

$$R_{\phi,p}^2 = \frac{\mathrm{EV}_{\phi,p}}{\mathrm{TV}_{\phi,p}} = 1 - \frac{\mathrm{RV}_{\phi,p}}{\mathrm{TV}_{\phi,p}} \in [0,1] \quad (3.13)$$

$R_{\phi,p}^2$ specifies the amount of variability in $X_{\phi,p,t}^{\mathrm{Deseas}}$ which is explained by the model $X_{\phi,p,t}^{\mathrm{Mod}}$. The model is considered good at explaining the variability if the coefficient of determination exceeds a threshold value. In the following this threshold will be taken as 0.25. To examine the significance of the received trends the methods described in section 3.4 below are used.

3.3. QBO and ENSO lag

In section 1.3.2 the QBO and its characteristics have been introduced. The QBO index at the 30 hPa (24 km) level is used to remove the QBO related variability. Downward propagation of a certain QBO state takes about 1 month per kilometer altitude. Thus, shifts between ozone (temperature) and the corresponding index get larger with increasing altitude. This requires an extension of the index beyond 2014. But also at the 30 hPa level the QBO index derived from wind measurements is not in phase with temperature and ozone (Fig. 1.8). Closer analysis reveals that the temperature is actually in phase with the wind shear rather than the wind itself. The wind shear has a phase shift with regard to the wind by a quarter period which corresponds to approximately 6 to 8 months. At a fixed location changes from easterlies to westerlies with time are associated with positive temperature anomalies and vice versa [Randel et al. 1999; Baldwin et al. 2001]. This is explained further e.g. in Dunkerton [2002] by connecting the horizontal wind shear to vertical components. For ozone the lag is smaller, ranging from 4 to 6 months. Moreover the more complex ozone chemistry and dynamics lead to a change from positive to negative anomalies corresponding to westerly wind at approximately 27 km.

To get a clear lag pattern $\Delta t_{\phi,p}$ (cf. Eq. (3.8a)) is calculated from the longest available time series for temperature and ozone, i.e., from the ECMWF (1979 to 2012)

and GOZCARDS (1985 to 2012) data sets, respectively. Several different methods for the identification of the lag have been investigated. It was found that the selection process requires a certain amount of a priori information to ensure physically correct results (such as positive coefficients for the regression of the tropical temperature). At the 30 hPa level possible lags for temperature and ozone from zero to twelve months are allowed. To account for the downwards propagating nature of the QBO this lag range is shifted by one month per kilometer. For each lag the regression model was fitted to the data and the lag which lead to the largest EV (largest $R^2_{\phi,p}$) was chosen as lag for the corresponding latitude and altitude. Fig. 3.1a (right) shows the derived QBO index-temperature lag (solid line) in the 0° to 10° latitude band for different pressure (altitude) levels. The gray shading indicates the allowed lag range at a certain height. The horizontal dashed line marks 30 hPa, where the wind lags the temperature by 5 months. This lag is in good agreement with the findings of the studies discussed above [e.g., Randel et al. 1999]. The left panel of Fig. 3.1a show the lag distribution for all latitudes (x-axis) and altitudes (y-axis). Shaded in blue corresponding to negative lags, in red corresponding to positive lags.

Fig. 3.1b shows the lag from the QBO index to ozone. In general, a similar pattern as for the temperature is found. At 30 hPa the index lags the ozone by 4 months in the 0° to 10° latitude band. Note the anomaly around 15 hPa (30 km), where the selected lag reaches the boundary of the allowed lag. In this region the index-ozone correlation switches from positive to negative and no clear QBO signal can be found in this region.
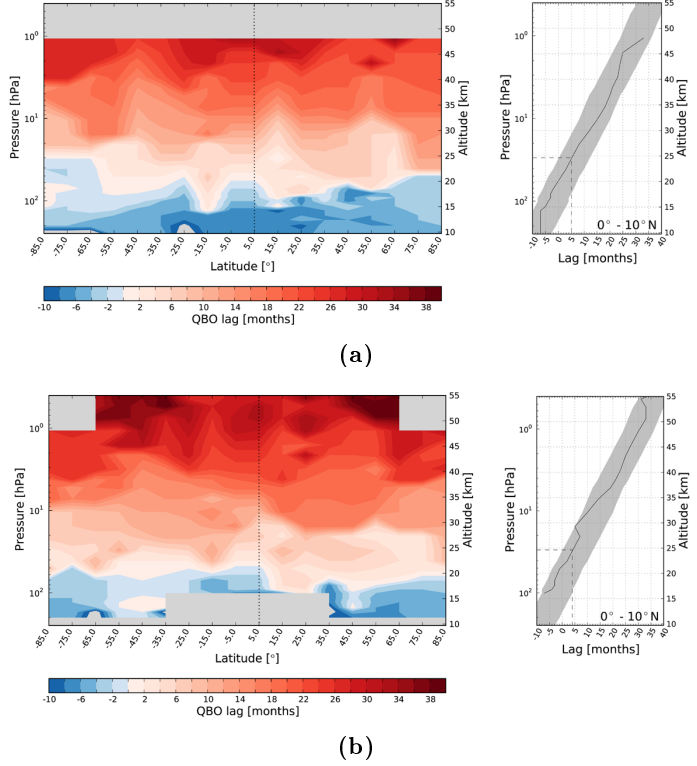
Regarding ENSO, the lag of the Nino3.4 index to temperature and ozone was set to -3 months for the entire stratosphere, following an analysis of Steiner et al. [2013b] and in agreement with Randel et al. [2009].

3.4. Significance testing

The t-distribution

To test the significance of the *linear trend* $a^{\text{linear}}_{\phi,p}$ a two sided Student's t-test is used. It is based on the Student's t-distribution, which arises if the sample variance (rather than the true, but unknown variance of the population) is used for the standardizing of a finite sample of measurements of a normally distributed variable. The *sample size* $n_{\phi,p}$ is given by the Degrees Of Freedom (DOF) which are calculated as the

(a)

(b)

Figure 3.1.: The lag of the QBO index to ERA-Interim temperature (a) and GOZCARDS ozone (b). The latitude and altitude dependence is shown in the left panels. The section of the 0° to 10° band is denoted by the dotted line and extracted in the right panel. The gray shading indicates the physically allowed lag range (same for all latitudes).

number of available measurements $N_{\phi,p}$ minus the number of regression coefficients $a_{\phi,p}^s$:

$$n_{\phi,p} = N_{\phi,p} - 5 \quad (-2 \text{ for water vapor}) \tag{3.14}$$

With this the *probability density function* $f(n_{\phi,p}, x)$ of the standardized Student's t-distribution is given by (the ϕ and p dependencies of n are omitted in the next 3 equations):

$$f(n,x) = \frac{\Gamma\left(\frac{n+1}{2}\right)}{\sqrt{n\pi}\,\Gamma\left(\frac{n}{2}\right)} \left(1 + \frac{x^2}{n}\right)^{-\frac{n+1}{2}},$$

$$\mu = 0,$$

$$\sigma = \sqrt{\frac{n}{n-2}} \quad \text{for } n > 2, \tag{3.15}$$

where Γ is the *Gamma-function* and x the *random variable*. μ and σ are the corresponding *expectation value* and *standard deviation* of the distribution. For large DOF, Eq. (3.15) converges into the *standardized normal distribution*:

$$f(n \to \infty, x) \longrightarrow \frac{1}{\sqrt{2\pi}} e^{-\frac{x^2}{2}},$$

$$\mu = 0,$$

$$\sigma = 1. \tag{3.16}$$

In the case of a normally distributed sample the significance of the mean value can be expressed by the standard deviation, which corresponds to well defined probabilities (e.g., about $68.3\,\%$, $95.5\,\%$, and $99.7\,\%$ of the data lie within 1, 2, and 3 standard deviations around the mean, respectively). The standard deviation of the t-distribution depends on the DOF $n_{\phi,p}$. For the t-test a theoretical *critical t-value* $t^{\mathrm{crit}}(n_{\phi,p}, \alpha)$ is defined by

$$\int_{-t^{\mathrm{crit}}}^{t^{\mathrm{crit}}} f(n, x)\,\mathrm{d}x = \alpha \tag{3.17}$$

so that $\alpha\,\%$ of the t-distributed data lay within $\pm t^{\mathrm{crit}}(n_{\phi,p}, \alpha)$. The corresponding *t-value of the trend* $t_{\phi,p}^{\mathrm{linear}}$ is given by:

$$t_{\phi,p}^{\mathrm{linear}} = \frac{a_{\phi,p}^{\mathrm{linear}}}{\Delta a_{\phi,p}^{\mathrm{linear}}}, \tag{3.18}$$

where $\Delta a_{\phi,p}^{\mathrm{linear}}$ is the *standard deviation of the trend*. Therefore, the t-value gives the number of standard deviations the trend differs from zero. To calculate $\Delta a_{\phi,p}^{\mathrm{linear}}$ first the *standard deviation of the residua* $\Delta r_{\phi,p}$ is computed following Eq. (3.19) (the mean of $r_{\phi,p,t}$ equals zero by definition):

$$\Delta r_{\phi,p} = \sqrt{\frac{\sum_t r_{\phi,p,t}^2}{n_{\phi,p}}} \tag{3.19}$$

$\Delta a_{\phi,p}^{\mathrm{linear}}$ then follows as the square root of the corresponding entry in the covariance matrix scaled with $r_{\phi,p,t}^2$ or as the square root of the `cov_params(scale=dr)` function from *Pythons* `statmodels` module (see the documentation for more information).

The significance levels in this work are also based on the t-distribution. The $\alpha\,\%$ *confidence interval* $\delta a_{\phi,p}^{linear}(\alpha)$ is given by

$$\delta a_{\phi,p}^{linear}(\alpha) = \Delta a_{\phi,p}^{linear} \times t^{crit}(n_{\phi,p}, \alpha) \tag{3.20}$$

so that within $a_{\phi,p}^{linear} \pm \delta a_{\phi,p}^{linear}(\alpha)$ lay $\alpha\,\%$ of the data.

Hypothesis test

Another way to interpret $t_{\phi,p}^{\text{linear}}$ follows from the hypothesis test, which is carried out here to test the significance of the trend. As indicated at the beginning of this section the significance test is based on the assumption that the tested values are random samples from a normally distributed population. The true expectation value μ and standard deviation σ are unknown. The *null hypothesis* H_0 now assumes that the true trend is zero, hence $\mu = 0$. The true standard deviation σ is approximated by the sample standard deviation $\Delta a_{\phi,p}^{\text{linear}}$. In this context Eq. (3.18) given below describes a kind of standardization where $a_{\phi,p}^{\text{linear}}$ is the expectation value of the (not standardized) sample distribution and $t_{\phi,p}^{\text{linear}}$ its standardized counterpart:

$$\frac{a_{\phi,p}^{\text{linear}} - \mu}{\sigma} \longrightarrow \frac{a_{\phi,p}^{\text{linear}}}{\Delta a_{\phi,p}^{\text{linear}}} = t_{\phi,p}^{\text{linear}} \tag{3.18}$$

To reject the null hypothesis $t_{\phi,p}^{\text{linear}}$ has to lay outside of the $\alpha\,\%$ confidence intervals $\pm t^{crit}(n, \alpha)$ from the standardized t-distribution with $n_{\phi,p}$ DOF, hence

$$\left| t_{\phi,p}^{\text{linear}} \right| \stackrel{!}{>} t^{\text{crit}}(n_{\phi,p}, \alpha). \tag{3.21}$$

If this holds true a trend is considered statistically significant at the $\alpha\,\%$ level.

Auto-correlation

Eq. (3.14) gives the simplest approach to calculate the DOF $n_{\phi,p}$. It leads however to a biased outcome of the hypothesis testing, if the measurands (and their corresponding residua) are auto-correlated. In order to obtain accurate results with the t-test the effect of the auto-correlation has to be removed. An easy and often used approach is to use the *effective sample size* $n_{\phi,p}^{\text{eff}}$:

$$n_{\phi,p}^{\text{eff}} = n_{\phi,p}\, \frac{1 - \rho_{\phi,p}}{1 + \rho_{\phi,p}}, \tag{3.22}$$

where ρ is the *correlation parameter* reaching from -1 (perfect anticorrelation) to 1 (perfect correlation). For $\rho = 0$ there is no correlation and n^{eff} equals n. The correlation parameter can be calculated in different ways, here the Durbin-Watson statistic is used [Wilks 2006]. ρ is computed for a lag 1 correlation by

$$\rho_{\phi,p} = 1 - \frac{\sum_{t>0} \left(r_{\phi,p,t} - r_{\phi,p,t-1} \right)^2}{2 \sum_t r_{\phi,p,t}^2}. \tag{3.23}$$

n^{eff} is used in the calculation of t^{crit} in Eq. (3.17) as well as for t^{linear} in Eq. (3.19). Note however that there are also several other ways to remove the effects of correlation. Even using the simple approach via the effective sample size allows different

options. It is possible to calculate ρ not from the residua but directly from X^{Deseas}, leading to slightly different results. Moreover the effective sample size may only be used for the calculation of t^{linear} but not for t^{crit}. For a more detailed study see Santer et al. [2000] and references therein.

4. Results

Here the results of the investigation of the data sets presented in chapter 2 are given. This includes an analysis of the mean atmospheric state and the mean annual cycle for ozone and temperature in different time periods. Moreover the findings of the trend analysis are presented and the different data sets are compared to each other. Due to the emission restrictions for ODSs introduced by the Montreal Protocol ozone decline started to slow down in the 1990s. The scientific literature agrees that the trend reversal occurred in the mid 90s and ozone is recovering since [Steinbrecht et al. 2006; Jones et al. 2009; IPCC 2013; Kyrölä et al. 2013; Tegtmeier et al. 2013]. In this work the *depletion period* reaches from January 1979 to December 1996, hence covering an 18 year period. The *recovery period* covers 16 years from January 1997 to December 2012. A special focus is given to the 11 year period from January 2002 to December 2012, for which RO temperature data are available (*RO period* hereafter). In the following the extraction of the trends for the depletion and the recovery period will be described to set a framework for the more detailed study of the RO period in section 4.3.
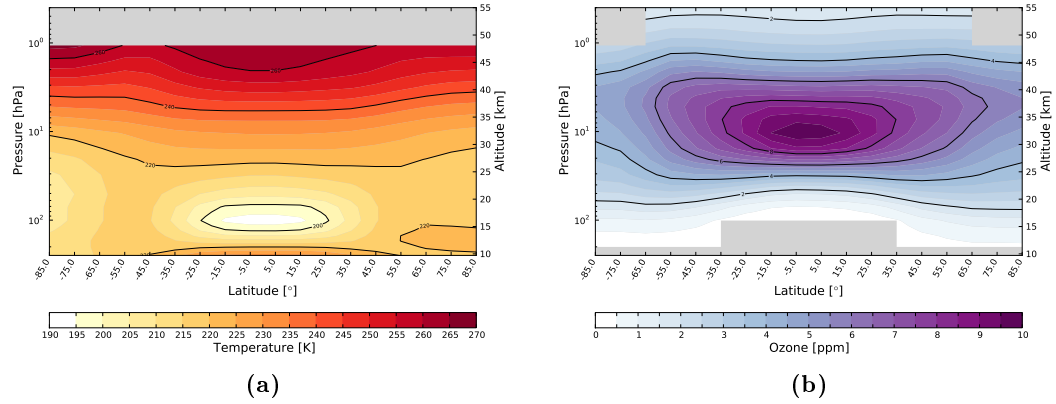
4.1. The state of the atmosphere

4.1.1. Climatologies

The climatology or mean state of an atmospheric variable within a certain time range is calculated applying Eq. (3.3). Fig. 4.1 shows two example climatologies for the period from 1979 to 2012. Fig. 4.1a shows the temperature climatology for ERA-Interim. The lowest temperatures are found in the tropical tropopause from $15\,\mathrm{km}$ to $20\,\mathrm{km}$ and within $\pm 25°$ latitude. In the MS to US the temperature increases to $260\,\mathrm{K}$. Note the slightly cooler temperatures in the southern polar LS, in comparison to the northern hemisphere due to the effects of the stronger Antarctic polar vortex and the ozone hole.

The mean ozone concentration from 1979 to 2012 is shown in Fig. 4.1b for the GOZ-CARDS data set. The ozone concentration increases rapidly above the tropopause until it peaks between $30\,\mathrm{km}$ and $35\,\mathrm{km}$ at low latitudes. In the US ozone concentration decreases again with altitude. The distribution is mostly symmetric with

Figure 4.1.: Mean atmospheric state from 1979 to 2012 as function of latitude and altitude: ERA-Interim temperature (a) and GOZCARDS ozone (b). Missing data are given in gray.
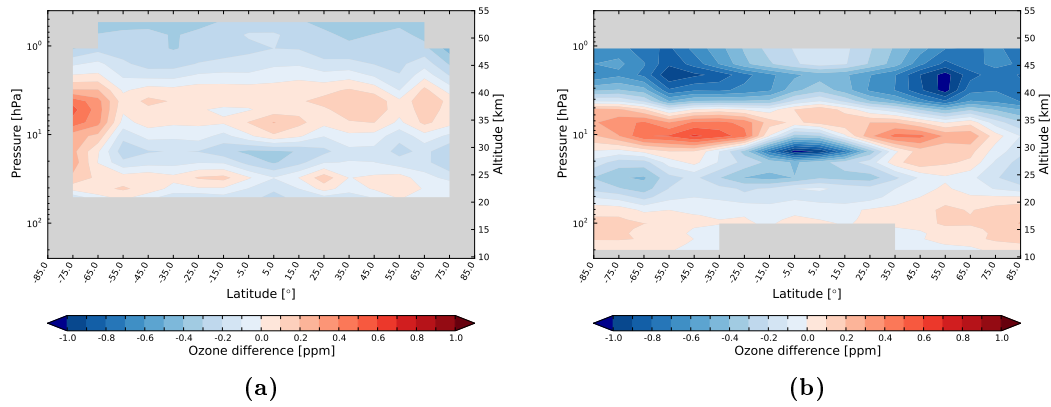
respect the equator, but at high latitudes the southern hemisphere ozone is slightly lower.

Fig. 4.2 shows the difference of the SBUV (a) and ERA-Interim (b) ozone climatologies with respect to GOZCARDS, following Eq. (3.7). SBUV shows generally good agreement and ozone concentrations lie within ± 0.3 ppm in most of the stratosphere. At high southern latitudes larger positive anomalies up to 0.6 ppm are found. Negative anomalies slightly exceeding -0.3 ppm are visible just below the ozone maximum in MS and above 45 km outside the tropics. The differences show a clear altitude-dependent pattern. The strong ozone increase towards the maximum in the MS and US is somewhat underestimated by SBUV compared to GOZCARDS. On the other hand the peak concentrations between 30 km and 40 km are higher in the SBUV data set. This may be due to the lower vertical resolution of the SBUV data set, which is based on nadir measurements, with respect to the limb measurements used for the GOZCARDS data set.

The difference of ERA-Interim ozone to GOZCARDS, visible in Fig. 4.2b, shows a similar pattern, however with an up to three times larger amplitude. The positive anomaly at southern polar latitudes does not appear in ERA-Interim, but strong negative differences of about -1 ppm are found at 30 km in the tropics and above 40 km at mid latitudes.

4.1.2. Annual cycle

Fig. 4.3 shows the mean annual cycle calculated after Eq. (3.5) for ERA-Interim temperature (top) and GOZCARDS ozone (bottom) at two selected latitudes. Note

Figure 4.2.: Difference of the mean atmospheric state (1979 to 2012) with respect to GOZCARDS ozone: SBUV (a) and ERA-Interim (b) ozone.
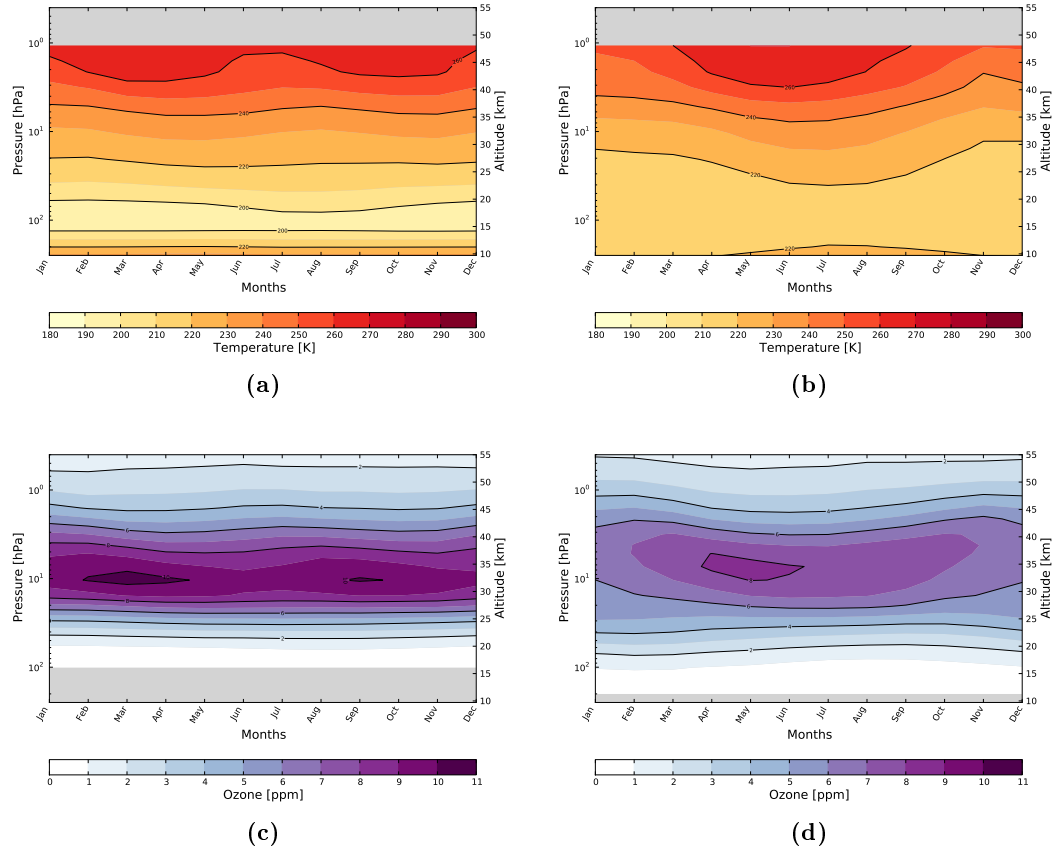
the different colorbar compared to Fig. 4.1 for both, temperature and ozone. The tropical temperature visible in Fig. 4.3a shows hardly any annual variability in the LS and MS. In the US a semi-annual cycle can be identified. At mid latitudes, represented by the 40° to 50° latitude band shown in Fig. 4.3b, an annual cycle is found in the entire stratosphere. The mean annual cycle for all latitudes is shown in Fig. A.10 and Fig. A.11 in the appendix. The strongest annual variations are seen at high latitudes beyond the Arctic and Antarctic circle (see Fig. A.10). They result from the absence of sunlight during the polar nights and the subsequent build up of the polar vortex. The annual cycle of ozone is similar to that of temperature. At low latitudes a weak semi-annual cycle is visible (Fig. 4.3c), while seasonal changes dominate the mid latitudes (Fig. 4.3d).

4.1.3. De-seasonalized anomaly time series

Removing the mean annual cycle from the data via Eq. (3.6) yields the de-seasonalized anomaly time series. At low latitudes the QBO signal becomes evident in most of the data sets. Fig. 4.4 shows de-seasonalized anomaly time series for the 0° to 10° latitude band. The ERA-Interim temperature in Fig. 4.4a shows a clear ∼2-year cycle of cold and warm anomalies in the entire LS and MS, reaching down to about 15 km.

The ozone data reveal a more diverse picture. GOZCARDS ozone (Fig. 4.4b) shows a clear downward propagating QBO signal in most of the LS and MS. At about 27 km a phase shift in the anomalies occurs. This phenomenon is linked to the change from dynamical ozone control in the LS to chemical ozone control in the MS

45

(a)   (b)

(c)   (d)
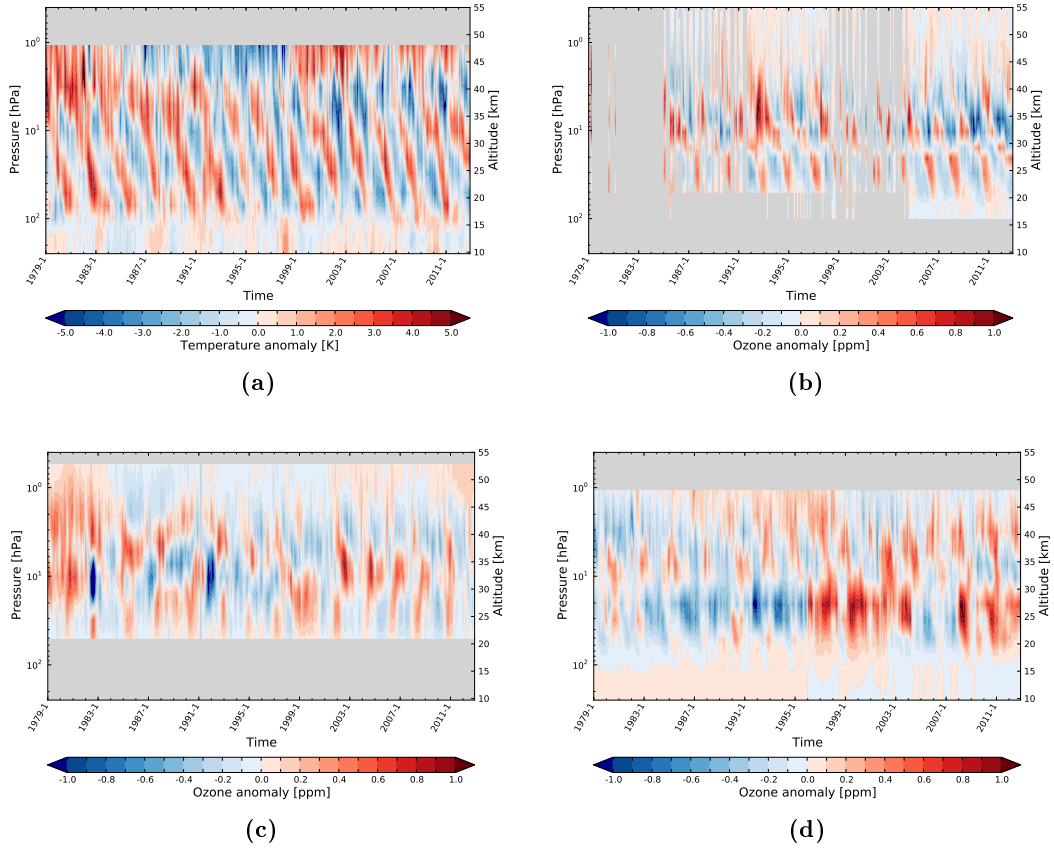
Figure 4.3.: Mean annual cycle from 1979 to 2012 for ERA-Interim temperature (top) and GOZCARDS ozone (bottom) for the 0° to 10° (left) and the 40° to 50° (right) latitude band.

and US [Randel and Thompson 2011; Bourassa et al. 2014]. Fig. 4.4c and Fig. 4.4d show SBUV and ERA-Interim ozone, respectively. The 2-year QBO pattern and the switch at approximately 27 km are also identifiable for these two data sets, however less clear. In particular ERA-Interim seems not to be able to resolve most of the QBO variability in stratospheric ozone. Moreover a change from mostly negative ozone anomalies to mostly positive ozone anomalies occurs from 1995 to 1996 in the ERA-Interim data but not in the other two ozone data sets. ERA-Interim ozone trends should therefore be interpreted with care.

Note that before 1985 the coverage of GOZCARDS is very sparse (gray areas in Fig. 4.4b). Still, for the climatology and the annual cycle calculations, the whole 1979 to 2012 period was used to conserve consistency with the other data sets. For

Figure 4.4.: De-seasonalized time series in the 0° to 10° latitude band for ERA-Interim temperature (a) as well as GOZCARDS (b), SBUV (c), and ERA-Interim (d) ozone.

the trend analysis in the depletion period however, GOZCARDS will be used only from 1985 onwards.

4.2. The ozone depletion and recovery period

As mentioned at the beginning of this chapter the scientific literature states that the emission restrictions for ODSs in 1986 have resulted in an ozone trend reversal in the mid 1990s. If looking at linear trends of ozone and related quantities it is therefore reasonable to compute trends separately for the depletion and for the recovery period. Here 1996/1997 was chosen as turning point, following, e.g., Steinbrecht et al. [2006], IPCC [2013], and Kyrölä et al. [2013]. As suggested, e.g., by Jones et al. [2009] a more detailed approach would require several separate turn around points for different altitudes and latitudes. Moreover is it reasonably to assume that the turn around

Figure 4.5.: Global total column ozone deviations relative to the 1964 to 1980 ground based time average. The represented data sets are given on the right hand side of the plot. Adapted from WMO [2011].

did not happen from on full year to another, hence monthly time resolution should be used.

Fig. 4.5 shows the global total column ozone evolution from the 1960s onwards as presented in the last *Scientific Assessment of Ozone Depletion* [WMO 2011]. The anomalies are calculated as deviation from the ground based average from 1964 to 1980. During this time the total column ozone measured from the ground showed no obvious trend (black line in Fig. 4.5). The trend reversal in the 1990s is visible as clear minimum in all data sets. The ozone increase in the late 1990s follows however a stagnation in the last decade, when looking at integrated ozone.
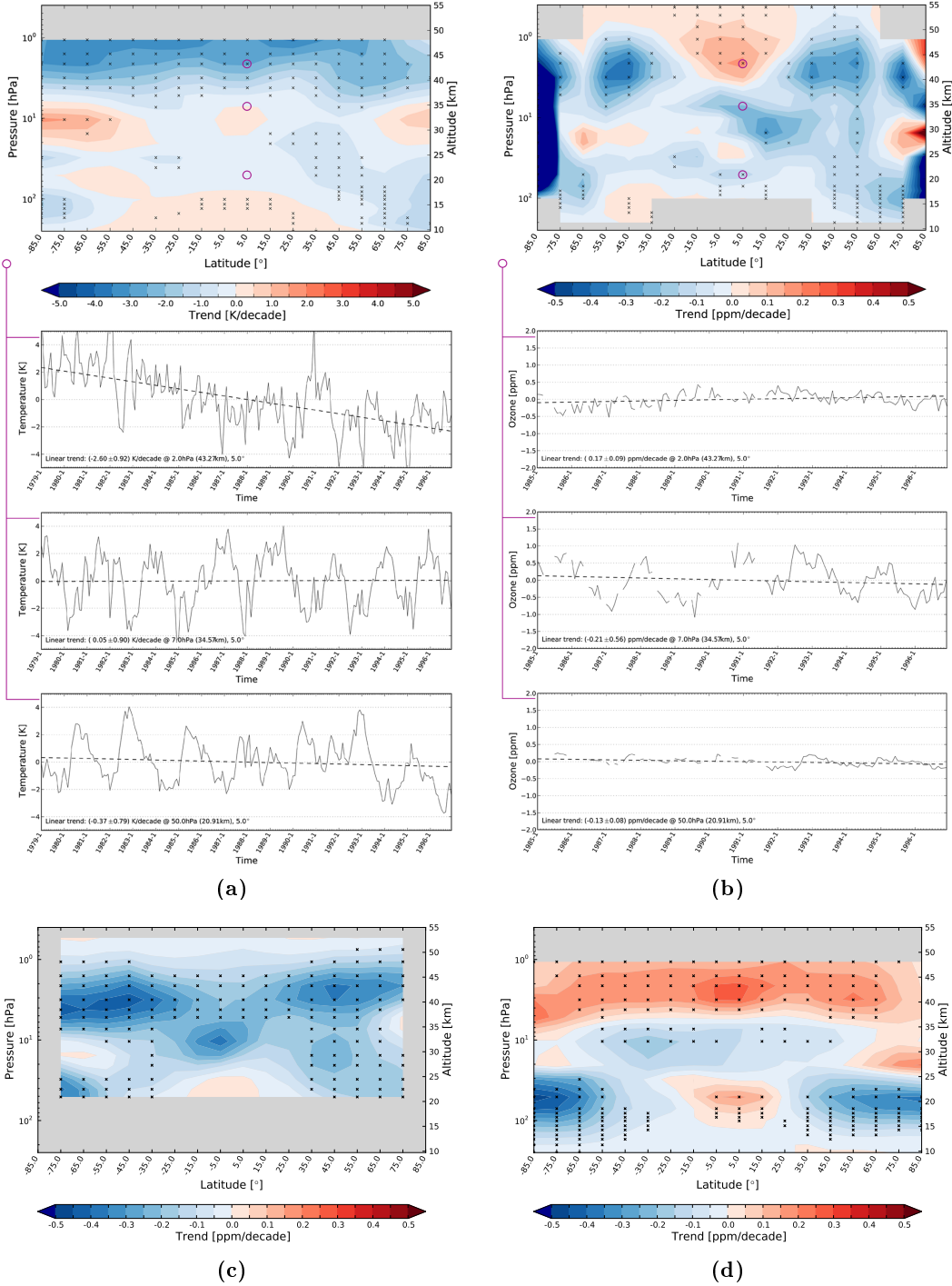
4.2.1. The ozone depletion period

In the depletion period reaching from 1979 to 1996 (1985 to 1996 for GOZCARDS) ozone is declining over large areas of the stratosphere as a result of anthropogenic ODSs. Fig. 4.6 shows the results of the regression study for different data sets. The significance test is based on the auto-correlation corrected t-test explained in section 3.4. Statistically significant trends on the 95 % level are indicated by an ×. Note that the marks also give an indication on the vertical resolution of the data.

Fig. 4.6b (top), Fig. 4.6c, and Fig. 4.6d show consistent negative ozone trends below ~35 km for GOZCARDS, SBUV, and ERA-Interim, respectively. In the tropical tropopause region slightly positive trends appear, especially ERA-Interim shows a statistically significant ozone trend at about 20 km. Other studies also found indications that LS tropical ozone might have increased regionally before 1997 [Jones et al. 2009; Kyrölä et al. 2013].

At mid latitudes all three data sets show a statistically significant ozone decrease over large parts of the stratosphere, only ERA-Interim ozone trends are positive above 35 km. GOZCARDS ozone increases above 35 km in the tropics, while SBUV shows negative trends in the entire MS and US. In the LS ozone concentrations

Figure 4.6.: Trends per decade for the ozone depletion period (1979 to 1996): ERA-Interim temperature (a) as well as GOZCARDS (1985 to 1996) (b), SBUV (c), and ERA-Interim (d) ozone. Regions with trends significant at the 95 % level are marked with an × sign. For ERA-Interim temperature (a) and GOZCARDS ozone (b) three selected de-seasonalized anomaly time series are shown for specific levels: 2 hPa, 7 hPa, and 50 hPa (from top to bottom). Note the different time span for GOZCARDS ozone.
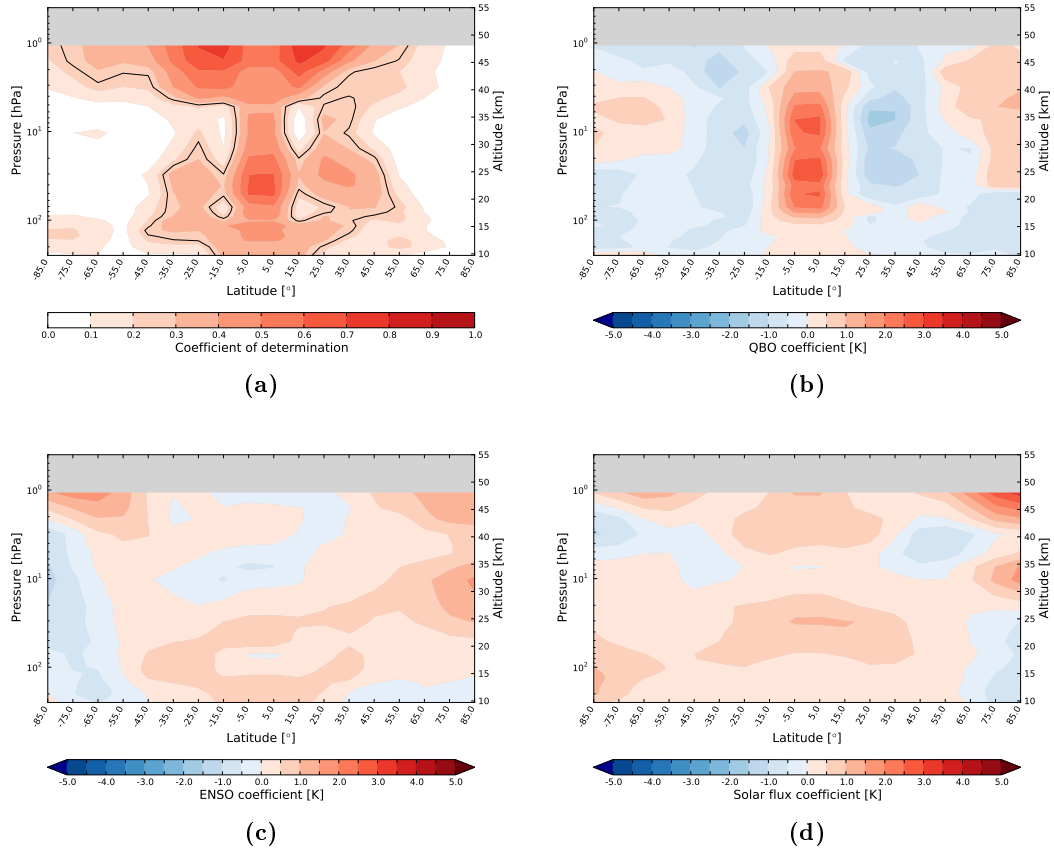
are generally small, therefore only weak signals are found when looking at absolute trends. Thus, also relative ozone trends in % decade^{-1} are shown in the appendix for ERA-Interim, GOZCARDS, and SBUV (Fig. B.3f, Fig. B.4f, and Fig. B.5f). When put into perspective of the total ozone concentration the trend signals in the LS become much more distinct.

For three selected pressure levels (2 hPa, 7 hPa, and 50 hPa) in the tropics (0° to 10°) the de-seasonalized anomaly time series and the corresponding trends are shown in Fig. 4.6b (bottom). Note the high ozone variability at 35 km in comparison to the low changes at higher and lower altitudes. The trend values and the 95 % confidence intervals for the three pressure levels are (0.17 ± 0.09) ppm decade^{-1} (2 hPa), (-0.21 ± 0.57) ppm decade^{-1} (7 hPa), and (-0.13 ± 0.08) ppm decade^{-1} (50 hPa). The strong QBO variability at 7 hPa leads to the high uncertainty intervals at this pressure level.

The temperature trends during the ozone depletion period are shown in Fig. 4.6a for ERA-Interim. The US shows significant cooling of up to $\sim$3 K decade^{-1} at almost all latitudes. In the MS and LS an asymmetry is visible between the hemispheres. While hardly any significant trend is found near the equator and at southern latitudes, the northern mid latitudes show a statistically significant cooling trend of $\sim$1 K decade^{-1}. For compleneness also relative temperature trends were computed. The trend pattern is fully consistent with absolute temperature trends shown in Fig. B.1f. Fig. 4.6a (bottom) shows the de-seasonalized temperature anomaly time series for the same three pressure levels as for GOZCARDS. The overall variability is more homogenous when compared to ozone. While at 22 km and 35 km a distinct QBO signal is visible in the data, the 43 km anomaly time series shows no clear pattern.

Fig. 4.7a shows the coefficient of determination for the ERA-Interim temperature regression in the ozone depletion period. High values are found at all altitudes close to the equator as well as at mid latitudes in the US. In the MS low values are located at 15°S and 15°N. To further investigate the low coefficient of determination outside the $\pm$10° latitude band Fig. 4.7b to Fig. 4.7d show the regression coefficients for the QBO, ENSO, and the solar flux, respectively. As described, e.g., by Baldwin et al. [2001] the QBO influence is largest directly at the equator but has subsequent maxima between 20° to 40° in both hemispheres. The low QBO regression coefficients just outside the $\pm$10° band is reflected in the coefficient of determination. Overall, the contribution of the QBO to variability of both, temperature and ozone decreases rapidly towards high latitudes. To keep the regression model (Eq. (3.8a)) as general and as simple as possible the QBO index was nevertheless included in the regression for all latitude zones. In regions where no QBO influence is present a low coefficient is automatically without any effect in the regression.

(a) **(b)**

(c) **(d)**
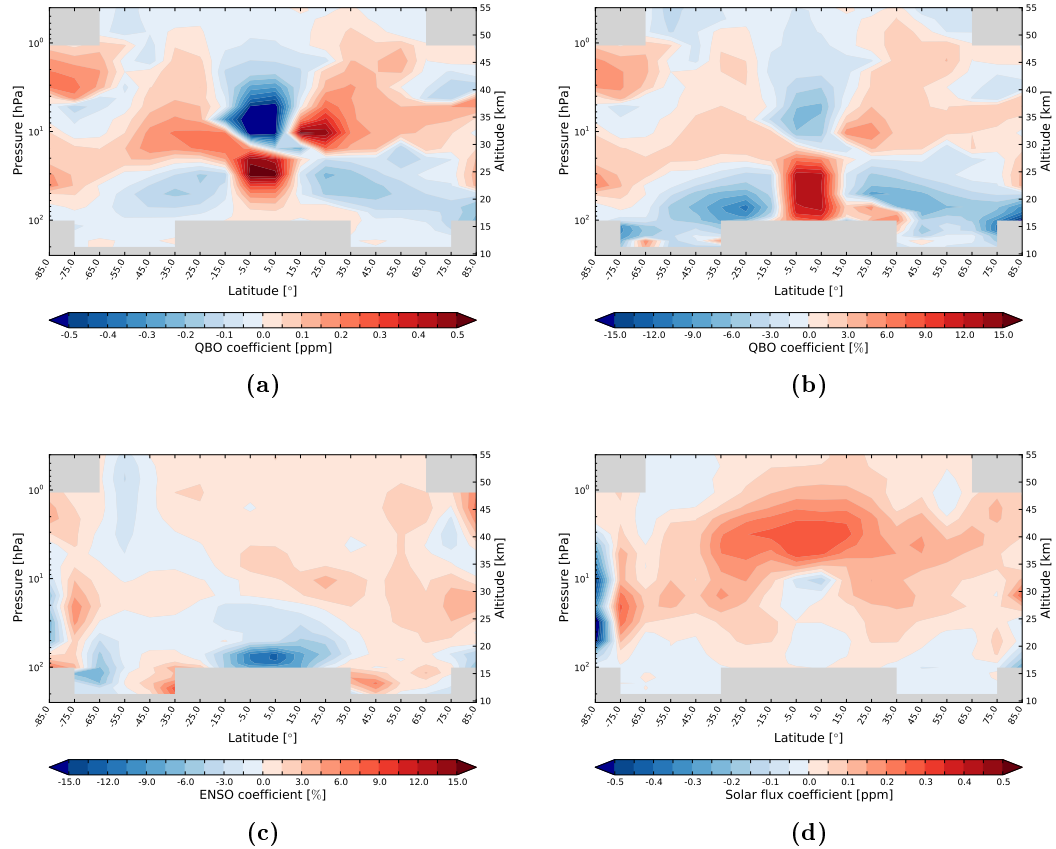
Figure 4.7.: Results of the ERA-Interim temperature regression for the depletion period: coefficient of determination (a) (black line is 0.25) as well as relative QBO (b), ENSO (c), and solar flux (d) coefficient.

The ENSO regression coefficients are shown in Fig. 4.7c. At low latitudes the regression coefficients are positive below 30 km and mainly negative above. The northern high latitudes show positive values over the entire stratosphere, while negative coefficients appear south of $-55°$ latitude in the LS and MS.

The solar flux regression coefficient is positive in most of the stratosphere. Local negative values appear above 30 km especially towards higher latitudes and in the polar LS in the northern hemisphere.

In general the QBO variability dominates most of the low and mid latitudes with amplitudes up to three times larger than ENSO and solar flux. Towards the poles all three coefficients contribute at the same order but explain only a small fraction

Figure 4.8.: Results of the GOZCARDS ozone regression for the depletion period: coefficient of determination (a) as well as relative QBO (b), ENSO (c), and solar flux (d) coefficient.

of the total natural variability ($R^2 < 0.1$).

Fig. 4.8a and Fig. 4.8b show the absolute and relative QBO regression coefficients for the GOZCARDS data set, respectively. Note that the large absolute QBO coefficients between 30 km and 40 km in Fig. 4.8a are distinctively smaller in relative terms (Fig. 4.8b). The change between positive coefficients in the tropical LS and negative coefficients in the MS is due to the phase shift seen in Fig. 4.4b. The pattern is comparable to earlier findings by, e.g., Baldwin et al. [2001] and Eckert et al. [2013]. The absolute ENSO coefficients shown in Fig. 4.8c have a maximum in the low latitude MS, which mostly disappears when looking at it in relative trends (not shown). The solar flux coefficient is positive over most of the stratosphere with a

maximum around 40 km. At high southern latitudes negative coefficients exceeding
-0.5 ppm are found in the LS and MS.

For completeness Fig. B.1 to Fig. B.5 in the appendix show the results of the regression analysis for the ozone depletion period for all data sets, showing the QBO (a), ENSO (b), and solar flux (c) coefficients as well as the coefficient of determination (d). Moreover the absolute (e) and relative (f) trends are given for comparison.

4.2.2. The ozone recovery period
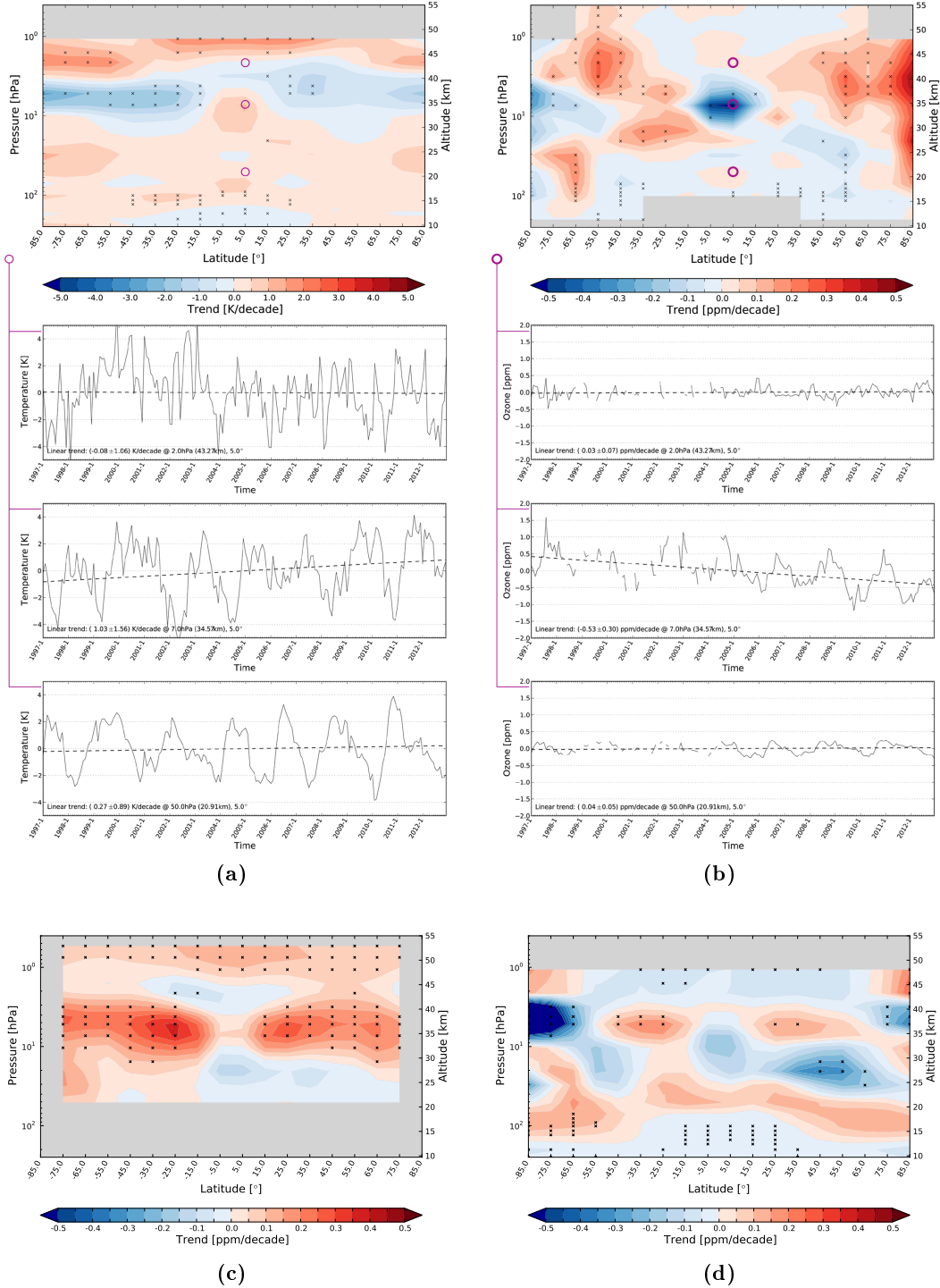
In this work the ozone recovery period is defined from 1997 to 2012 and therefore overlaps with the RO period (2002 to 2012) for about two thirds of the time. Fig. 4.9a shows the temperature change within the recovery period regressed from ERA-Interim. In large areas of the stratosphere the sign of the temperature trend has changed compared to the depletion period. The statistically significant cooling between 15 km and 30 km visible in Fig. 4.6a has changed to a not significant positive trend in the recovery period. From 35 km to 40 km the temperature decreases for both periods while the US shows positive trends during the recovery period. Note the strong natural variability in Fig. 4.9a (bottom) which makes it difficult to detect statistically significant trends.

The ozone trends in the recovery period show similarities as well as some obvious differences among the three data sets (Fig. 4.9b to Fig. 4.9d). At mid latitudes around 35 km a statistically significant and consistent ozone increase is found. SBUV shows the strongest signal with respect to the amplitude as well as the spatial extend, while the ERA-Interim data feature the smallest but still statistically significant positive trends in this area. In the tropical MS an ozone decrease is found, although the amplitude and exact location varies across the data sets. The drop in ozone concentrations in this region is in general agreement with other studies, e.g., Jones et al. [2009], Eckert et al. [2013], Kyrölä et al. [2013], and Gebhardt et al. [2014].
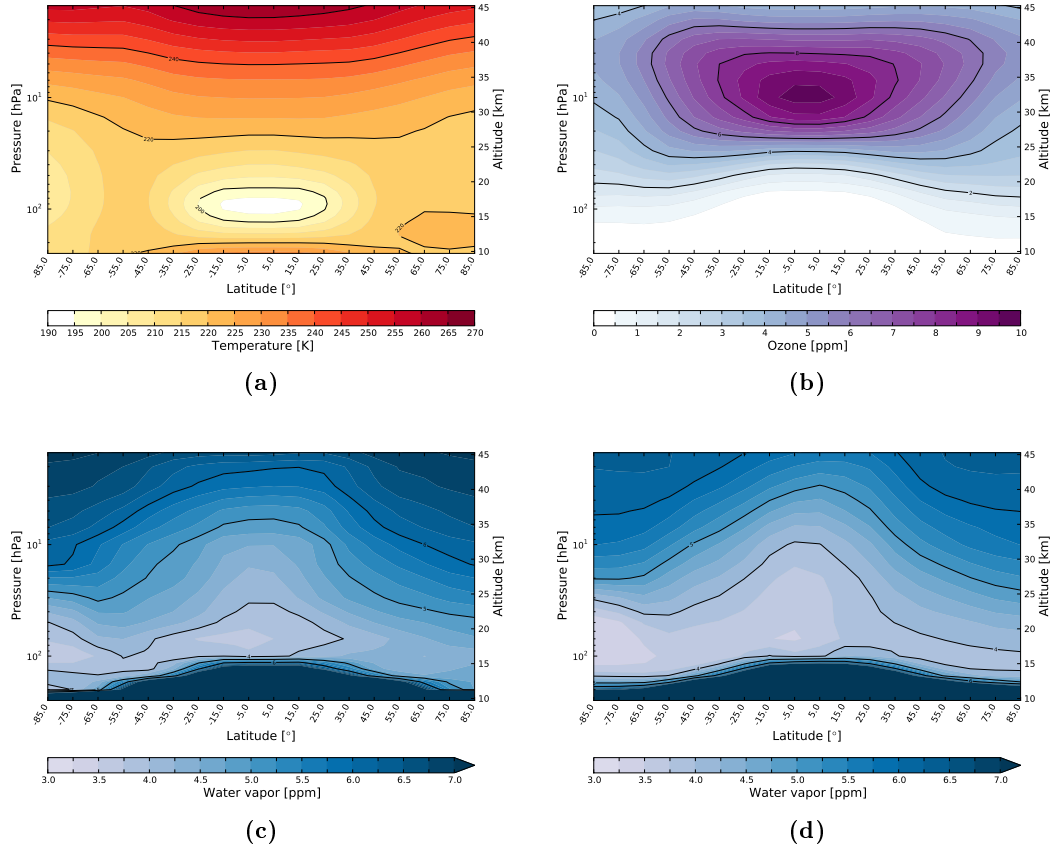
The US ozone trends are inconsistent across the three data sets. ERA-Interim and SBUV both find statistically significant trends but with different signs, while GOZCARDS shows hardly any trend. The LS ozone shows signs of recovery for ERA-Interim as well as in some regions for GOZCARDS and SBUV. However, in the later two data sets also regions with continuing ozone decline can be identified in the LS although most of them are not statistically significant at the 95 % level.

Again Fig. C.1 to Fig. C.5 in the appendix show the results of the regression analysis for the ozone recovery period for all data sets, showing the QBO (a), ENSO (b), and solar flux (c) coefficients as well as the coefficient of determination (d). Moreover the absolute (e) and relative (f) trends are given for comparison.

(a)

(b)

(c)

(d)

Figure 4.9.: Trends per decade for the recovery period (1997 to 2012). ERA-Interim temperature (a) as well as GOZCARDS (b), SBUV (c), and ERA-Interim (d) ozone. Same layout as Fig. 4.6.
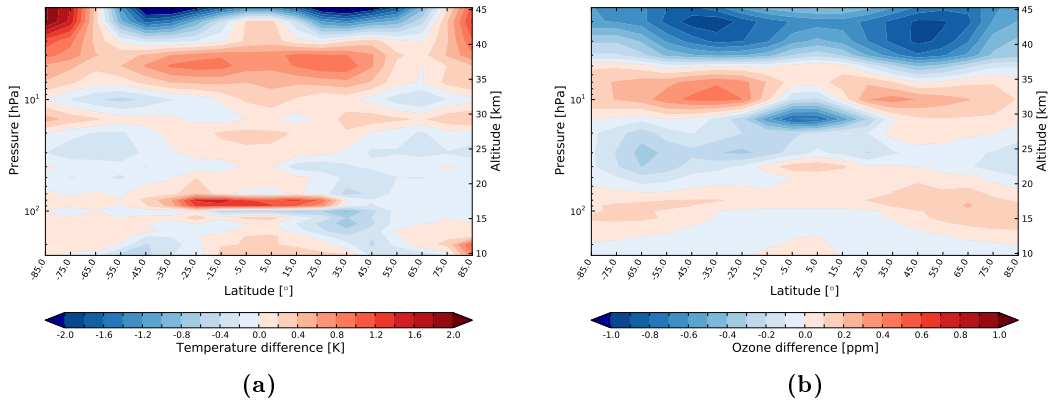
Figure 4.10.: Mean climatology for the RO period (2002 to 2012): RO temperature (a) and HARMOZ ozone (b) as well as GOZCARDS (c) and ERA-Interim (d) water vapor at different latitudes and altitudes.

4.3. The RO period

4.3.1. Data set differences

The RO period covers the time from 2002 to 2012 due to the availability of the RO data set (cf. Fig. A.1). The focus of this section is the comparison of the RO temperature anomaly time series and trends with the other data sets. The top panels of Fig. 4.10 show the mean state of RO temperature (left) and HARMOZ ozone (right) for the RO period calculated after Eq. (3.3). The GOZCARDS and SBUV ozone climatologies are in good agreement with HARMOZ (not shown). The differences are less than 0.4 ppm across the stratosphere. ERA-Interim ozone shows larger discrepancies with respect to HARMOZ, especially in the MS and US (Fig. 4.11b). ERA-Interim temperatures agree well with RO temperatures between
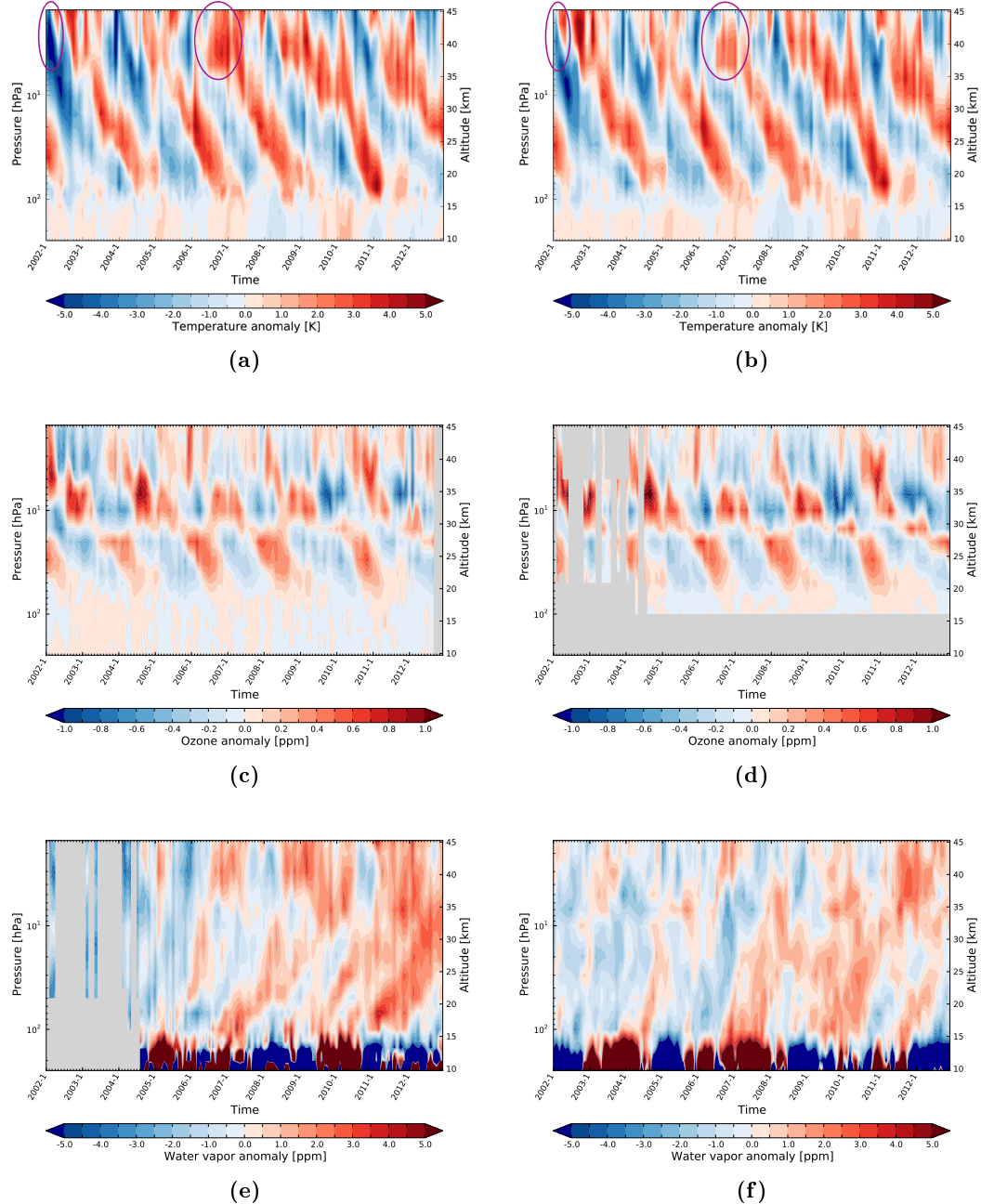
Figure 4.11.: Climatology differences of ERA-Interim temperature (a) and ozone (b) with respect to RO temperature (shown in Fig. 4.10a) and HARMOZ ozone (shown in Fig. 4.10b).

20 km to 35 km, not exceeding 0.4 K difference (Fig. 4.11a). Above a stronger positive difference is visible (ERA-Interim - RO; cf. Eq. (3.7)) followed by a cold bias above 40 km. Chauhan et al. [2009] compared ECMWF *analysis* data to MIPAS and MLS temperatures and also found larger differences above approximately 10 hPa, which the authors contributed to deficits in the ECMWF analysis data. In the tropical tropopause ($\sim$17 km) ERA-Interim temperatures are approximately 1 K higher than RO temperatures.

Fig. 4.10c and Fig. 4.10d show the water vapor climatology for GOZCARDS and ERA-Interim, respectively. Both data sets show a similar pattern with increasing concentrations towards higher altitudes and latitudes in the stratosphere. The low water vapor concentrations in the tropical LS are due to the cold tropopause at low latitudes. As first suggested by Brewer [1949] stratospheric water vapor is mostly controlled by the temperature of the tropical tropopause, where air enters the stratosphere from the troposphere. A more comprehensive study of stratospheric water vapor can be found in Hegglin et al. [2013]. A visualization of the water vapor time series for both the GOZCARDS and ERA-Interim data can be found in the appendix (Fig. A.6 and Fig. A.9).
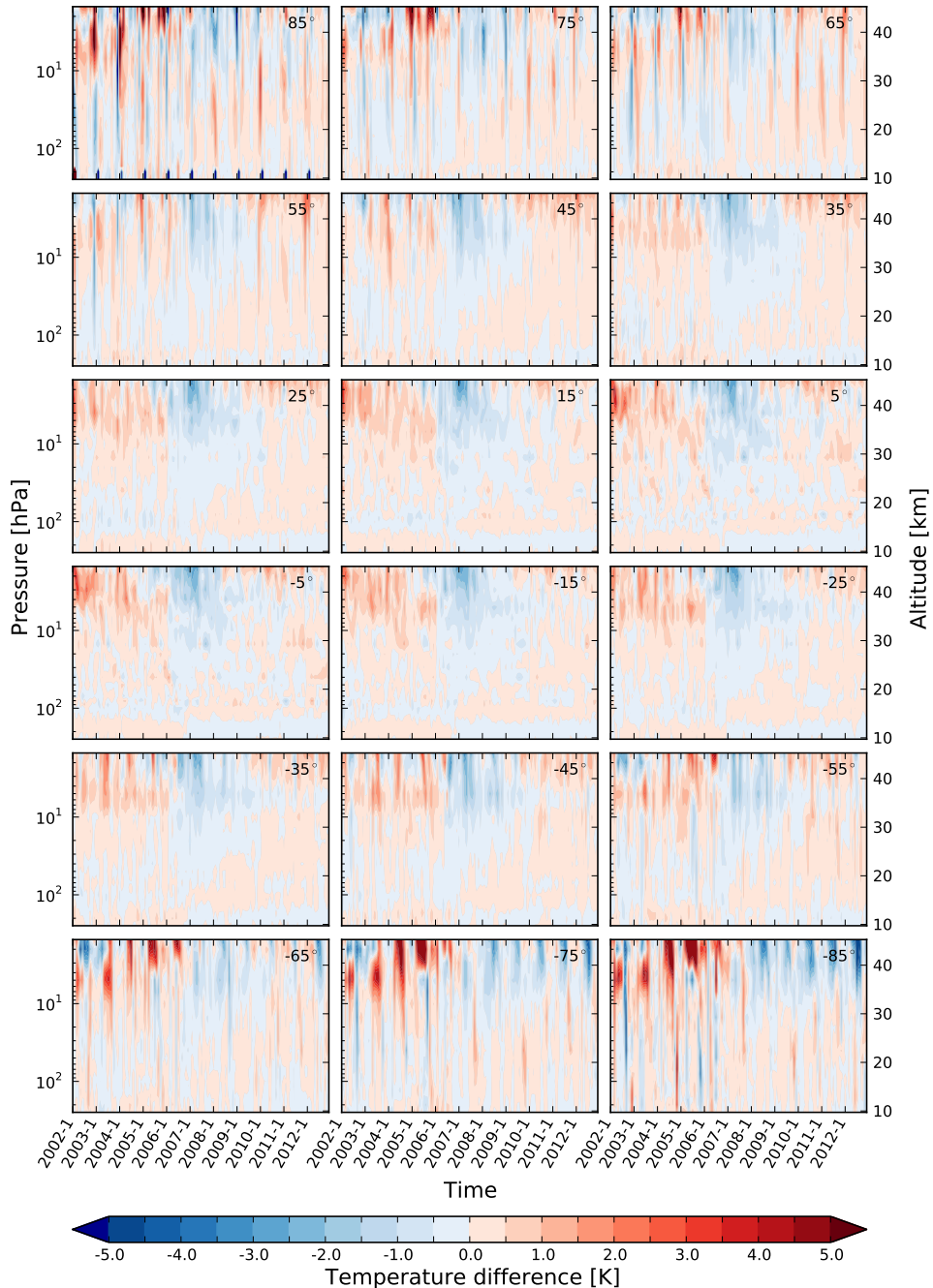
Using Eq. (3.6), the mean annual cycle is removed from each data set, resulting in de-seasonalized anomaly time series presented in Fig. 4.12 for different data sets for the 0° to 10° latitude band. Fig. 4.12a and Fig. 4.12b show de-seasonalized RO and ERA-Interim temperature, respectively. The differences are shown for all latitude bands in Fig. 4.13. In the LS and MS the difference is mostly within ±0.5 K. Largest differences are visible at high latitude showing a pronounced pattern. Another promi-
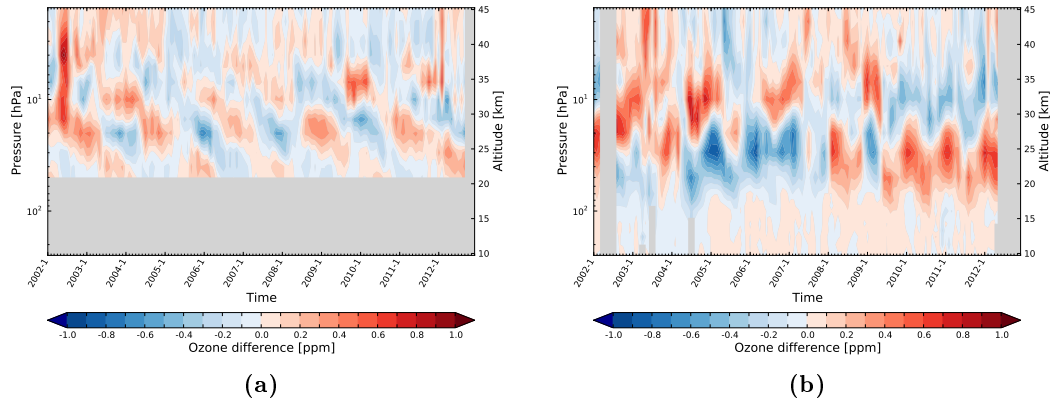
Figure 4.12.: De-seasonalized anomaly time series of RO (a) and ERA-Interim (b) temperature, HARMOZ (c) and GOZCARDS (d) ozone as well as GOZCARDS (e) and ERA-Interim (f) water vapor. Shown is the 0° to 10° latitude band.

Figure 4.13.: ERA-Interim temperature anomaly with respect to RO. The center of the shown latitude band is given in the top right corner of each figure.

Figure 4.14.: (a) Difference of SBUV ozone with respect to HARMOZ for the 0° to 10° latitude band. (b) Difference of ERA-Interim ozone with respect to HARMOZ for the −30° to −20° latitude band.

nent feature is the change of a predominantly positive systematic difference from 2002 to 2006 to a negative systematic difference from 2006 to 2009 in the MS and US. In the RO data set larger temperature anomalies are apparent in 2002 and during 2006 to 2009, which are less pronounced in the corresponding ERA-Interim anomalies (violet circles in Fig. 4.12a and Fig. 4.12b). This leads to the strong negative difference when subtracting RO from ERA-Interim temperatures.

The RS data set reaches only up to approximately 22 km altitude. If compared to the RO temperatures the difference is mostly within ±1 K (not shown). Larger discrepancies only appear in the −10° to 0° latitude band. Here a 2-year pattern, most likely connected to the QBO, can be found. It seems that the RS data set has a slightly higher amplitude for both the warm and cold anomalies. This is however not seen north of the equator. The difference reaches a maximum of approximately 2.5 K between 15 km and 20 km during the strong positive anomalies between 2010 and 2011. A summery of the regression results for the RS data can be found in the appendix Fig. D.3.

Two de-seasonalized anomaly ozone time series are shown in Fig. 4.12c (HARMOZ) and Fig. 4.12d (GOZCARDS). HARMOZ ozone has not been shown before, since it is only available for the period from 2002 to 2012. When compared to GOZCARDS the two data sets show excellent agreement and the differences are mostly within ±0.4 ppm. From 2002 to 2004 the GOZCARDS data set has larger gaps in the coverage and the difference can locally reach up to 1 ppm (not shown).

Fig. 4.14a shows the difference between SBUV and HARMOZ data in the 0° to 10° latitude band. Since SBUV does not capture the QBO well (cf. Fig. 4.4c) but HARMOZ does (cf. Fig. 4.12c) the differences in Fig. 4.14a show the distinct pattern of the QBO close to the equator. At higher latitudes the differences are significantly smaller and are mostly within ±0.4 ppm. The only exception is a strong positive anomaly in the first year of the time series (2002). It is visible in nearly all latitude bands in the MS and US, although stronger in the northern hemisphere. The anomaly origins from low concentration values found in the HARMOZ time series in mid 2002 and higher concentration measured by SBUV.

The ERA-Interim ozone anomaly time series shows larger differences relative to HAR-MOZ. The difference can reach 1 ppm at all latitudes. Fig. 4.14b shows the −30° to −20° latitude band as a representative example for the other latitude bands. An annual cycle can be identified in the difference time series. The changing gradient at approximately 29 km is also visible as a switch from positive to negative anomalies (or vice versa). Moreover the anomalies change from mostly negative (positive) to mostly positive (negative) from 2007 to 2008 below (above) 29 km (also true for all latitude bands). This leads to large trend differences from ERA-Interim to the other data sets (see Fig. 4.17 below).

Fig. 4.12e and Fig. 4.12f show the de-seasonalized water vapor anomalies in the 0° to 10° latitude band for GOZCARDS and ERA-Interim, respectively. The approximately annual variations in the anomalies are connected to the tropical *tape recorder* first suggested by Mote et al. [1996]. Mote and colleges linked the stratospheric water vapor anomaly changes to the tropical annual cycle and confirmed the earlier work from Brewer [1949]. For more information see also Randel et al. [2004] and references therein.
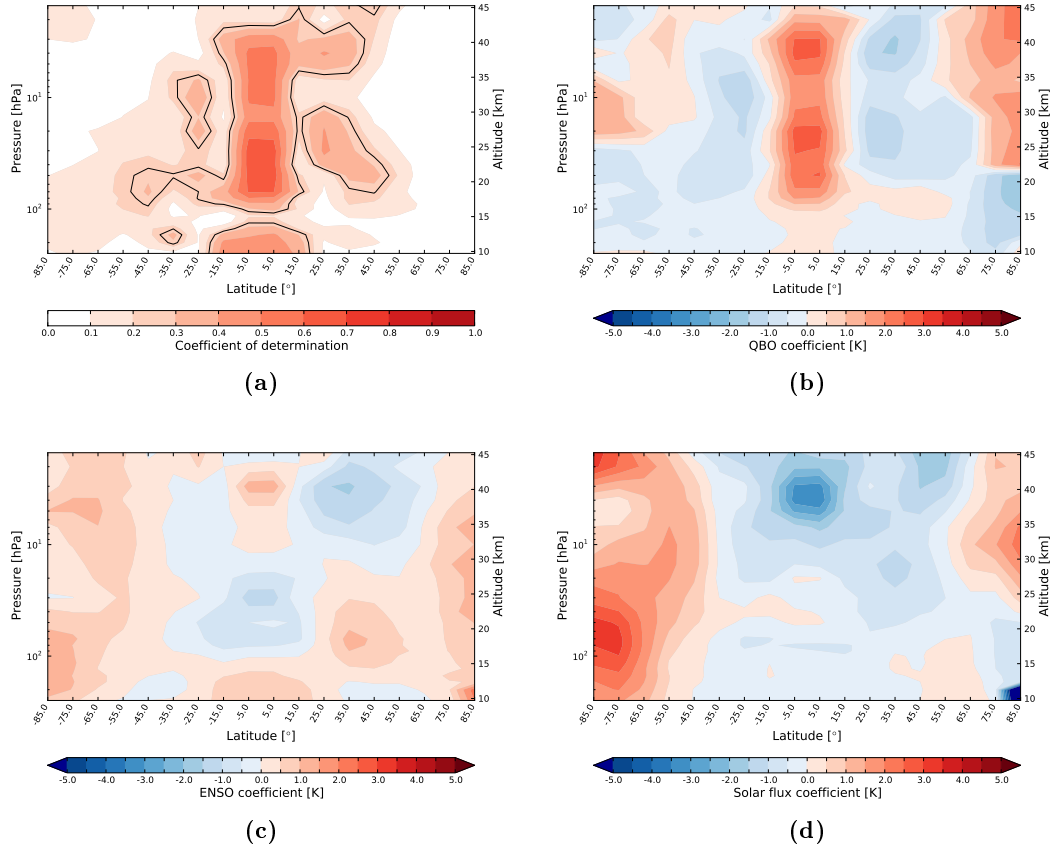
4.3.2. Regression results

Natural variability

From the de-seasonalized anomaly time series the regression coefficients were obtained following Eq. (3.8a) to Eq. (3.10). The Explained Variance (EV) in the RO temperature regression is shown in Fig. 4.15a via the coefficient of determination. The QBO regression coefficient (shown in Fig. 4.15b for RO temperature) is very similar for all three temperature data sets and also consistent with the regression results of other time periods (cf. Fig. 4.7b). In the tropical stratosphere the QBO is positively correlated to the temperature and shows the largest coefficients, while the correlation is negative at mid latitudes and the coefficients are smaller.

The ENSO regression coefficient $a_{\phi,p}^{\mathrm{ENSO}}$ is shown in Fig. 4.15c for the RO temperature regression. It is about a factor 2 lower than QBO coefficients. In the tropics to

(a)   **(b)**

(c)   **(d)**
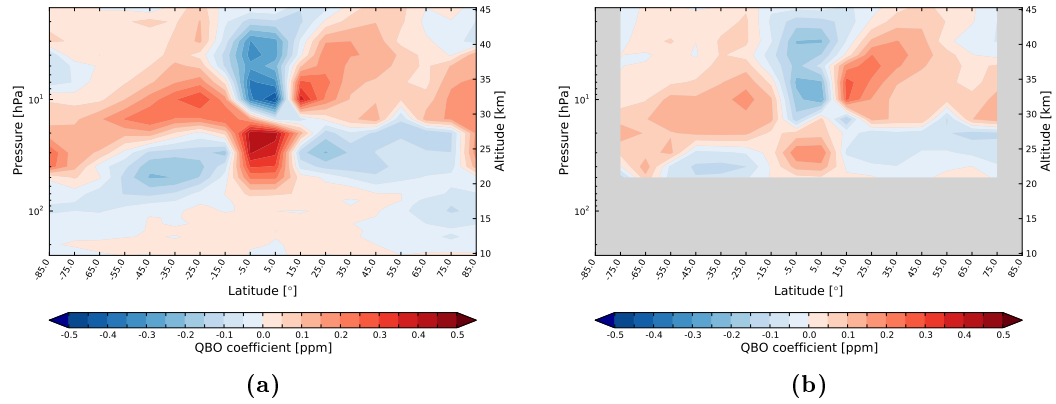
Figure 4.15.: Output values of the RO temperature regression: (a) coefficient of determination, (b) QBO regression coefficient, (c) ENSO regression coefficient, and (d) solar flux regression coefficient.

subtropics a positive ENSO coefficient up to the tropopause shows positive correlation, while the ENSO coefficient becomes negative in the tropical LS and MS. In the northern mid-latitudes above 30 km larger negative coefficients up to 1.5 K appear. The southern hemisphere middle and high latitudes show positive ENSO coefficients in the entire stratosphere.

The solar flux coefficient $a_{\phi,p}^{\mathrm{Flux}}$ is shown in Fig. 4.15d also for the RO regression. While the agreement to ERA-Interim and RS is given in the LS and MS the distinct minimum in the tropical US is not visible in the ERA-Interim regression.

Fig. 4.16a and Fig. 4.16b show the QBO coefficients for the HARMOZ and SBUV time series, respectively. GOZCARDS is in excellent agreement with HARMOZ in the whole stratosphere (not shown). ERA-Interim QBO coefficients have some

Figure 4.16.: QBO regression coefficient for HARMOZ (a) and SBUV (b).

small differences in the MS and US, i.e., the QBO influence in the HARMOZ data set is larger than for ERA-Interim (cf. Fig. D.4a and Fig. D.7a). The SBUV QBO coefficients shown in Fig. 4.16b generally agree with the HARMOZ coefficients in the MS and US but differ from it by a factor 3 in the LS. This discrepancy is attributed to the bad representation of the QBO in the SBUV time series (see Fig. 4.4c).
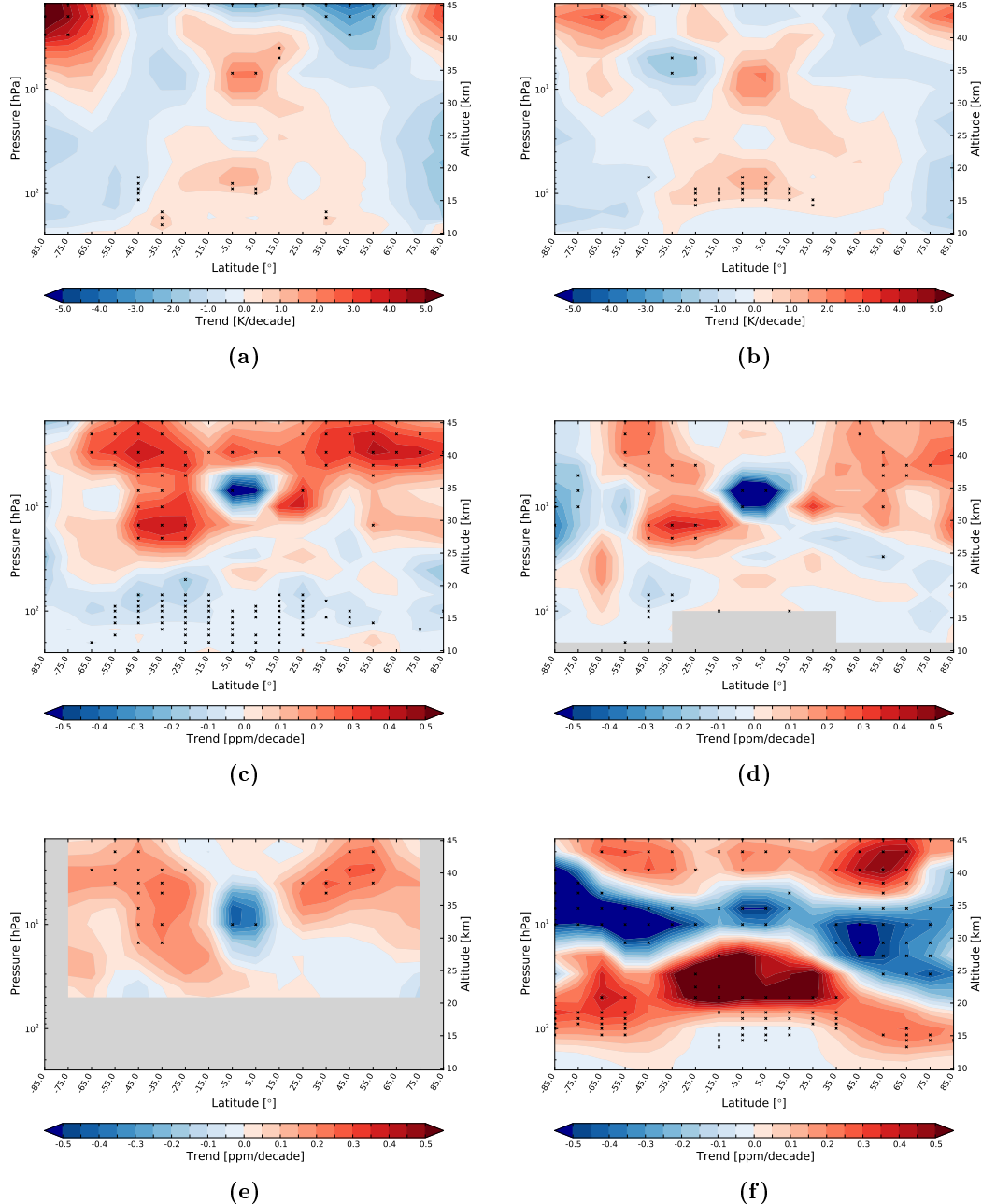
The ENSO coefficients of the four ozone data sets agree reasonably well in the entire stratosphere (cf. Fig. D.4b, Fig. D.5b, Fig. D.6b, and Fig. D.7b).

Trends

Fig. 4.17 shows the trends for all ozone and temperature data sets available for the RO period, except for the RS temperature, which covers only the LS. High agreement is found between the RO (Fig. 4.17a) and ERA-Interim (Fig. 4.17b) temperature trends. The strongest warming signal (around $2\,\mathrm{K\,decade^{-1}}$) is found in the tropical MS at about $30\,\mathrm{km}$ to $35\,\mathrm{km}$. Towards mid latitudes at the same altitude a weak cooling trend is visible in both data sets. In the northern hemisphere US the negative trend exceeds $-3\,\mathrm{K\,decade^{-1}}$ for RO but is slightly smaller and not statistically significant in the ERA-Interim data. Between $20\,\mathrm{km}$ and $30\,\mathrm{km}$ hardly any statistically significant trends are found, except for a weak warming signal in the $20°$ to $30°$ latitude band. In the tropical LS just above the tropopause a significant warming trend is found in both data sets. It extends a bit further to southern mid latitudes and reaches about $1.5\,\mathrm{K\,decade^{-1}}$ near the tropopause at low latitudes.
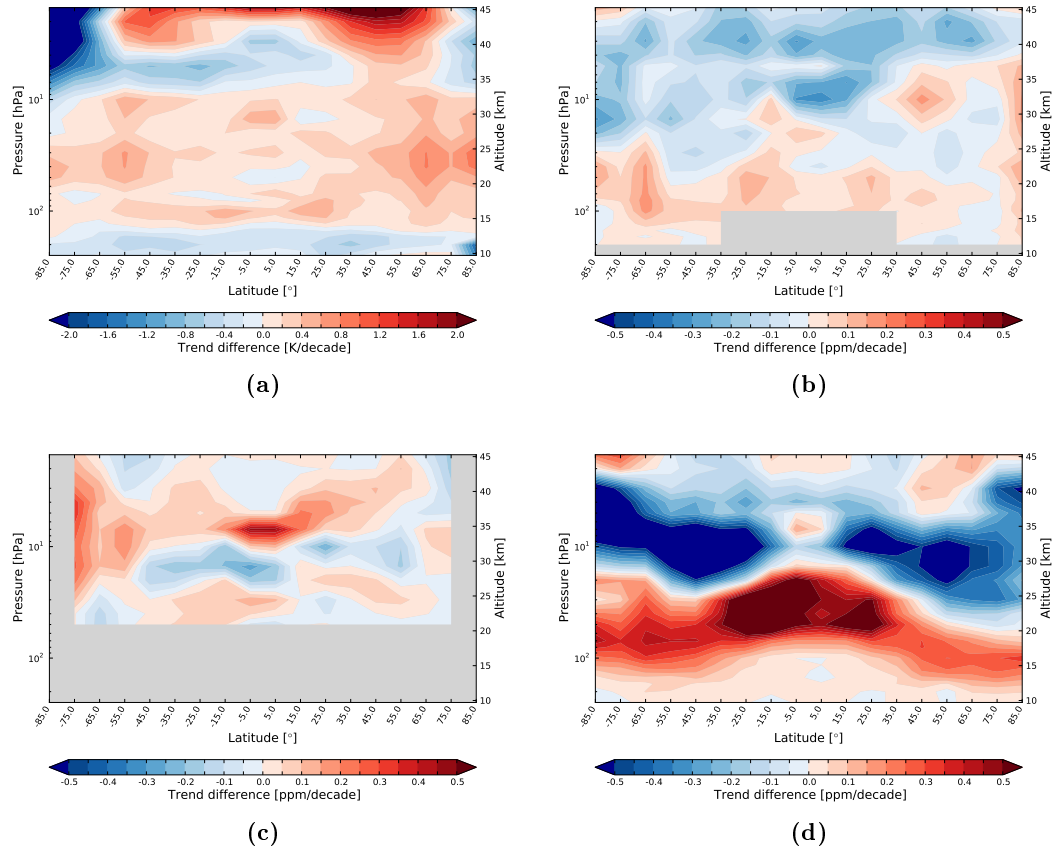
Fig. 4.18a shows the difference between ERA-Interim and RO temperature trends. The differences in the LS and MS trends are mostly within $\pm0.4\,\mathrm{K\,decade^{-1}}$, with the maximum difference slightly exceeding $0.6\,\mathrm{K\,decade^{-1}}$ at high northern latitudes

Figure 4.17.: RO period trends per decade for RO (a) and ECMWF (b) temperature as well as HARMOZ (c), GOZCARDS (d), SBUV (e), and ECMWF (f) ozone. Regions with trends significant at the 95 % level are denoted with an × sign.

(a)

(b)

(c)

(d)
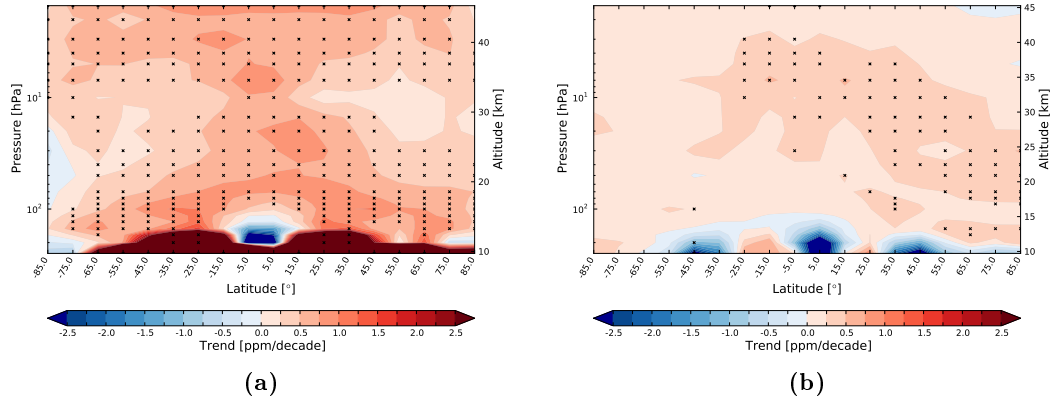
Figure 4.18.: Trend differences in the RO period (2002 to 2012): ERA-Interim minus RO temperature (a) as well as GOZCARDS (b), SBUV (c), and ERA-Interim (d) minus HARMOZ ozone.

near 25 km altitude. In general over all latitudes negative differences are evident below about 15 km, positive differences are found from 15 km to 33 km and negative differences of up to $-1\,\mathrm{K}\,\mathrm{decade}^{-1}$ are apparent from 33 km to 40 km. The larger amplitude of the northern mid-hemisphere US cooling in the RO data leads to positive differences above $2\,\mathrm{K}\,\mathrm{decade}^{-1}$.

The ozone trends (Fig. 4.17c to Fig. 4.17f) show some consistend features across all data sets, but also distinct differences in some regions. The most persistent and noticeable signal is a local decline of ozone at approximately 30 km to 36 km in the tropics (cf. also Fig. 4.9 for the ozone recovery period). Significant negative trends are found in all four data sets, although the amplitudes vary. GOZCARDS shows the strongest trend signal, reaching $-0.77\,\mathrm{ppm}\,\mathrm{decade}^{-1}$. HARMOZ and ERA-Interim agree well with $-0.51\,\mathrm{ppm}\,\mathrm{decade}^{-1}$ and $-0.46\,\mathrm{ppm}\,\mathrm{decade}^{-1}$, respectively. It is

Figure 4.19.: RO period trends per decade for GOZCARDS (a) and ECMWF (b) water vapor. Regions with trends significant at the 95 % level are denoted with an × sign.

however noted again, that the ERA-Interim trends have to be treated and interpreted with care since large discrepancies with respect to the other ozone data sets were found. The weakest but still statistically significant trend signal is found in the SBUV data with $-0.37\,\mathrm{ppm\,decade^{-1}}$. Moreover the decline reaches over a broader altitude range in this data set.

The decline in the tropical MS is embedded into positive trends at higher latitudes. HARMOZ, GOZCARDS, and SBUV data show a consistent ozone increase in the MS and US outside the tropics in both hemispheres. The amplitudes are also in good agreement, ranging between $0.25\,\mathrm{ppm\,decade^{-1}}$ to $0.35\,\mathrm{ppm\,decade^{-1}}$. ERA-Interim agrees with the other data sets in the US but shows a significant ozone decrease in the MS, which is connected to the anomaly change discussed in section 4.1.3. The same holds true for the strong increase in the LS, which exceeds $0.70\,\mathrm{ppm\,decade^{-1}}$ for some regions.

HARMOZ, GOZCARDS, and SBUV data find a small, not-significant increase of tropical LS ozone. Towards mid latitudes HARMOZ and GOZCARDS show some significant negative trends, especially in the southern hemisphere. Fig. 4.18b to Fig. 4.18d show the trend difference with respect to HARMOZ in $\mathrm{ppm\,decade^{-1}}$ for GOZCARDS, SBUV, and ERA-Interim, respectively. ERA-Interim shows large discrepancies in large parts of the stratosphere, partly exceeding $0.5\,\mathrm{ppm\,decade^{-1}}$. GOZCARDS and SBUV show better agreement although SBUV also deviates from HARMOZ by about $0.5\,\mathrm{ppm\,decade^{-1}}$ in some regions.

Finally, Fig. 4.19a and Fig. 4.19b show the water vapor concentration trend for GOZ-CARDS and ERA-Interim regressed with a simple linear regression (Eq. (3.8b)). A simple regression model is used because no clear QBO signal is apparent in the de-

seasonalized anomaly time series of water vapor. An investigation reveals that the trend signal of water water vapor is hardly influenced by the consideration of additional regression terms like QBO, ENSO, and solar flux. Increasing water vapor mixing ratios in the entire stratosphere are found in both data sets. The GOZCARDS trends are about $0.5\,\mathrm{ppm\,decade^{-1}}$ larger than ERA-Interim trends and statistically significant on the $95\,\%$ level in large areas of the stratosphere. A comparison of absolute and relative water vapor trends as well as the coefficient of determination for the regression can be found in the appendix for GOZCARDS (Fig. D.8a, Fig. D.8b, and Fig. D.8c) and ERA-Interim (Fig. D.8d, Fig. D.8e, and Fig. D.8f).

Fig. D.1 to Fig. D.7 in the appendix show the results of the regression analysis for the RO period for the ozone and temperature data sets, showing the QBO (a), ENSO (b), and solar flux (c) coefficients as well as the coefficient of determination (d). Moreover the absolute (e) and relative (f) trends are given for comparison.

5. Summary and discussion

This work surveys global ozone and temperature changes from 1979 to 2012 based on different satellite data sets. The ozone evolution is investigated based on Global OZone Chemistry And Related trace gas Data Records for the Stratosphere (GOZ-CARDS), the National Oceanic and Atmospheric Administration (NOAA) Solar Backscatter UltraViolet (SBUV) instruments, and the HARMonized dataset of OZone profiles (HARMOZ). Temperature time series are based on RadioSondes (RSs) and satellite-based Radio Occultation (RO) measurements. The ECMWF ReAnalysis-Interim (ERA-Interim) field by the European Centre for Medium-Range Weather Forecasts (ECMWF) was also used for both, ozone and temperature.

Trends are calculated for three different periods using a linear regression model. The regression uses proxies to account for the main sources of natural variability. For the Quasi-Biennial Oscillation (QBO) the 30 hPa zonal averaged monthly averaged wind at the equator is used. In agreement with theoretical considerations, e.g., by Baldwin et al. [2001] a 5 month (4 month) lag of the wind index with regard to temperature (ozone) at 30 hPa is found. The downwards propagation of QBO states by about 1 km per month leads to an increase of this lag to above 30 months in the Upper Stratosphere (US). The El Niño–Southern Oscillation (ENSO) is represented by the Nino3.4 index of Sea Surface Temperatures (SSTs), using a constant lag of stratospheric ozone and temperature of 3 months. Finally, the 10.7 cm radio flux represents the solar flux variations.

In the *ozone depletion period* 1979 to 1996 a clear decrease in the ozone concentration is found for the GOZCARDS and NOAA data sets (Fig. 4.6b and Fig. 4.6c). ERA-Interim ozone shows a different trend pattern which does not match the observations (Fig. 4.6d).

The ozone decline is in agreement with several other studies, which have investigated ozone trends for similar time periods. Jones et al. [2009] looked at three different altitude ranges in the 30°S to 30°N as well as the 30° to 60° latitude range in both hemispheres. They found significant ozone decrease in most of the investigated areas for the 1979 to 1997 period. Kyrölä et al. [2013] surveyed vertically resolved ozone profiles and found mostly decreasing ozone values from 1984 to 1997 in most of the stratosphere. The 5th Assessment Report of the Intergovernmental Panel on Climate Change (IPCC AR5) finally states that *"it is certain that global stratospheric ozone*

has declined from pre-1980 values" and that *"most of the decline occurred prior to the mid 1990s"* [IPCC 2013].

Investigating temperature it also shows decrease in most of the stratosphere during the ozone depletion period. The cooling is found strongest in the US, where most of the trend is statistically significant on the 95% level (Fig. 4.6a). This is consisted with the results from Ramaswamy et al. [2001] who also found stratospheric cooling in the 1979 to 1994 period of approximately $-0.6\,\mathrm{K\,decade^{-1}}$ in the Lower Stratosphere (LS) and up to $-4\,\mathrm{K\,decade^{-1}}$ in the US.

Investigation of the *ozone recovery period* from 1997 to 2012 revealed a change in the ozone trends from decline to general increase. The strongest increase was found in the Middle Stratosphere (MS) at middle and high latitudes (Fig. 4.9b and Fig. 4.9c). However, GOZCARDS shows a strong decline in the tropics at $\sim$35 km, which is not visible in the NOAA data. In the recovery period ERA-Interim is in better agreement with the ozone measurements than for the depletion period but still shows significant differences (Fig. 4.9d).

Regarding temperature, a positive increase is found for the recovery period except for a decrease in a 5 km layer centered about 37 km in all latitudes (Fig. 4.9a).

The *RO period* from 2002 to 2012 was chosen due to the availability of the Wegener Center for Climate and Global Change (WEGC) RO temperature data set. This period is moreover covered by a third observational ozone data set (HARMOZ). The three observational ozone data set show good agreement regarding the general evolution pattern in the RO period. Ozone is increasing in the US and in the middle and high latitude MS. A decline is found from 30 km to 35 km in the tropics by all data sets. However, the amplitude of the decline varies by more than 50% (Fig. 4.17c to Fig. 4.17e). The ERA-Interim ozone trends show again large differences with respect to sign and amplitude when compared to the observational data sets.

For the 1997 to 2012 period (and the 2002 to 2012 sub-period) a range of scientific publications investigating the ozone recovery exists. The general increase and the distinct declining feature in the tropical MS is found by several of them [Kyrölä et al. 2013; Eckert et al. 2013; Gebhardt et al. 2014].

The RO and ERA-Interim temperature trends show excellent agreement in most of the stratosphere. Larger differences only appear at high altitudes above 40 km and especially at high southern latitudes (Fig. 4.18a). In general, hardly any significant trend could be detected in 2002 to 2012 due to the strong natural variability (Fig. 4.17a and Fig. 4.17b).

A study by Randel and Thompson [2011] found strong correlation between temperature and ozone in the LS and anti-correlation above approximately 30 km. When

comparing ozone and temperature in the ozone depletion period this anti-correlation pattern above 30 km is also found in this work (Fig. 4.9 and Fig. 4.17). The strongest warming signal in the tropics at ~35 km is in the same region as the strongest ozone decline. Since a direct influence of ozone on temperature would lead to a positive correlation it is assumed that more complex mechanisms (e.g., changes in dynamical patterns, temperature-ozone feedbacks) lead to this anti-correlation pattern.

In general the detection of statistically significant trends is very difficult at low latitudes due to the strong QBO signal (Fig. 4.4a to Fig. 4.4d and Fig. 4.12a to Fig. 4.12d). This is especially true for the comparatively short RO period. The contribution of the QBO variability as identified by the 30 hPa wind proxy can reach 4 K and 0.5 ppm for temperature and ozone, respectively (Fig. 4.15b and Fig. 4.16a and Fig. 4.16b).
This underlines the importance of thoroughly estimating and removing natural variability in vertically high-resolved data sets. It is evident that a proxy which is defined only on a single pressure level such as the 30 hPa winds for the QBO is not sufficient to remove the QBO variability in the entire stratosphere. Therefore further research is necessary to better identify and remove natural variability patterns to isolate significant trends in stratospheric ozone and temperature.

List of Figures

Bibliography

Baldwin, M. P., L. J. Gray, T. J. Dunkerton, K. Hamilton, P. H. Haynes, W. J. Randel, J. R. Holton, M. J. Alexander, I. Hirota, T. Horinouchi, D. B. A. Jones, J. S. Kinnersley, C. Marquardt, K. Sato, and M. Takahashi (2001). 'The quasi-biennial oscillation'. *Rev. Geophys.* 39.2, pp. 179–229. DOI: 10.1029/1999RG000073.

Baldwin, M. P., M. Dameris, and T. G. Shepherd (2007). 'How Will the Stratosphere Affect Climate Change?' *Science* 316.5831, pp. 1576–1577. DOI: 10.1126/science.1144303.

Bhartia, P. K., R. D. McPeters, C. L. Mateer, L. E. Flynn, and C. Wellemeyer (1996). 'Algorithm for the estimation of vertical ozone profiles from the backscattered ultraviolet technique'. *J. Geophys. Res.* 101.D13, pp. 18793–18806. DOI: 10.1029/96JD01165. URL: http://dx.doi.org/10.1029/96JD01165.

Bhartia, P. K., R. D. McPeters, L. E. Flynn, S. Taylor, N. A. Kramrova, S. Frith, B. Fisher, and M. DeLand (2013). 'Solar Backscatter UV (SBUV) total ozone and profile algorithm'. *Atmos. Measur. Tech.* 6.10, pp. 2533–2548. DOI: 10.5194/amt-6-2533-2013.

Blaschek, M. (2009). 'Vergleich von globalen Radiosondentemperaturen mit GPS Okkultationsmessungen'. Diploma thesis. University of Vienna.

Bourassa, A. E., D. A. Degenstein, W. J. Randel, J. M. Zawodny, E. Kyrölä, C. A. McLinden, C. E. Sioris, and C. Z. Roth (2014). 'Trends in stratospheric ozone derived from merged SAGE II and Odin-OSIRIS satellite observations'. *Atmos. Chem. Phys. Discuss.* 14.6, pp. 7113–7140. DOI: 10.5194/acpd-14-7113-2014.

Brewer, M. A. (1949). 'Evidence for a world circulation provided by measurements of helium and water vapor distribution in the stratosphere'. *Quart. J. Roy. Meteor. Soc.* 75, pp. 351–363. DOI: 10.1002/qj.49707532603.

Calvo, N., R. García-Herrera, and R. R. Garcia (2008). 'The ENSO Signal in the Stratosphere'. *Annals of the New York Academy of Sciences* 1146.1, pp. 16–31. DOI: 10.1196/annals.1446.008.

Chang, P. and S. E. Zebiak (2002). 'El Niño and the southern oscillation'. In: *Encyclopedia of Atmospheric Sciences*. Ed. by J. R. Holton, J. Pyle, and J. Curry. Vol. 1. Academic Press, pp. 713–724. ISBN: 978-0-12-227090-1.

Chapman, S (1929). 'A theory of upper-atmospheric ozone'. *Memoirs of the Royal Meteorological Society* 3.26, pp. 102–125.

Chauhan, S., M. Hopfner, G. P. Stiller, T. von Clarmann, B. Funke, N. Glatthor, U. Grabowski, A. Linden, S. Kellmann, M. Milz, T. S. H. Fischer, L. Froidevaux, A. Lambert, M. L. Santee, M. Schwartz, W. G. Read, and N. J. Livesey (2009). 'MIPAS reduced spectral resolution UTLS-1 mode measurements of temperature, O_3, HNO_3, N_2O, H_2O and relative humidity over ice: retrievals and comparison to MLS'. *Atmos. Measur. Tech.* 2, pp. 337–353. DOI: 10.5194/amt-2-337-2009.

Clarmann, T. von, M. Höpfner, S. Kellmann, A. Linden, S. Chauhan, B. Funke, U. Grabowski, N. Glatthor, M. Kiefer, T. Schieferdecker, G. P. Stiller, and S. Versick (2009). 'Retrieval of temperature, H_2O, O_3, HNO_3, CH_4, N_2O, $ClONO_2$ and ClO from MIPAS reduced resolution nominal mode limb emission measurements'. *Atmospheric Measurement Techniques* 2.1, pp. 159–175. DOI: 10.5194/amt-2-159-2009.

Crutzen, P. J. (1970). 'The influence of nitrogen oxides on the atmospheric ozone content'. *Quart. J. Roy. Meteor. Soc.* 96.408, pp. 320–325. DOI: 10.1002/qj.49709640815.

– (1974). 'Estimates of possible future ozone reductions from continued use of fluoro-chloro-methanes (CF_2Cl_2, $CFCl_3$)'. *Geophys. Res. Lett.* 1.5, pp. 205–208. DOI: 10.1029/GL001i005p00205.

Dee, D. P., S. M. Uppala, A. J. Simmons, P. Berrisford, P. Poli, S. Kobayashi, U. Andrae, M. A. Balmaseda, G. Balsamo, P. Bauer, P. Bechtold, A. C. M. Beljaars, L. van de Berg, J. Bidlot, N. Bormann, C. Delsol, R. Dragani, M. Fuentes, A. J. Geer, L. Haimberger, S. B. Healy, H. Hersbach, E. V. Hólm, L. Isaksen, P. Kållberg, M. Köhler, M. Matricardi, A. P. McNally, B. M. Monge-Sanz, J.-J. Morcrette, B.-K. Park, C. Peubey, P. de Rosnay, C. Tavolato, J.-N. Thépaut, and F. Vitart (2011). 'The ERA-Interim reanalysis: configuration and performance of the data assimilation system'. *Quart. J. Roy. Meteor. Soc.* 137.656, pp. 553–597. DOI: 10.1002/qj.828.

DuBois, J. L., R. P. Multhauf, and C. A. Ziegler (2002). *The Invention and Development of the Radiosonde*. Simthsonian Institution Press.

Dunkerton, T. J (2002). 'Quasi-Biennial Oscillation'. In: *Encyclopedia of Atmospheric Sciences*. Ed. by J. R. Holton, J. Pyle, and J. Curry. Vol. 1. Academic Press. ISBN: 978-0-12-227090-1.

Dupuy, E. et al. (2009). 'Validation of ozone measurements from the Atmospheric Chemistry Experiment (ACE)'. *Atmos. Chem. Phys.* 9.2, pp. 287–343. DOI: 10.5194/acp-9-287-2009.

Eckert, E., T. von Clarmann, M. Kiefer, G. P. Stiller, S. Lossow, N. Glatthor, D. A. Degenstein, L. Froidevaux, S. Godin-Beekmann, T. Leblanc, S. McDermid, M. Pastel, W. Steinbrecht, D. P. J. Swart, K. A. Walker, and P. F. Bernath (2013). 'Drift-corrected trends and periodic variations in MIPAS IMK/IAA ozone measurements'. *Atmos. Chem. Phys. Discuss.* 13.7, pp. 17849–17900. DOI: 10.5194/acpd-13-17849-2013.

Elachi, C. and J. van Zyl (2006). *Introduction to the Physics and Techniques of Remote Sensing*. Second edition. John Wiley & Sons.

Eyring, V., I. Cionni, G. E. Bodeker, A. J. Charlton-Perez, D. E. Kinnison, J. F. Scinocca, D. W. Waugh, H. Akiyoshi, S. Bekki, M. P. Chipperfield, M. Dameris, S. Dhomse, S. M. Frith, H. Garny, A. Gettelman, A. Kubin, U. Langematz, E. Mancini, M. Marchand, T. Nakamura, L. D. Oman, S. Pawson, G. Pitari, D. A. Plummer, E. Rozanov, T. G. Shepherd, K. Shibata, W. Tian, P. Braesicke, S. C. Hardiman, J. F. Lamarque, O. Morgenstern, J. A. Pyle, D. Smale, and Y. Yamashita (2010). 'Multi-model assessment of stratospheric ozone return dates and ozone recovery in CCMVal-2 models'. *Atmos. Chem. Phys.* 10.19, pp. 9451–9472. DOI: 10.5194/acp-10-9451-2010.

Foelsche, U., B. Scherllin-Pirscher, F. Ladstädter, A. K. Steiner, and G. Kirchengast (2011). 'Refractivity and temperature climate records from multiple radio occultation satellites consistent within 0.05 %'. *Atmos. Measur. Tech.* 4, pp. 2007–2018. DOI: 10.5194/amt-4-2007-2011.

Frederick, J. E. (2002). 'Ozone as UV Filter'. In: *Encyclopedia of Atmospheric Sciences*. Ed. by J. R. Holton, J. Pyle, and J. Curry. Vol. 1. Academic Press, pp. 1621–1627. ISBN: 978-0-12-227090-1.

Free, M. and D. J. Seidel (2009). 'Observed El Niño–Southern Oscillation temperature signal in the stratosphere'. *J. Geophys. Res.* 114, D23108. DOI: 10.1029/2009JD012420.

Froidevaux, L., R. Fuller, M. Schwartz, J. Anderson, and R. Wang (2013). *README Document for the Global OZone Chemistry And Related trace gas Data records for the Stratosphere (GOZCARDS) project*. URL: gozcards.jpl.nasa.gov.

Gebhardt, C., A. Rozanov, R. Hommel, M. Weber, H. Bovensmann, J. P. Burrows, D. Degenstein, L. Froidevaux, and A. M. Thompson (2014). 'Stratospheric ozone trends and variability as seen by SCIAMACHY from 2002 to 2012'. *Atmos. Chem. Phys.* 14.2, pp. 831–846. DOI: 10.5194/acp-14-831-2014.

Gerber, E. P., A. Butler, N. Calvo, A. Charlton-Perez, M. Giorgetta, E. Manzini, J. Perlwitz, L. M. Polvani, F. Sassi, A. A. Scaife, T. A. Shaw, S.-W. Son, and S. Watanabe (2012). 'Assessing and Understanding the Impact of Stratospheric Dynamics and Variability on the Earth System'. *Bull. Amer. Meteor. Soc.* 93.6, pp. 845–859. DOI: 10.1175/BAMS-D-11-00145.1.

Gray, L. J., J. Beer, M. Geller, J. D. Haigh, M. Lockwood, K. Matthes, U. Cubasch, D. Fleitmann, G. Harrison, L. Hood, J. Luterbacher, G. A. Meehl, D. Shindell, B. van Geel, and W. White (2010). 'Solar influences on climate'. *Rev. Geophys.* 48.4. DOI: 10.1029/2009RG000282.

Haimberger, L., C. Tavolato, and S. Sperka (2008). 'Toward Elimination of the Warm Bias in Historic Radiosonde Temperature Records–Some New Results from a Comprehensive Intercomparison of Upper-Air Data'. *J. Climate* 23, pp. 4587–4606. DOI: 10.1175/2008JCLI1929.1.

– (2012). 'Homogenization of the Global Radiosonde Temperature Dataset through Combined Comparison with Reanalysis Background Series and Neighboring Sations'. *J. Climate* 25, pp. 8108–8131. DOI: 10.1175/JCLI-D-11-00668.1.

Hegglin, M. I. and T. G. Shepherd (2009). 'Large climate-induced changes in ultraviolet index and stratosphere-to-troposphere ozone flux'. *Nature* 2, pp. 687–691. DOI: 10.1038/ngeo604.

Hegglin, M. I., S. Tegtmeier, J. Anderson, L. Froidevaux, R. Fuller, B. Funke, A. Jones, G. Lingenfelser, J. Lumpe, D. Pendlebury, E. Remsberg, A. Rozanov, M. Toohey, J. Urban, T. von Clarmann, K. A. Walker, R. Wang, and K. Weigel (2013). 'SPARC Data Initiative: Comparison of water vapor climatologies from international satellite limb sounders'. *J. Geophys. Res.* 118.20, pp. 11,824–11,846. DOI: 10.1002/jgrd.50752.

Hitchcock, P., T. G. Shepherd, and C. McLandress (2009). 'Past and future conditions for polar stratospheric cloud formation simulated by the Canadian Middle Atmosphere Model'. *Atmos. Chem. Phys.* 9.2, pp. 483–495. DOI: 10.5194/acp-9-483-2009.

Holton, J. R and G. J Hakim (2013). *An Introduction to Dynamic Meteorology.* Vol. 5. Elsevier. ISBN: 978-0-12-384866-6.

IPCC (2013). *Climate Change 2013: The Physical Science Basis. Working Group I Contribution to the Fifth Assessment Report of the Intergovernmental Panel on Climate Change.* Ed. by T. F. Stocker, D. Qin, G.-K. Plattner, M. M. B. Tignor, S. K. Allen, J. Boschung, A. Nauels, Y. Xia, V. Bex, and P. M. Midgley. URL: http://www.ipcc.ch/.

Jacob, D. (1999). *An Introduction to Atmospheric Chemistry.* Vol. 1. Princeton University Press. URL: http://acmg.seas.harvard.edu/people/faculty/djj/book/.

Johnson, J. E., M. DeLand, and R. McPeters (2012). *README Document for the Creating a Long Term Multi-Sensor Ozone Data Record project.* URL: http://disc.sci.gsfc.nasa.gov/measures/documentation/documentation#McPeters.

Jones, A., J. Urban, D. P. Murtagh, P. Eriksson, S. Brohede, C. Haley, D. Degenstein, A. Bourassa, C. von Savigny, T. Sonkaew, A. Rozanov, H. Bovensmann, and J. Burrows (2009). 'Evolution of stratospheric ozone and water vapour time series studied with satellite measurements'. *Atmos. Chem. Phys.* 9.16, pp. 6055–6075. DOI: 10.5194/acp-9-6055-2009.

Kramarova, N. A., S. M. Frith, P. K. Bhartia, R. D. McPeters, S. L. Taylor, B. L. Fisher, G. J. Labow, and M. T. DeLand (2013). 'Validation of ozone monthly zonal mean profiles obtained from the version 8.6 Solar Backscatter Ultraviolet algorithm'. *Atmos. Chem. Phys.* 13.14, pp. 2549–2597. DOI: 10.5194/acp-13-6887-2013.

Kyrölä, E., J. Tamminen, G. Leppelmeier, V. Sofieva, S. Hassinen, J. Bertaux, A. Hauchecorne, F. Dalaudier, C. Cot, O. Korablev, O. F. d'Andon, G. Barrot, A. Mangin, B. Théodore, M. Guirlet, F. Etanchaud, P. Snoeij, R. Koopman, L. Saavedra, R. Fraisse, D. Fussen, and F. Vanhellemont (2004). 'GOMOS on Envisat: an overview'. *Adv. Space Res.* 33.7, pp. 1020–1028. DOI: 10.1016/S0273-1177(03)00590-8.

Kyrölä, E., M. Laine, V. Sofieva, J. Tamminen, S.-M. Päivärinta, S. Tukiainen, J. Zawodny, and L. Thomason (2013). 'Combined SAGE II–GOMOS ozone profile data set for 1984-2011 and trend analysis of the vertical distribution of ozone'. *Atmos. Chem. Phys.* 13.21, pp. 10645–10658. DOI: 10.5194/acp-13-10645-2013.

Ladstädter, F (2014). *Climatology Processing System 2.* Internal Report, Wegener Center for Climate and Global Change, University of Graz, Austria.

Ladstädter, F., A. K. Steiner, U. Foelsche, L. Haimberger, C. Tavolato, and G. Kirchengast (2011). 'An assessment of differences in lower stratospheric temperature records from (A)MSU, radiosondes, and GPS radio occultation'. *Atmos. Measur. Tech.* 4.9, pp. 1965–1977. DOI: 10.5194/amt-4-1965-2011.

Liu, C., G. Kirchengast, K. Zhang, R. Norman, Y. Li, S. Zhang, B. Carter, J. Fritzer, M. Schwaerz, S. Choy, S. Wu, and Z. Tan (2013). 'Characterisation of residual ionospheric errors in bending angles using GNSS RO end-to-end simulations'. *Adv. Space Res.* 52.5, pp. 821 –836. DOI: 10.1016/j.asr.2013.05.021.

Llewellyn, E., N. Lloyd, D. Degenstein, R. Gattinger, S. Petelina, A. Bourassa, J. Wiensz, E. Ivanov, I. McDade, B. Solheim, J. McConnell, C. Haley, C. von Savigny, C. Sioris, C. McLinden, E. Griffioen, J. Kaminski, W. Evans, E. Puckrin, and K. Strong (2004). 'The OSIRIS instrument on the Odin spacecraft'. *Canadian J. Phys.* 82.6, pp. 411–422. DOI: 10.1139/P04-005.

Manney, G. L., M. L. Santee, M. Rex, N. J. Livesey, M. C. Pitts, P. Veefkind, E. R. Nash, I. Wohltmann, R. Lehmann, L. Froidevaux, L. R. Poole, M. R. Schoeberl, D. P. Haffner, J. Davies, V. Dorokhov, H. Gernandt, B. Johnson, R. Kivi, E. Kyrö, and N. Larsen (2011). 'Unprecedented Arctic ozone loss in 2011'. *Nature* 478.7370, pp. 469 –475. DOI: 10.1038/nature10556.

Matsumi, Y. and M. Kawasaki (2003). 'Photolysis of Atmospheric Ozone in the Ultraviolet Region'. *Chem. Rev.* 103.12, pp. 4767–4782. DOI: 10.1021/cr0205255.

McLandress, C., A. I. Jonsson, D. A. Plummer, M. C. Reader, J. F. Scinocca, and T. G. Shepherd (2010). 'Separating the Dynamical Effects of Climate Change and Ozone Depletion. Part I: Southern Hemisphere Stratosphere'. *J. Climate* 23. DOI: 10.1175/2010JCLI3586.1.

McPeters, R. D. and G. J. Labow (2012). 'Climatology 2011: An MLS and sonde derived ozone climatology for satellite retrieval algorithms'. *J. Geophys. Res.* 117.D10. DOI: 10.1029/2011JD017006.

McPeters, R. D., G. J. Labow, and J. A. Logan (2007). 'Ozone climatological profiles for satellite retrieval algorithms'. *J. Geophys. Res.* 112.D5. DOI: 10.1029/2005JD006823.

Mohanakumar, K. (2008). *Stratosphere Troposphere Interactions*. Springer Science. ISBN: 978-1-4020-8216-0.

Molina, M. J. and F. S. Rowland (1974). 'Stratospheric sink for chlorofluromethanes: chlorine atomc-atalysed destruction of ozone'. *Nature* 249, pp. 810–812. DOI: 10.1038/249810a0.

Mote, P. W., K. H. Rosenlof, M. E. McIntyre, E. S. Carr, J. C. Gille, J. R. Holton, J. S. Kinnersley, H. C. Pumphrey, J. M. Russell, and J. W. Waters (1996). 'An atmospheric tape recorder: The imprint of tropical tropopause temperatures on stratospheric water vapor'. *J. Geophys. Res.* 101.D2, pp. 3989–4006. DOI: 10.1029/95JD03422.

Newman, P. A., L. D. Oman, A. R. Douglass, E. L. Fleming, S. M. Frith, M. M. Hurwitz, S. R. Kawa, C. H. Jackman, N. A. Krotkov, E. R. Nash, J. E. Nielsen, S. Pawson, R. S. Stolarski, and G. J. M. Velders (2009). 'What would have happened to the ozone layer if chlorofluorocarbons (CFCs) had not been regulated?' *Atmos. Chem. Phys.* 9.6, pp. 2113–2128. DOI: 10.5194/acp-9-2113-2009.

Poli, P., S. B. Healy, and D. P. Dee (2010). 'Assimilation of Global Positioning System radio occultation data in the ECMWF ERA–Interim reanalysis'. *Quart. J. Roy. Meteor. Soc.* 136.653, pp. 1972–1990. DOI: 10.1002/qj.722.

Polvani, L. M and S. Solomon (2012). 'The Signature of ozone depletion on tropical temperature trends, as revealed by their seasonal cycle in model integrations with single forcings'. *J. Geophys. Res.* 117. DOI: 10.1029/2012JD017719.

Qu, J. J., W. Gao, M. Kafatos, R. E. Murphy, and V. V. Salomonson (2006). *Earth Science Satellite Remote Sensing - Science and Instruments.* Vol. 1. Springer. ISBN: 978-3-540-35606-6.

Ramaswamy, V., M.-L. Chanin, J. Angell, J. Barnett, D. Gaffen, M. Gelman, P. Keckhut, Y. Koshelkov, K. Labitzke, J.-J. R. Lin, A. O'Neill, J. Nash, W. Randel, R. Rood, K. Shine, M. Shiotani, and R. Swinbank (2001). 'Stratospheric temperature trends: Observations and model simulations'. *Rev. Geophys.* 39.1, pp. 71–122. DOI: 10.1029/1999RG000065.

Randel, W. J., F. Wu, R. Swinbank, J. Nash, and A. O'Neill (1999). 'Global QBO Circulation Derived from UKMO Stratospheric Analyses'. *J. Atmos. Sci.* 56, pp. 457–474. DOI: 10.1175/1520-0469(1999)056<0457:GQCDFU>2.0.CO;2.

Randel, W. J. and A. M. Thompson (2011). 'Interannual variability and trends in tropical ozone derived from SAGE II satellite data and SHADOZ ozonesondes'. *J. Geophys. Res.* 116.D7. ISSN: 2156-2202. DOI: 10.1029/2010JD015195.

Randel, W. J., F. Wu, S. J. Oltmans, K. Rosenlof, and G. E. Nedoluha (2004). 'Interannual Changes of Stratospheric Water Vapor and Correlations with Tropical Tropopause Temperatures'. *J. Atmos. Sci.* 61, pp. 2133–2148. DOI: 10.1175/1520-0469(2004)061<2133:ICOSWV>2.0.CO;2.

Randel, W. J., R. R. Garcia, N. Calvo, and D. Marsh (2009). 'ENSO influence on zonal mean temperature and ozone in the tropical lower stratosphere'. *Geophys. Res. Lett.* 36.15. DOI: 10.1029/2009GL039343.

Reid, G. C., K. S. Gage, and J. R. McAfee (1989). 'The thermal response of the tropical atmosphere to variations in equatorial Pacific sea surface temperature'. *J. Geophys. Res.* 94.D12, pp. 14705–14716. DOI: 10.1029/JD094iD12p14705.

Rex, M., R. J. Ralawitch, P. von der Gathen, N. R. P. Harris, M. P. Chipperfield, and B. Naujokat (2004). 'Arctic ozone loss and climate change'. *Geophys. Res. Lett.* 31. DOI: 10.1029/2003GL018844.

Rieckh, T. (2013). 'Tropopause Characteristics from GPS Radio Occultation Data'. Diploma thesis. University of Graz. URL: http://wegcenter.uni-graz.at/de/wegener-center-verlag/2013/.

Rieder, H. E. and L. M. Polvani (2013). 'Are recent Arctic ozone losses caused by increasing greenhouse gases?' *Geophys. Res. Lett.* 40, pp. 1–5. DOI: 10.1002/grl.50835.

Rosing, M. T., D. K. Bird, N. H. Sleep, and C. J. Bjerrum (2010). 'No climate paradox under the faint early Sun'. *Science* 464, pp. 744–747. DOI: 10.1038/nature08955.

Santer, B. D., T. M. L. Wigley, J. S. Boyle, D. J. Gaffen, J. J. Hnilo, D. Nychka, D. E. Parker, and K. E. Taylor (2000). 'Statistical significance of trends and trend differences in layer-average atmospheric temperature time series'. *J. Geophys. Res.* 106.D6, pp. 7337–7356. DOI: 10.1029/1999JD901105.

Scherllin-Pirscher, B., A. K. Steiner, G. Kirchengast, Y.-H. Kuo, and U. Foelsche (2011a). 'Empirical analysis and modeling of errors of atmospheric profiles from GPS radio occultation'. *Atmos. Measur. Tech.* 4, pp. 1875–1890. DOI: 10.5194/amt-4-1875-2011.

Scherllin-Pirscher, B., G. Kirchengast, A. K. Steiner, Y.-H. Kuo, and U. Foelsche (2011b). 'Quantifying uncertainty in climatological fields from GPS radio occultation: an empirical-analytical error model'. *Atmos. Measur. Tech.* 4, pp. 2019–2034. DOI: 10.5194/amt-4-2019-2011.

Schwartz, S. E. and P. Warneck (1995). 'Units for use in atmospheric chemistry'. *Pure & Appl. Chem.* 67, pp. 1377–1408. URL: http://www.iupac.org/publications/pac/1995/pdf/6708x1377.pdf.
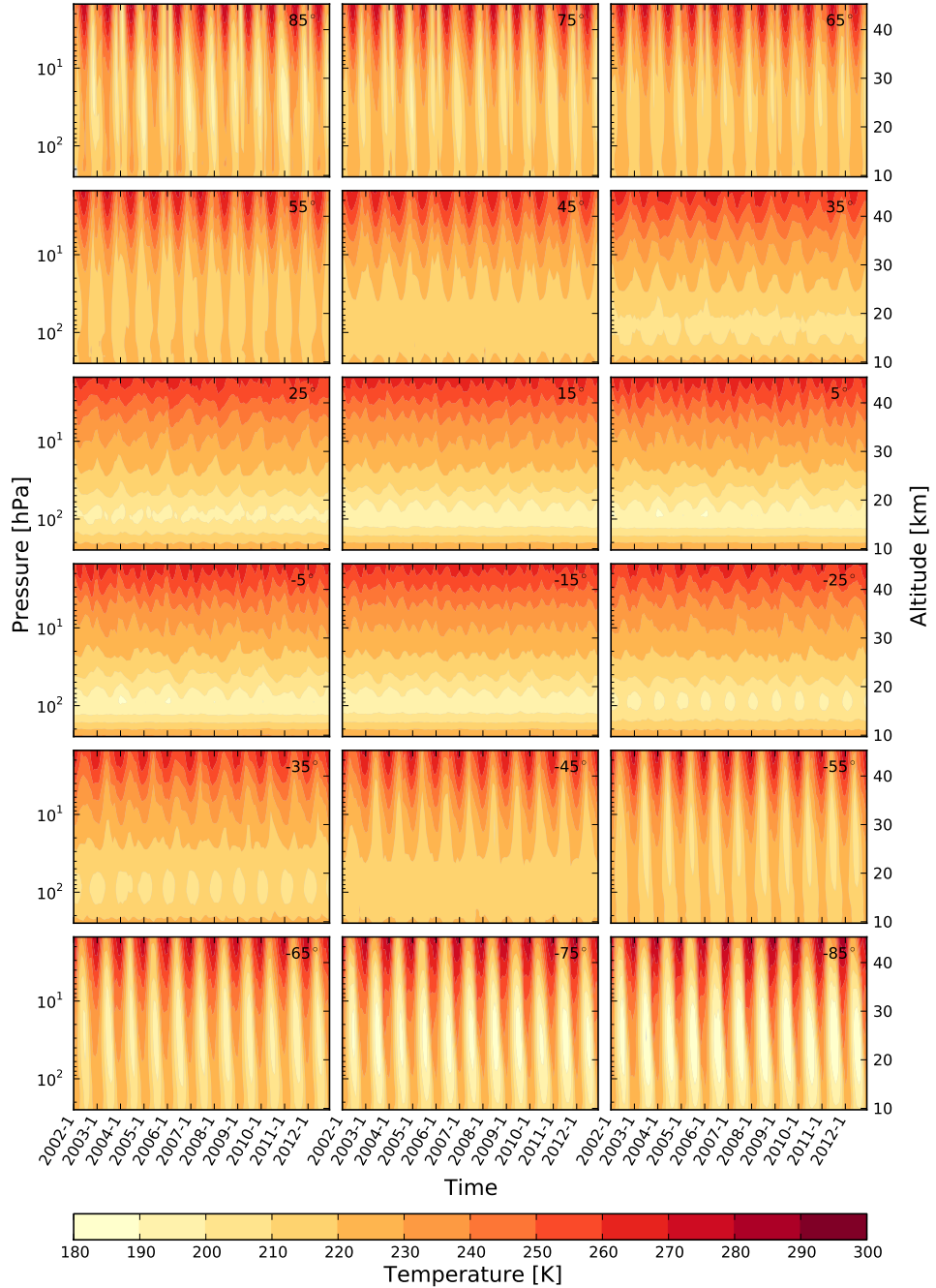
Schwärz, M., B. Scherllin-Pirscher, G. Kirchengast, J. Schwarz, F. Ladstädter, J. Fritzer, and J. Ramsauer (2013). *Multi-Mission Validation by Satellite Radio Occulation.*

Seidel, D. J. and W. J. Randel (2006). 'Variability and trends in the global tropopause estimated from radiosonde data'. *J. Geophys. Res.* 11. DOI: 10.1029/2006JD007363.

Seidel, D. J., N. P. Gillett, J. R. Lanzante, K. P. Shine, and P. W. Thorne (2011). 'Stratospheric temperature trends: our evolving understanding'. *Wiley Interdisciplinary Reviews: Climate Change* 2.4, pp. 592–616. DOI: 10.1002/wcc.125.

Simmons, A. J., P. Poli, D. P. Dee, P. Berrisford, H. Hersbach, S. Kobayashi, and C. Peubey (2014). 'Estimating low-frequency variability and trends in atmospheric temperature using ERA-Interim'. *Quart. J. Roy. Meteor. Soc.* 140.679, pp. 329–353. DOI: 10.1002/qj.2317.

Simmons, A., S. Uppala, D. Dee, and S. Kobayashi (2007). 'ERA-Interim: New ECMWF reanalysis products from 1989 onwards'. *ECMWF Newsletter* 110. URL: http://www.ecmwf.int/publications/newsletters/archive_chronological_list.htm.

Sofieva, V. F., N. Rahpoe, J. Tamminen, E. Kyrölä, N. Kalakoski, M. Weber, A. Rozanov, C. von Savigny, A. Laeng, T. von Clarmann, G. Stiller, S. Lossow, D. Degenstein, A. Bourassa, C. Adams, C. Roth, N. Lloyd, P. Bernath, R. J. Hargreaves, J. Urban, D. Murtagh, A. Hauchecorne, F. Dalaudier, M. van Roozendael, N. Kalb, and C. Zehner (2013). 'Harmonized dataset of ozone profiles from satellite limb and occultation measurements'. *Earth Sys. Sci. Data* 5.2, pp. 349–363. DOI: 10.5194/essd-5-349-2013.

Steinbrecht, W., H. Claude, F. Schönenborn, I. S. McDermid, T. Leblanc, S. Godin, T. Song, D. P. J. Swart, Y. J. Meijer, G. E. Bodeker, B. J. Connor, N. Kämpfer, K. Hocke, Y. Calisesi, N. Schneider, J. de la Noë, A. D. Parrish, I. S. Boyd, C. Brühl, B. Steil, M. A. Giorgetta, E. Manzini, L. W. Thomason, J. M. Zawodny, M. P. McCormick, J. M. Russell, P. K. Bhartia, R. S. Stolarski, and S. M. Hollandsworth-Frith (2006). 'Long-term evolution of upper stratospheric ozone at selected stations of the Network for the Detection of Stratospheric Change (NDSC)'. *J. Geophys. Res.* 111.D10. DOI: 10.1029/2005JD006454.

Steiner, A. K., D. Hunt, S.-P. Ho, G. Kirchengast, A. J. Mannucci, B. Scherllin-Pirscher, H. Gleisner, A. von Engeln, T. Schmidt, C. Ao, S. S. Leroy, E. R. Kursinski, U. Foelsche, M. Gorbunov, S. Heise, Y.-H. Kuo, K. B. Lauritsen, C. Marquardt, C. Rocken, W. Schreiner, S. Sokolovskiy, S. Syndergaard, and J. Wickert (2013a). 'Quantification of structural uncertainty in climate data records from GPS radio
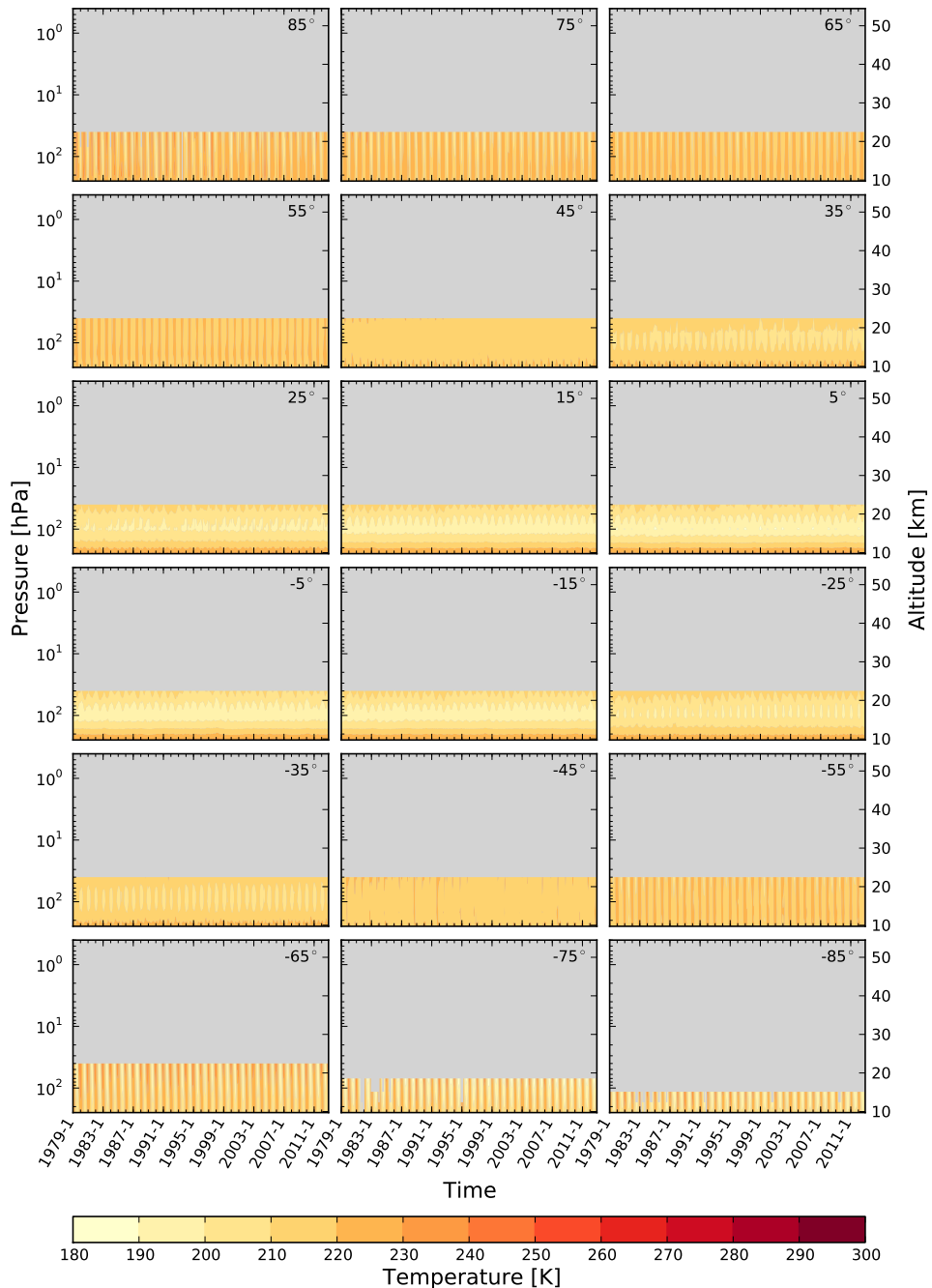
occultation'. *Atmos. Chem. Phys.* 13.3, pp. 1469–1484. DOI: 10.5194/acp-13-1469-2013.

Steiner, A. K., B. Scherllin-Pirscher, L. Brunner, M. Schwärz, and G. Kirchengast (2013b). *Temperature trends in the upper troposphere to lower stratosphere from radio occultation climate records 2002 to 2012*. Poster, AGU Fall Meeting.

Tegtmeier, S., M. I. Hegglin, J. Anderson, A. Bourassa, S. Brohede, D. Degenstein, L. Froidevaux, R. Fuller, B. Funke, J. Gille, A. Jones, Y. Kasai, K. Krüger, E. Kyrölä, G. Lingenfelser, J. Lumpe, B. Nardi, J. Neu, D. Pendlebury, E. Remsberg, A. Rozanov, L. Smith, M. Toohey, J. Urban, T. von Clarmann, K. A. Walker, and R. H. J. Wang (2013). 'SPARC Data Initiative: A comparison of ozone climatologies from international satellite limb sounders'. *J. Geophys. Res.* DOI: 10.1002/2013JD019877.

UN (1998). *Kyoto Protocol to the United Nations Framework Convention on Climate Change*. URL: http://unfccc.int/resource/docs/convkp/kpeng.pdf.

– (2012). *Doha amendment to the Kyoto Protocol*. URL: http://unfccc.int/files/kyoto_protocol/application/pdf/kp_doha_amendment_english.pdf.

WMO (1957). *Meteorology – A three dimensional science*. WMO Bull. 6. Geneva: World Meteorological Organization (WMO).

WMO (2011). *Scientific Assessment of Ozone Depletion: 2010, Global Ozone Research and Monitoring Project–Report No. 52*. ISBN: 9966-7319-6-2. URL: http://www.wmo.int/pages/prog/arep/gaw/ozone/.

WMO (2013). *Antarctic Ozone Bulletin: 6/2013*. URL: http://www.wmo.int/pages/prog/arep/WMOAntarcticOzoneBulletins2013.html.

Wallace, J. M. and P. V. Hobbs (2006). *Atmospheric Science. An Introductory Survey*. 2nd ed. ISBN: 0-12-732951-X.

Weinhold, B. (2008). 'Ozone Nation: EPA Standard Panned by the People'. *Environmental Health Perspectives*. URL: www.ncbi.nlm.nih.gov/pmc/articles/PMC2453178/.

Wilks, D. S. (2006). *Statistical methods in the atmospheric sciencs*. 2nd ed. Elsevier. ISBN: 978-0-12-751966-1.

A. Data set coverage and annual cycles
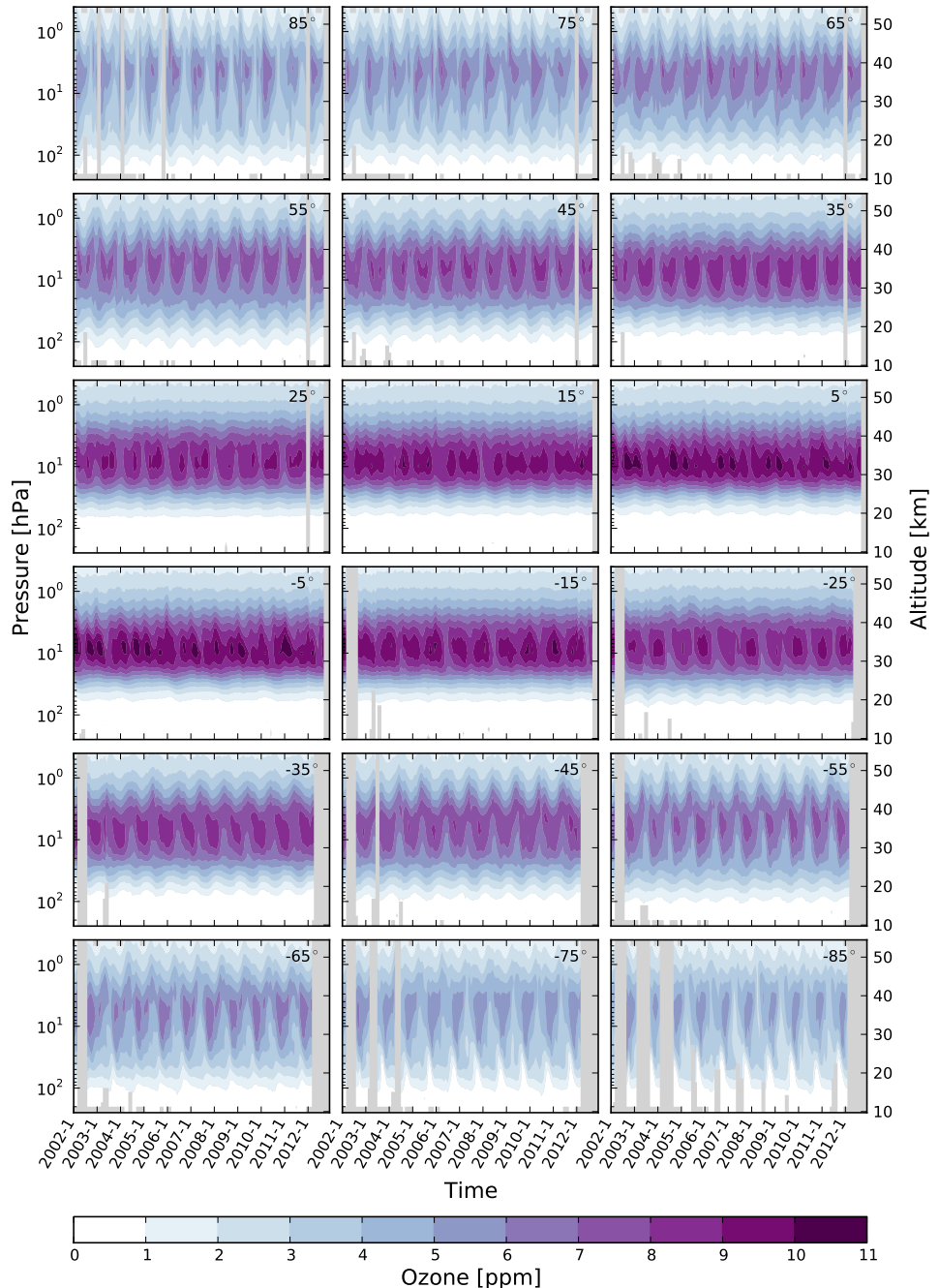
Figure A.1.: RO temperature time series for the period 2002 to 2012 based on the WEGC Occultation Processing System version 5.6 (OPSv5.6) data set. The center of the latitude band is given in the top right corner of each subplot, negative values correspond to the southern hemisphere.
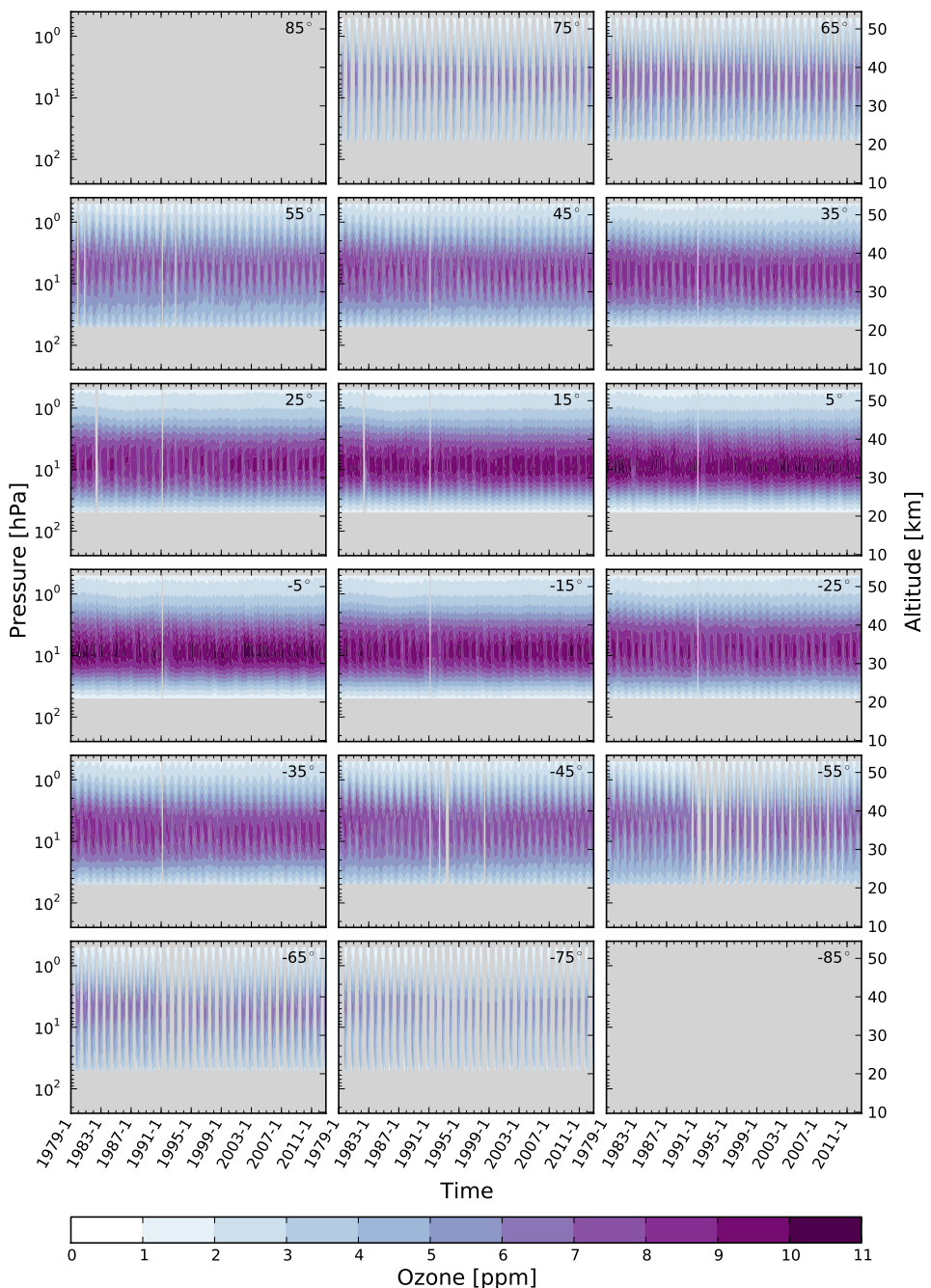
Figure A.2.: Radiosonde Innovation Composite Homogenization (RICH) RS temperature time series from 1979 to 2012. Same layout as Fig. A.1.

A. Data set coverage and annual cycles
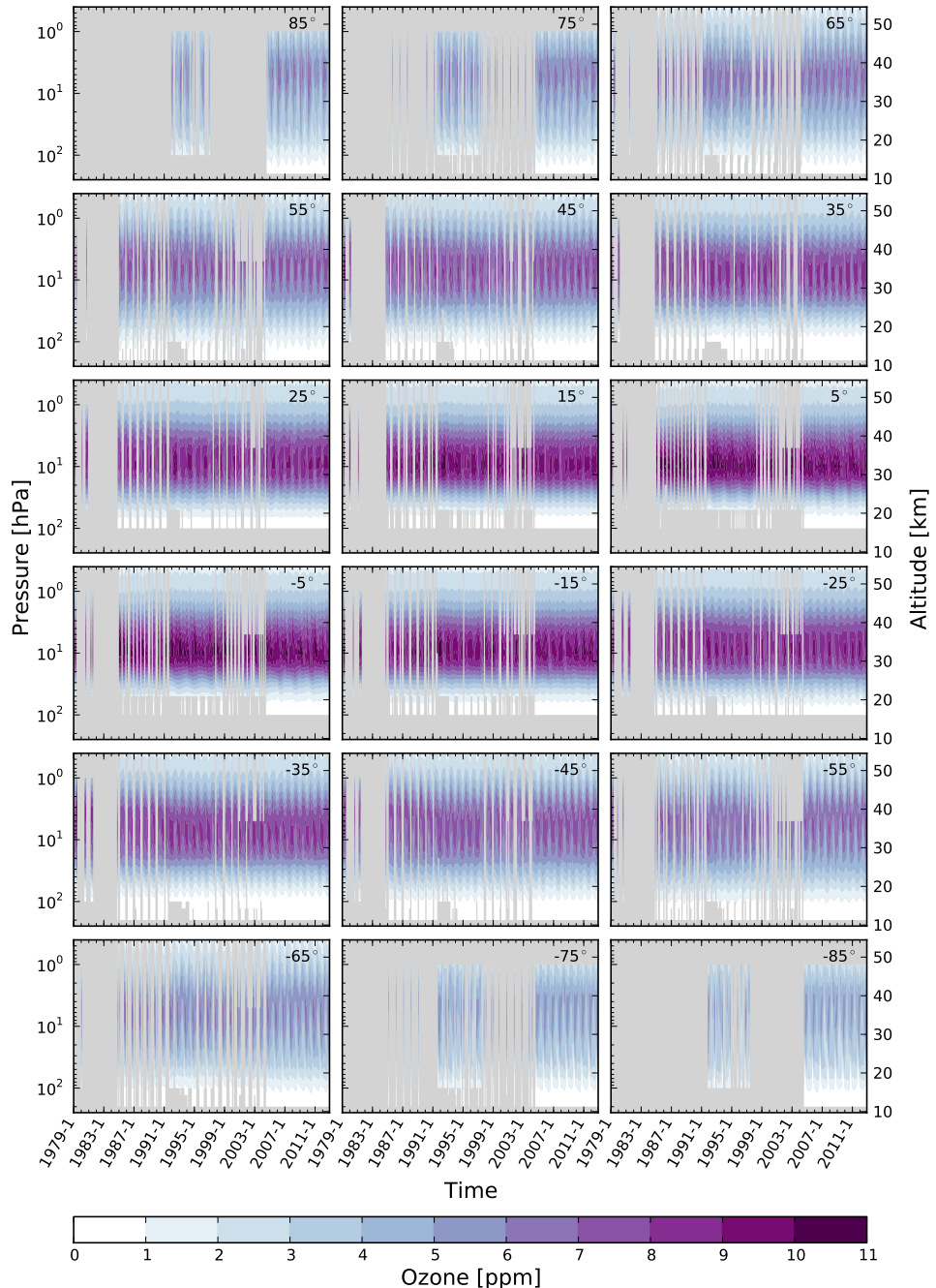
Figure A.3.: HARMOZ ozone time series from 2002 to 2012. Same layout as Fig. A.1.
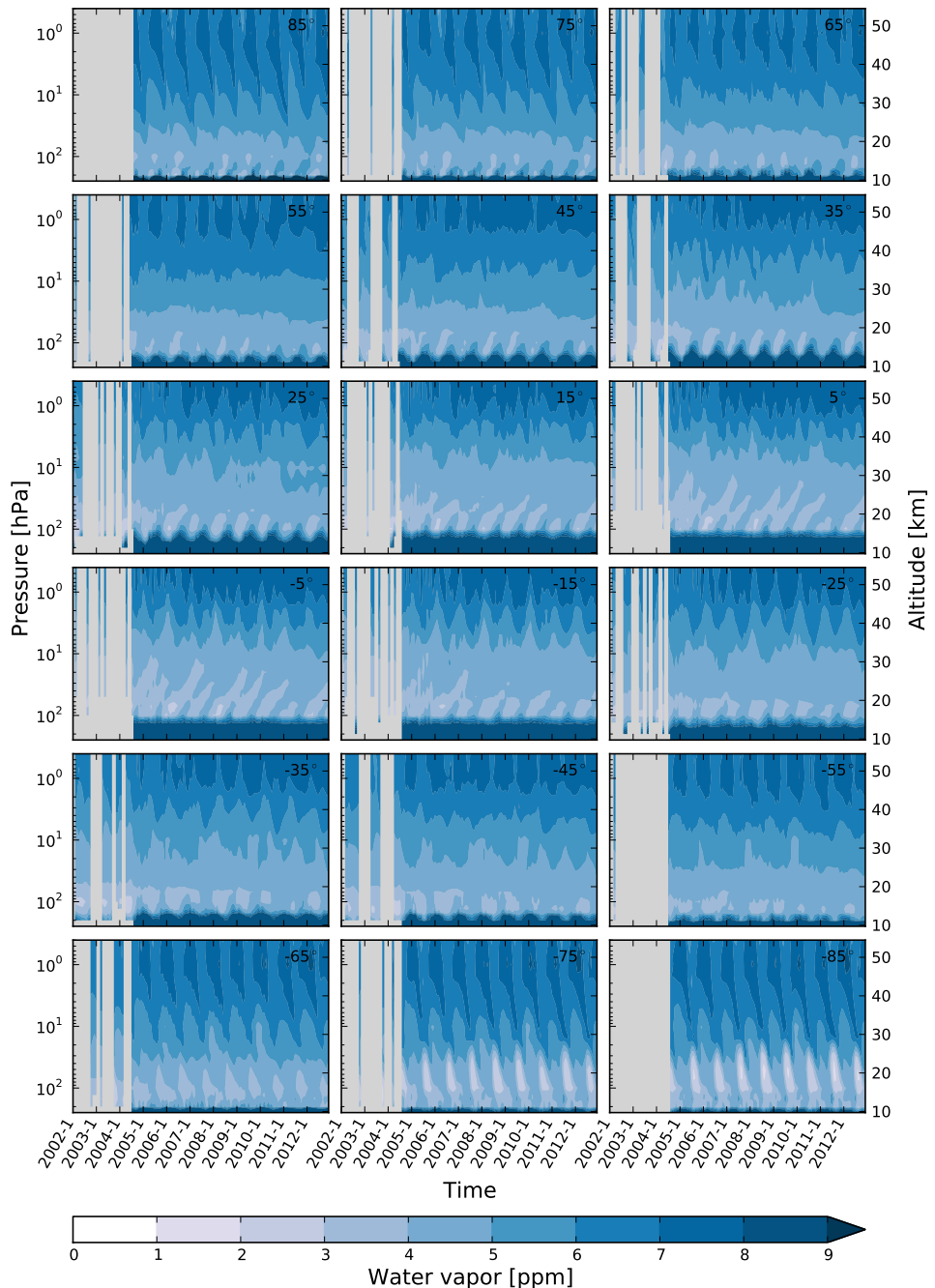
Figure A.4.: NOAA SBUV ozone time series from 1979 to 2012. Same layout as Fig. A.1.
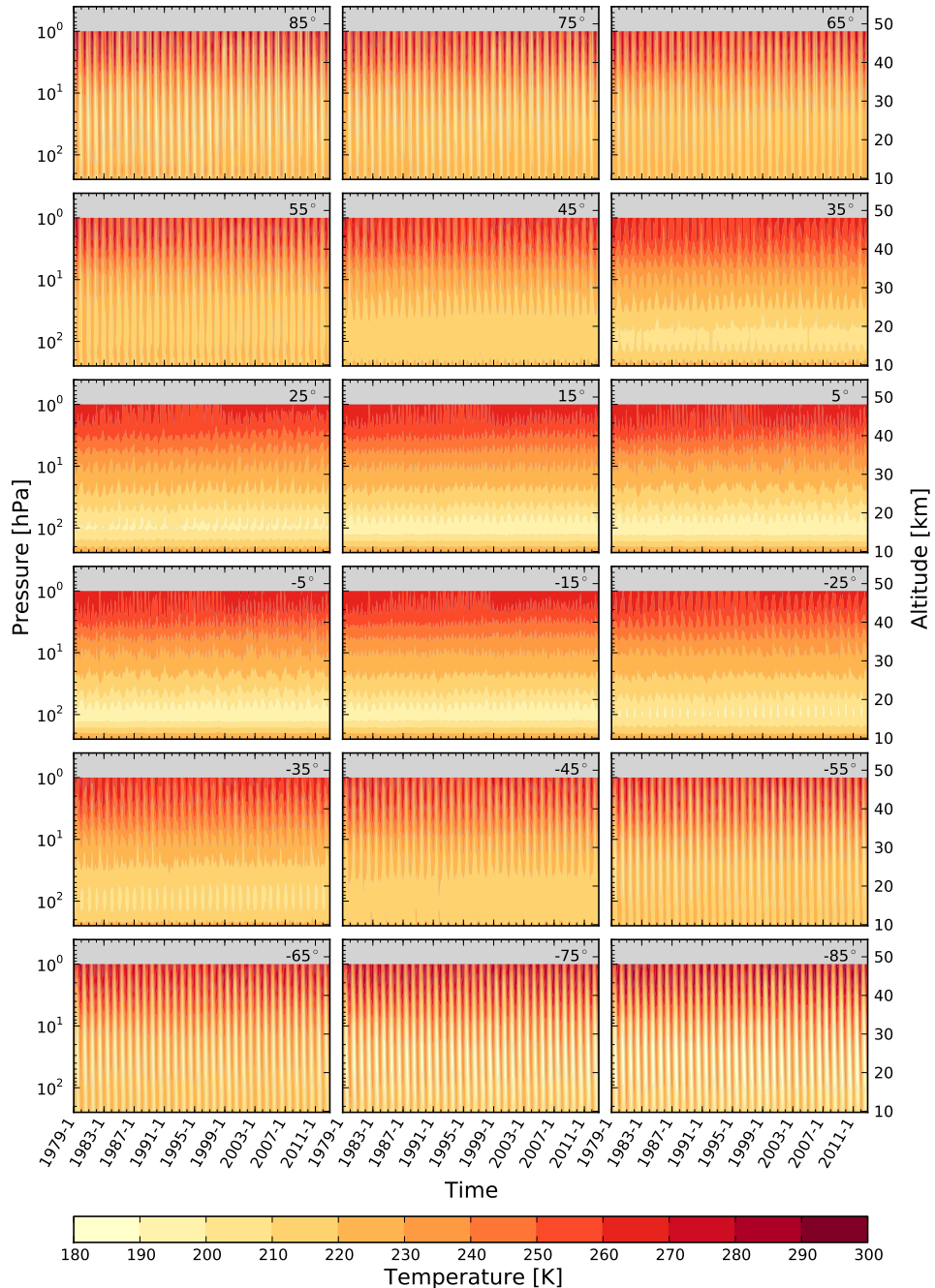
Figure A.5.: GOZCARDS ozone time series from 1979 to 2012. Same layout as Fig. A.1.
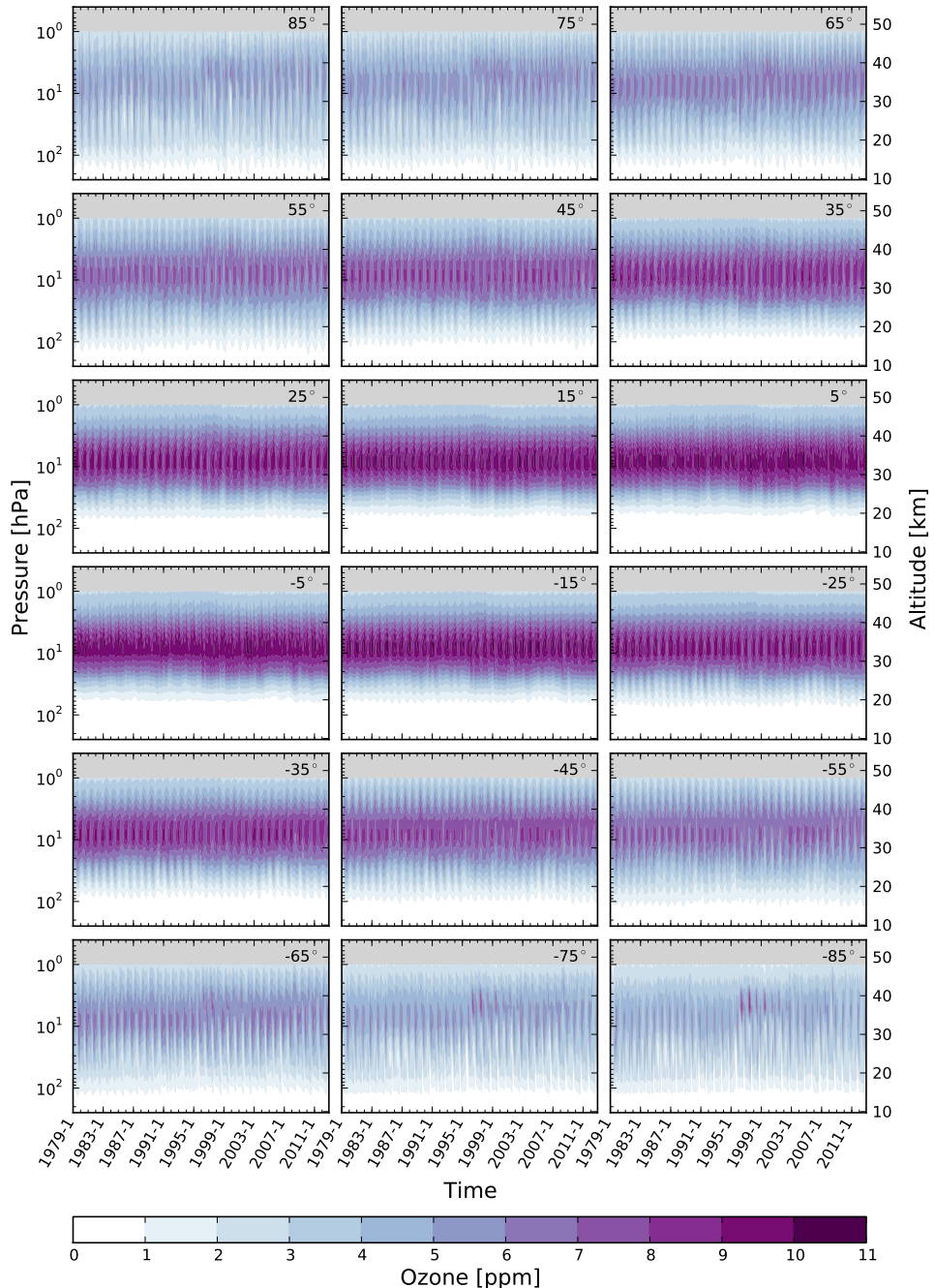
Figure A.6.: GOZCARDS water vapor time series from 2002 to 2012. Same layout as Fig. A.1.
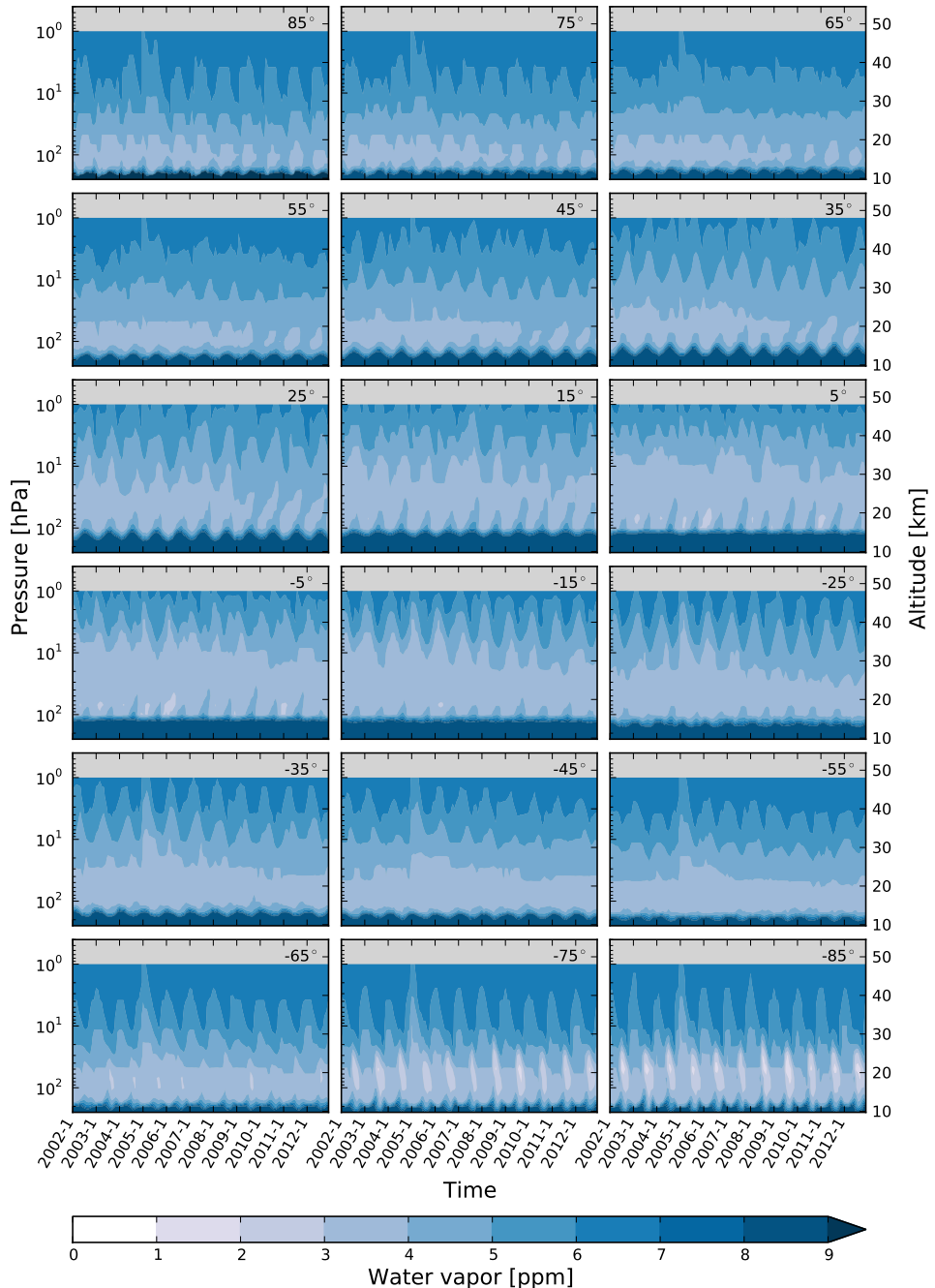
Figure A.7.: ERA-Interim temperature time series from 1979 to 2012. Same layout as Fig. A.1.
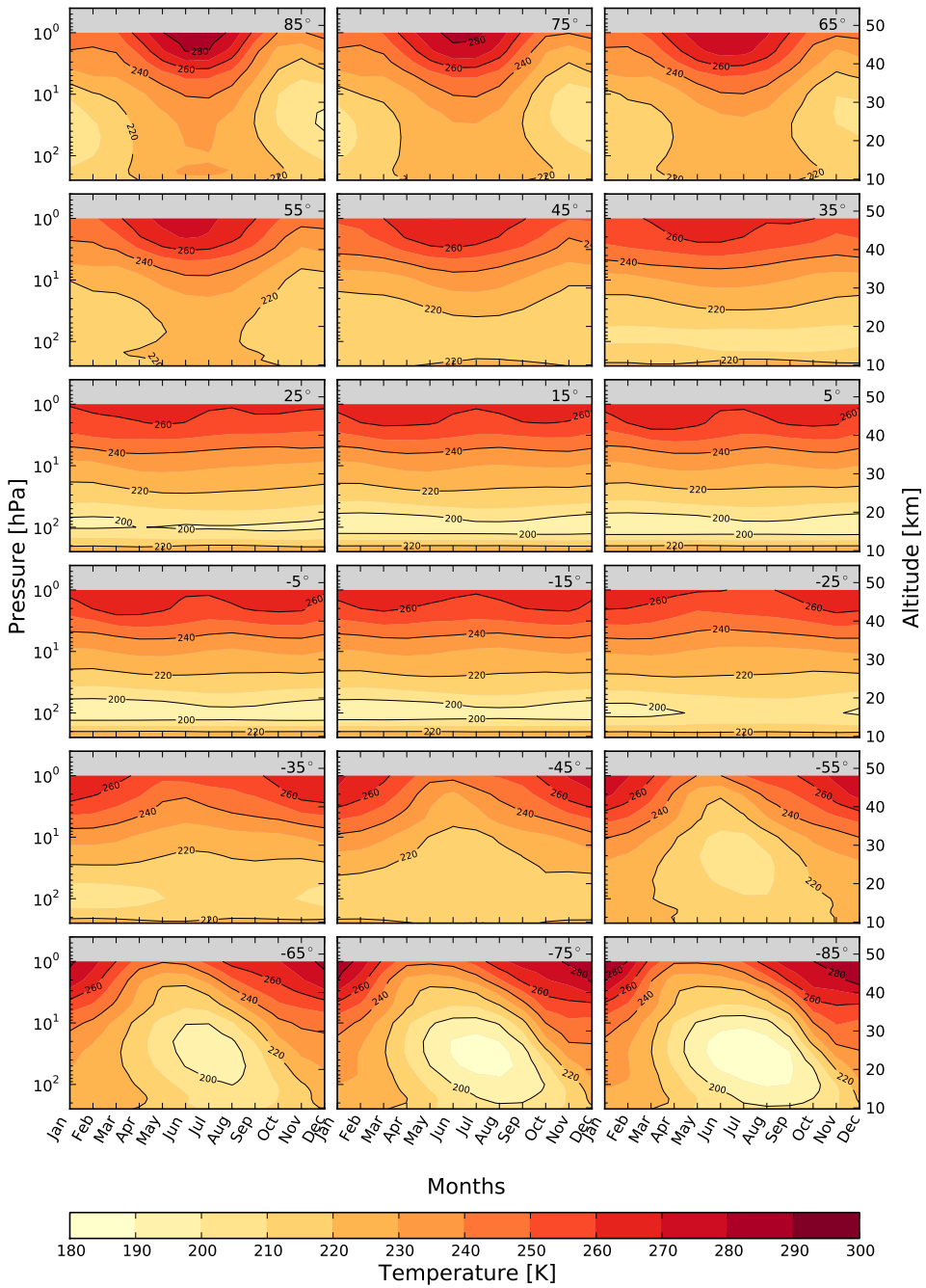
Figure A.8.: ERA-Interim ozone time series from 1979 to 2012. Same layout as Fig. A.1.

Figure A.9.: ERA-Interim water vapor time series from 2002 to 2012. Same layout as Fig. A.1.

Figure A.10.: Mean annual cycle averaged over 1979 to 2012 of ERA-Interim temperature. The center of the latitude band is given in the top right corner of each subplot, negative values correspond to the southern hemisphere.
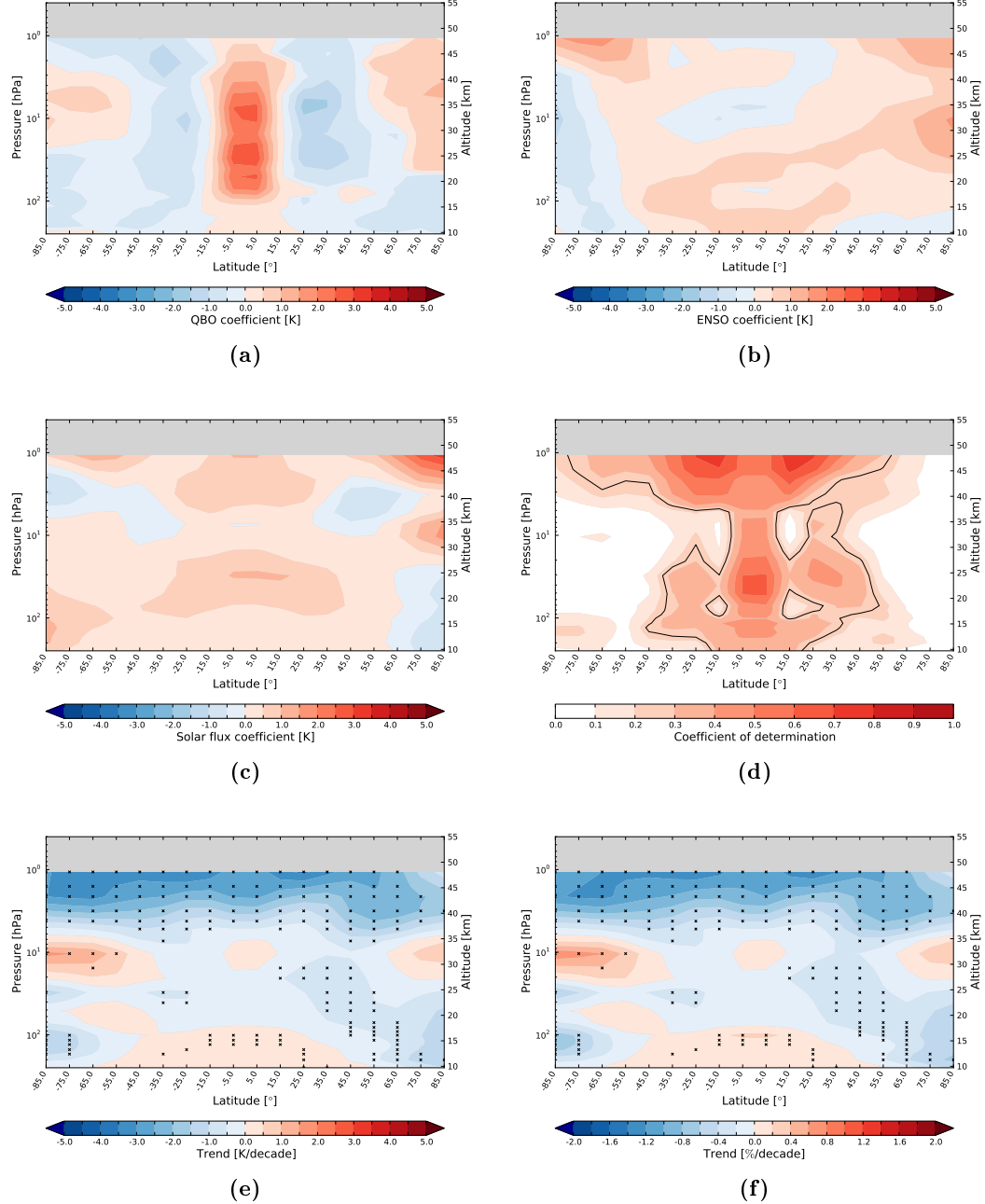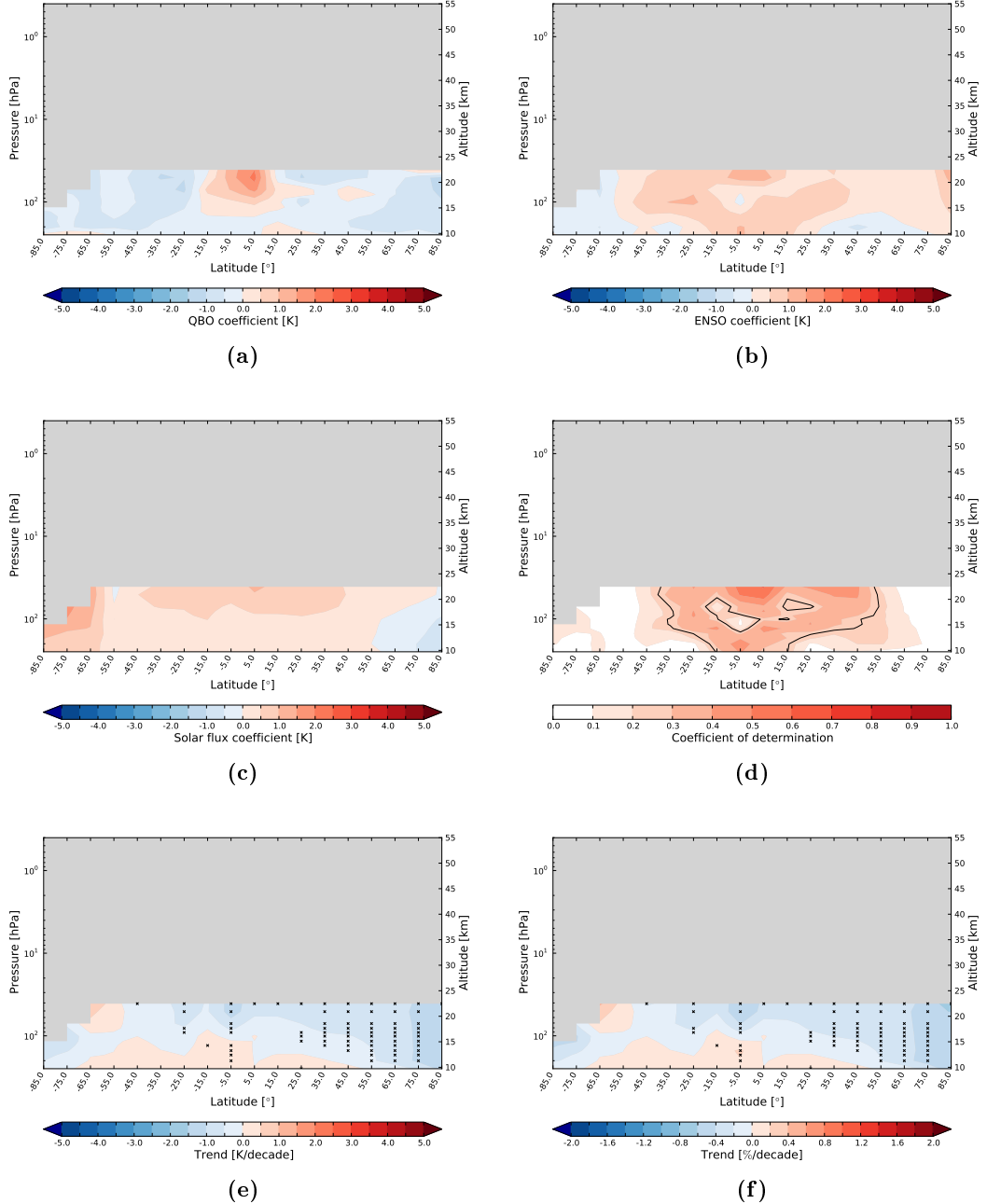
Figure A.11.: Mean annual cycle averaged over 1979 to 2012 of GOZCARDS ozone. Same layot as Fig. A.10

B. Ozone depletion period (1979 to 1996)
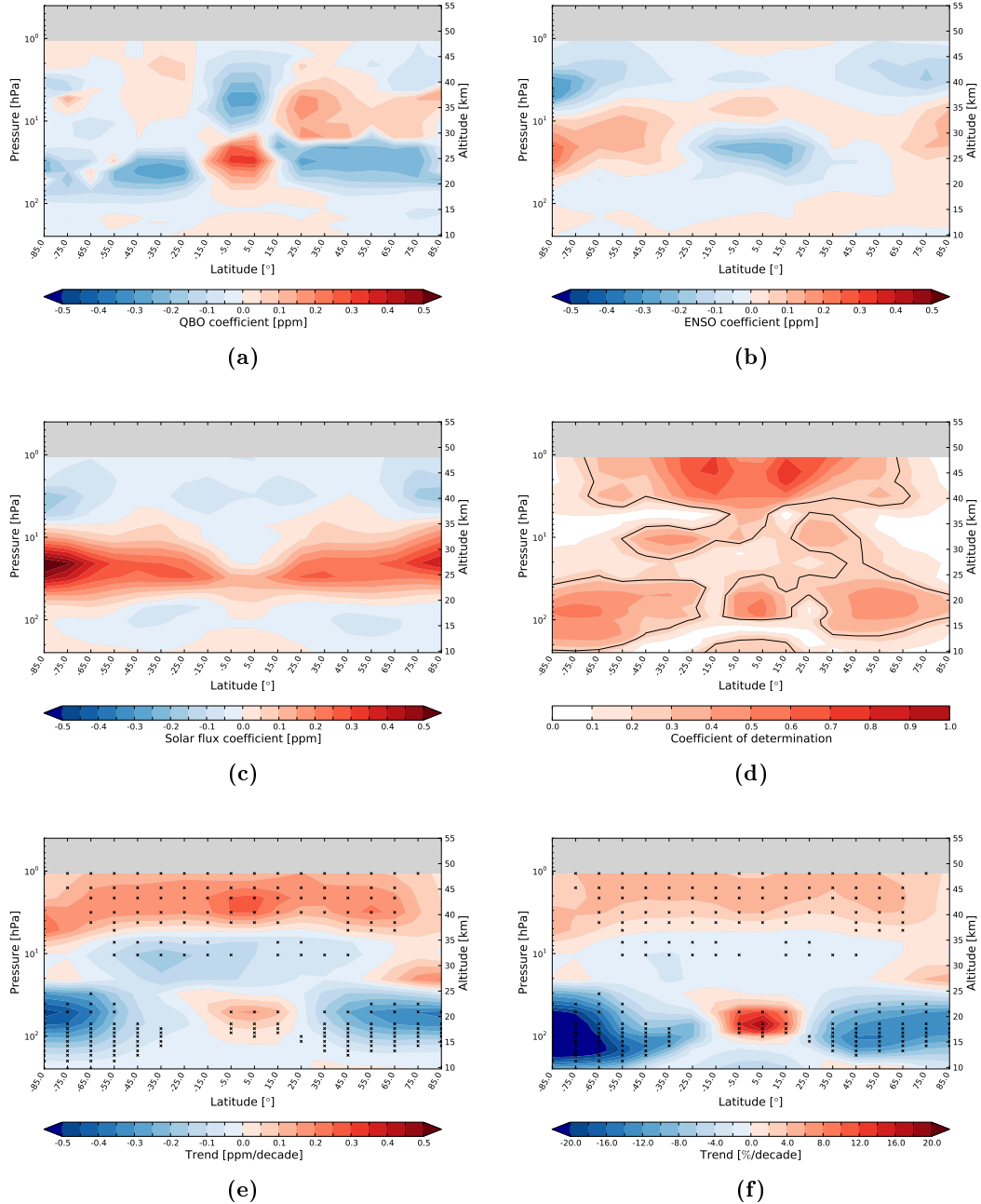
Figure B.1.: Results of the regression analysis for the ERA-Interim temperature data set in the depletion period 1979 to 1996. QBO (a), ENSO (b), and solar flux (c) coefficients as well as coefficient of determination (d). The solid line in (d) marks a determination value of 0.25. Absolute (e) and relative (f) trend, the × sign denotes regions significant on the 95 % level.
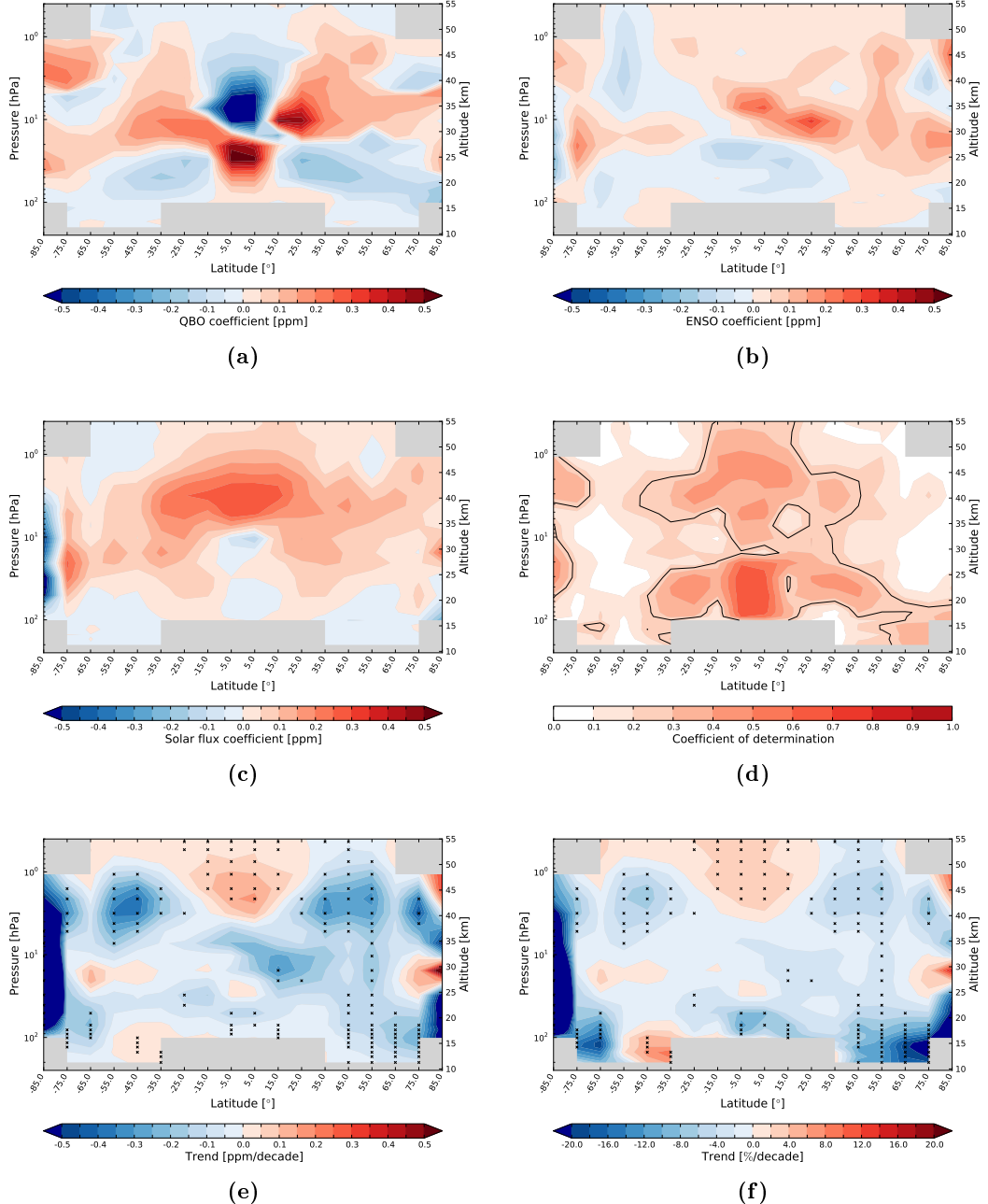
Figure B.2.: Results of the regression analysis for the RICH RS temperature data set in the depletion period 1979 to 2012. Same layout as Fig. B.1.

(a)

(b)

(c)

(d)

(e)

(f)
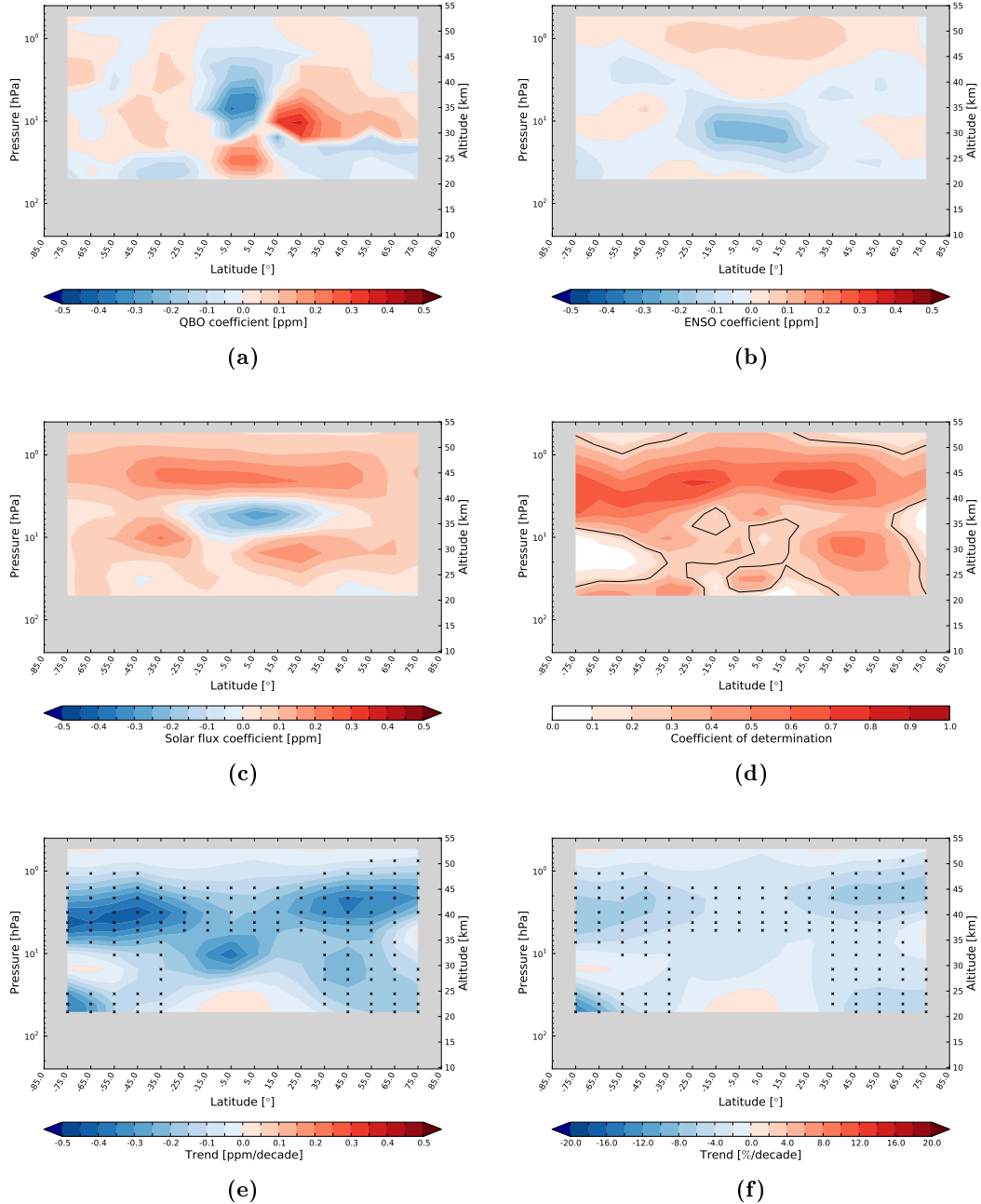
Figure B.3.: Results of the regression analysis for the ERA-Interim ozone data set in the depletion period 1979 to 2012. Same layout as Fig. B.1.

Figure B.4.: Results of the regression analysis for the GOZCARDS ozone data set in the depletion period 1985 to 2012. Same layout as Fig. B.1.

(a)

(b)

(c)

(d)

(e)

(f)
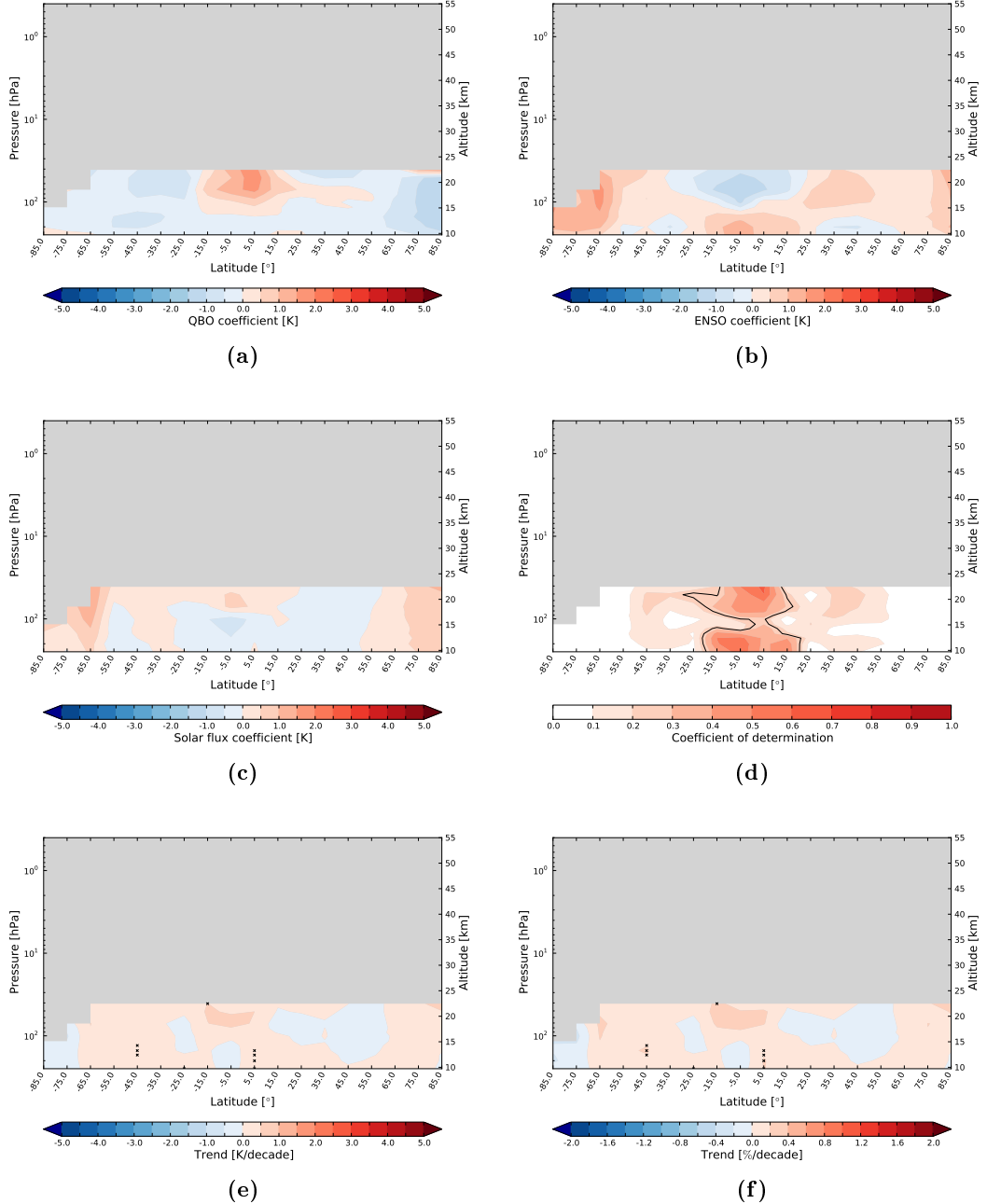
Figure B.5.: Results of the regression analysis for the NOAA SBUV ozone data set in the depletion period 1979 to 2012. Same layout as Fig. B.1.

C. Ozone recovery period (1997 to 2012)
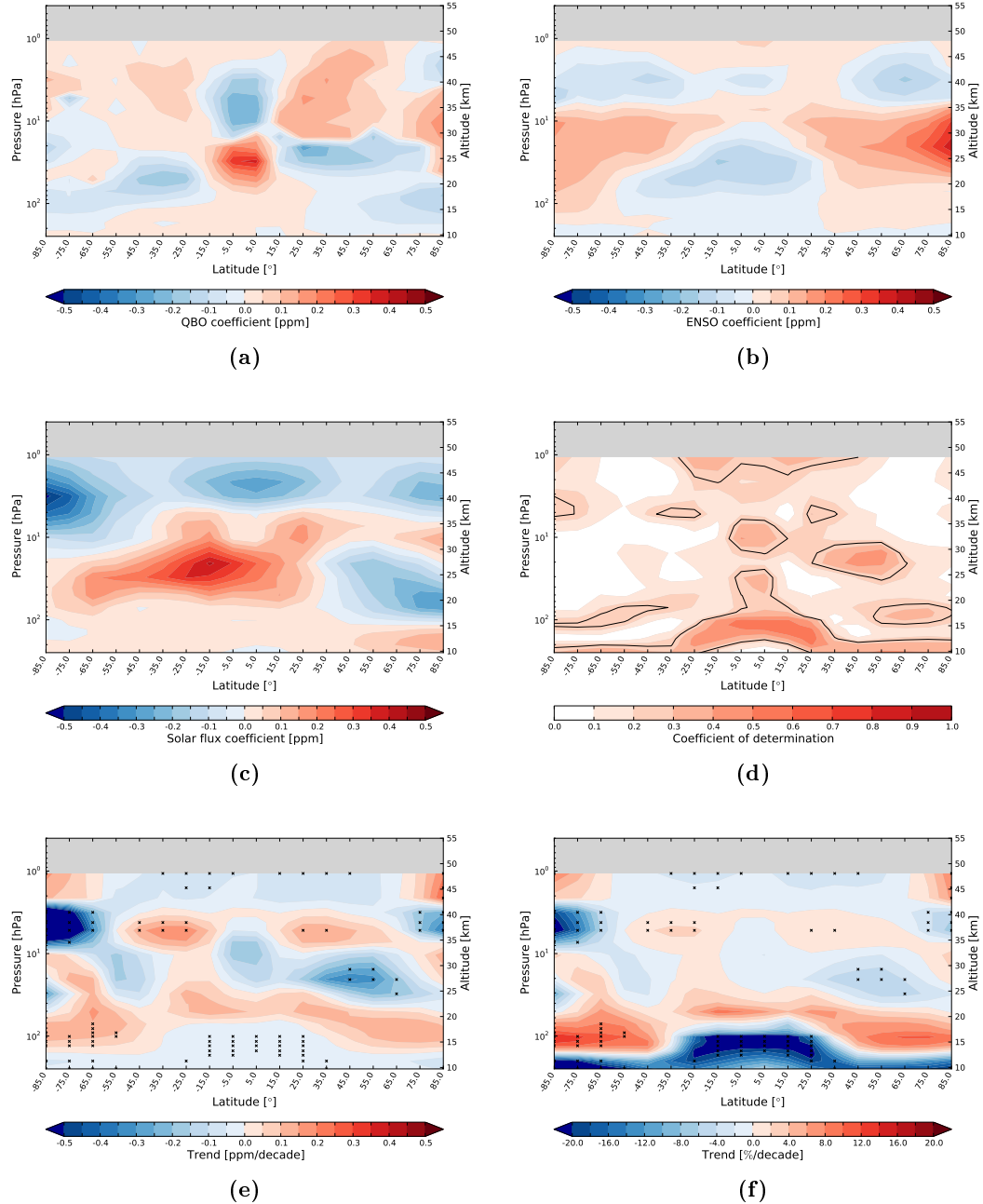
Figure C.1.: Results of the regression analysis for the ERA-Interim temperature data set in the recovery period 1997 to 2012. QBO (a), ENSO (b), and solar flux (c) coefficients as well as coefficient of determination (d). The solid line in (d) marks a determination value of 0.25. Absolute (e) and relative (f) trend, the × sign denotes regions significant on the 95 % level.
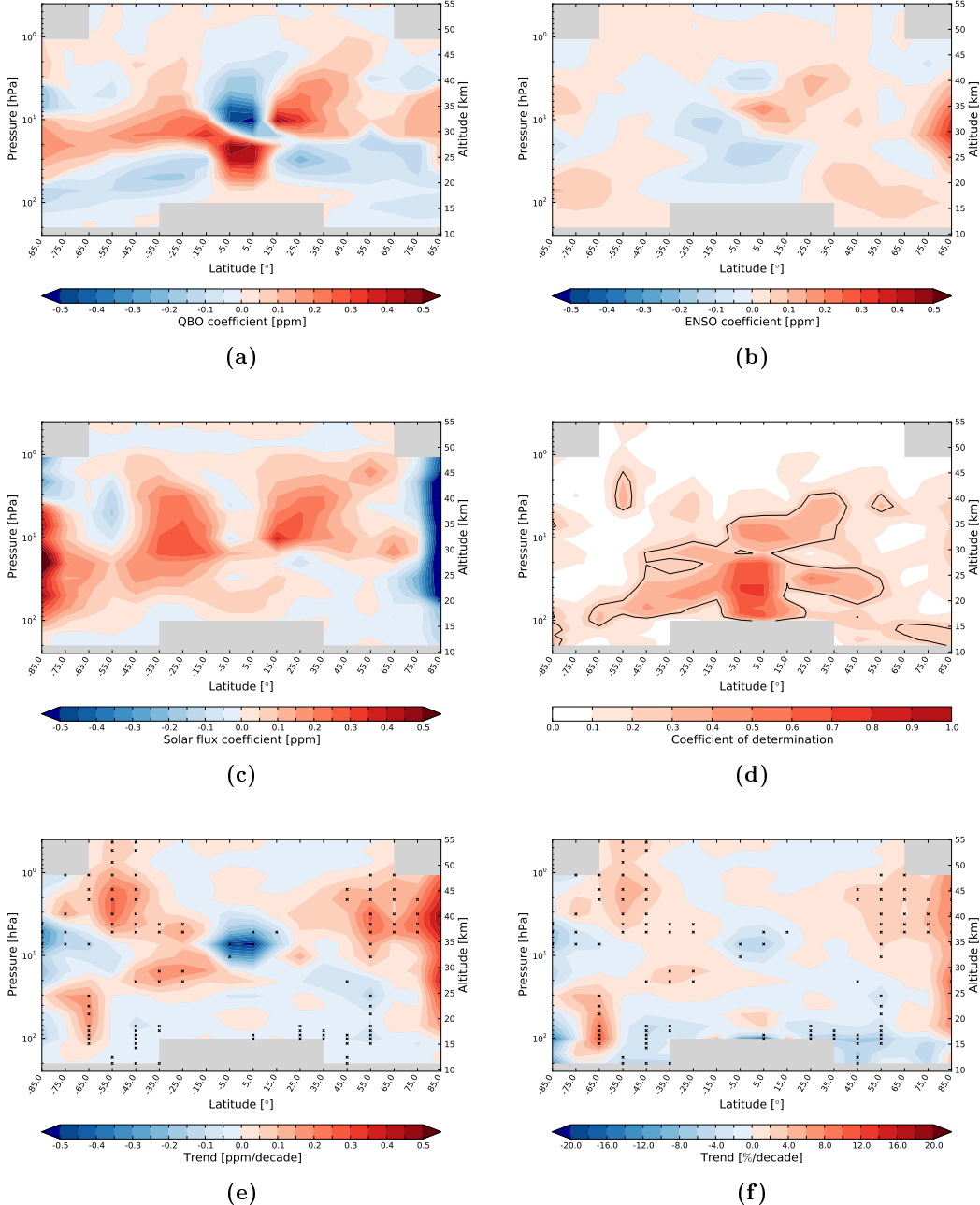
Figure C.2.: Results of the regression analysis for the RICH RS temperature data set in the recovery period 1997 to 2012. Same layout as Fig. C.1.
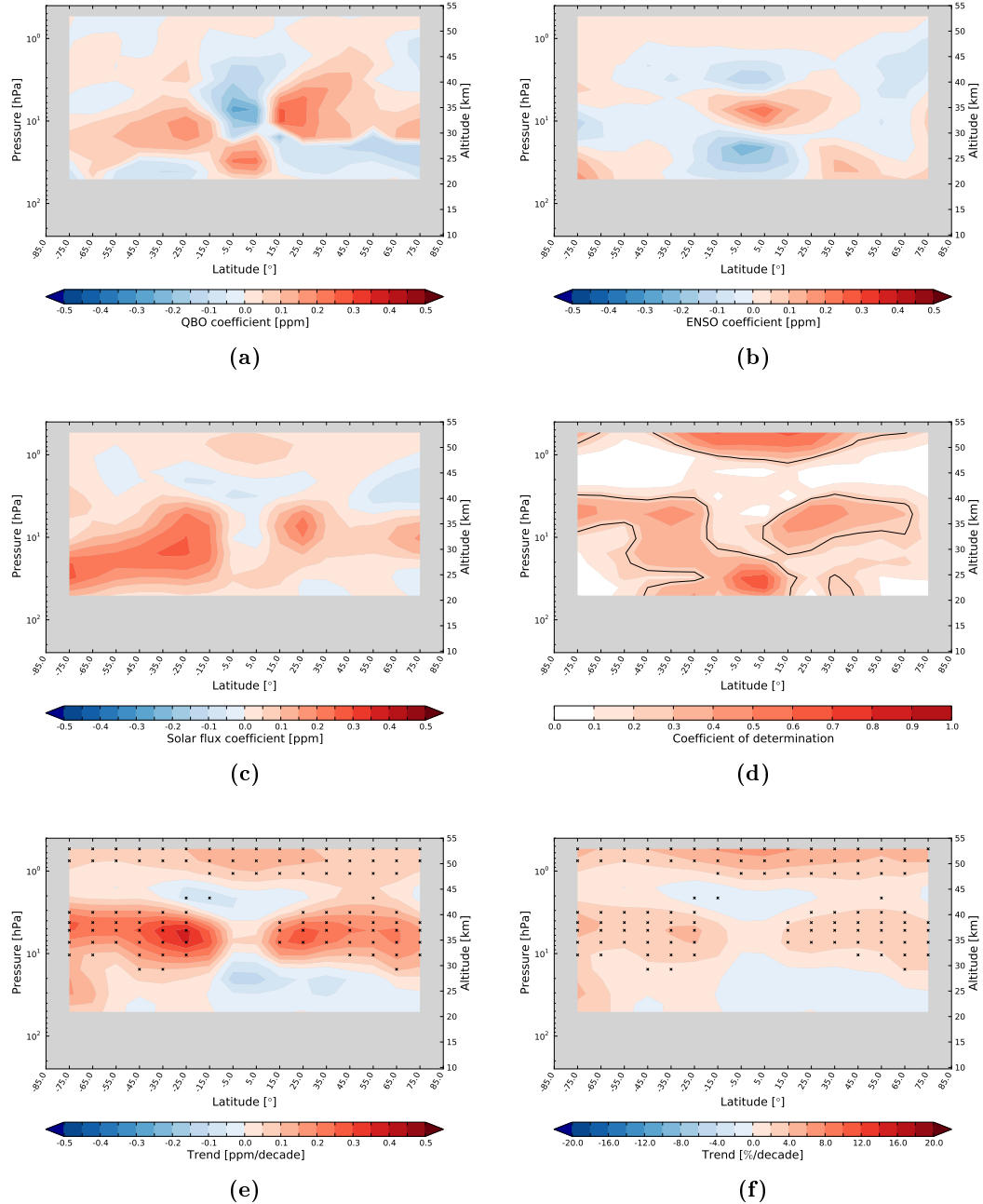
Figure C.3.: Results of the regression analysis for the ERA-Interim ozone data set in the recovery period 1997 to 2012. Same layout as Fig. C.1.

Figure C.4.: Results of the regression analysis for the GOZCARDS ozone data set in the recovery period 1997 to 2012. Same layout as Fig. C.1.
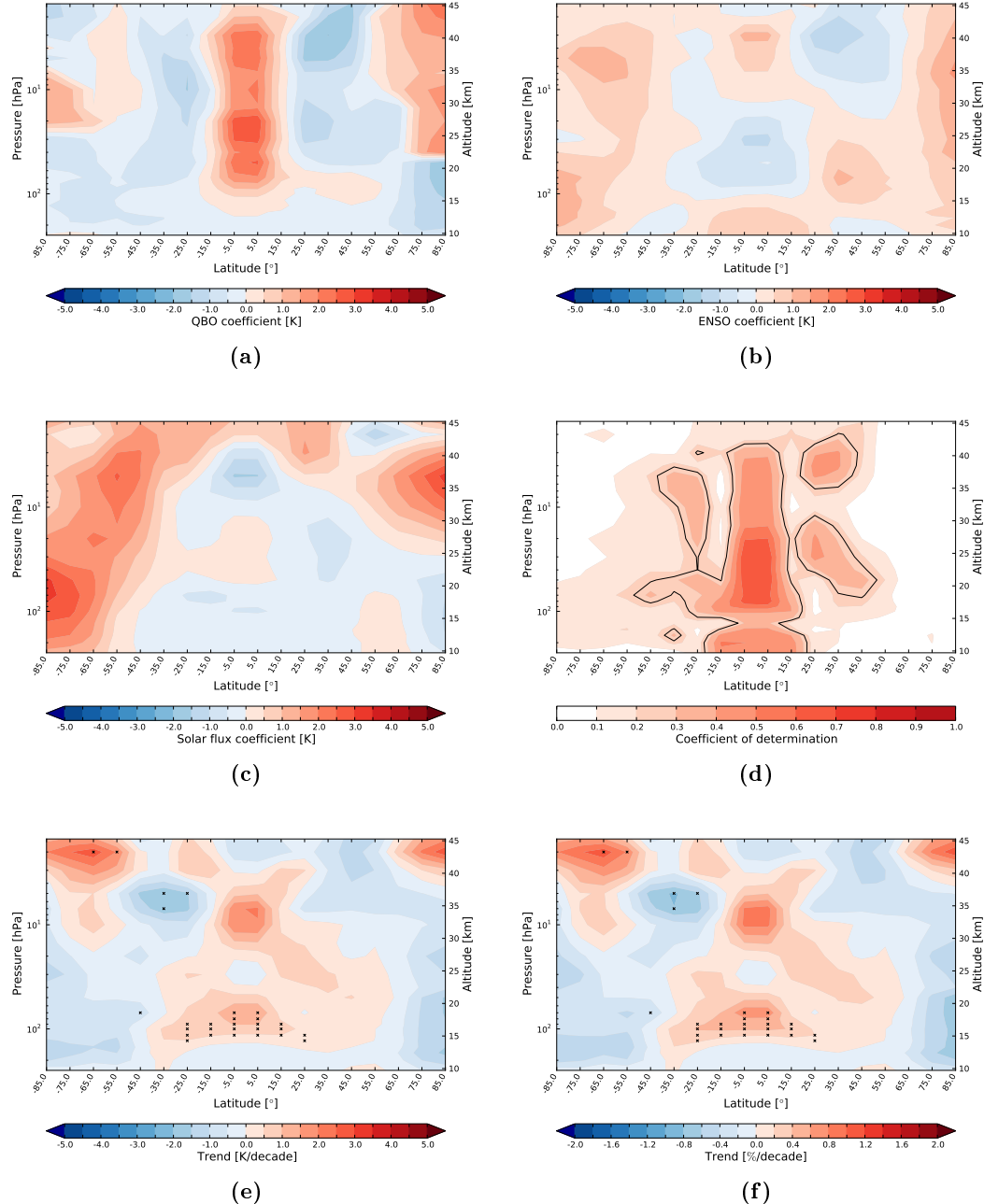
Figure C.5.: Results of the regression analysis for the NOAA SBUV ozone data set in the recovery period 1997 to 2012. Same layout as Fig. C.1.

D. RO period (2002 to 2012)
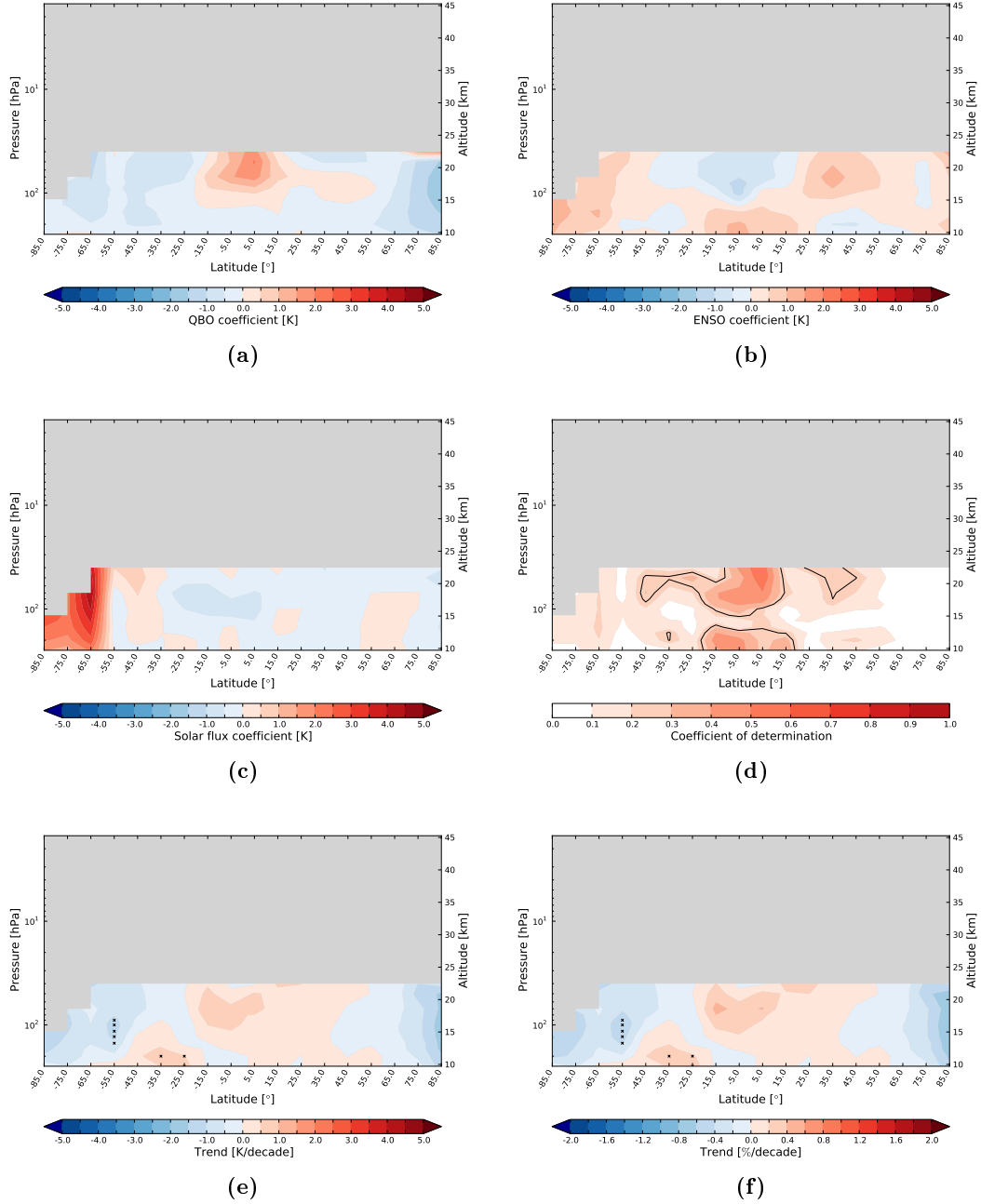
Figure D.1.: Results of the regression analysis for the RO temperature data set in the RO period 2002 to 2012. QBO (a), ENSO (b), and solar flux (c) coefficients as well as coefficient of determination (d). The solid line in (d) marks a determination value of 0.25. Absolute (e) and relative (f) trend, the × sign denotes regions significant on the 95 % level.
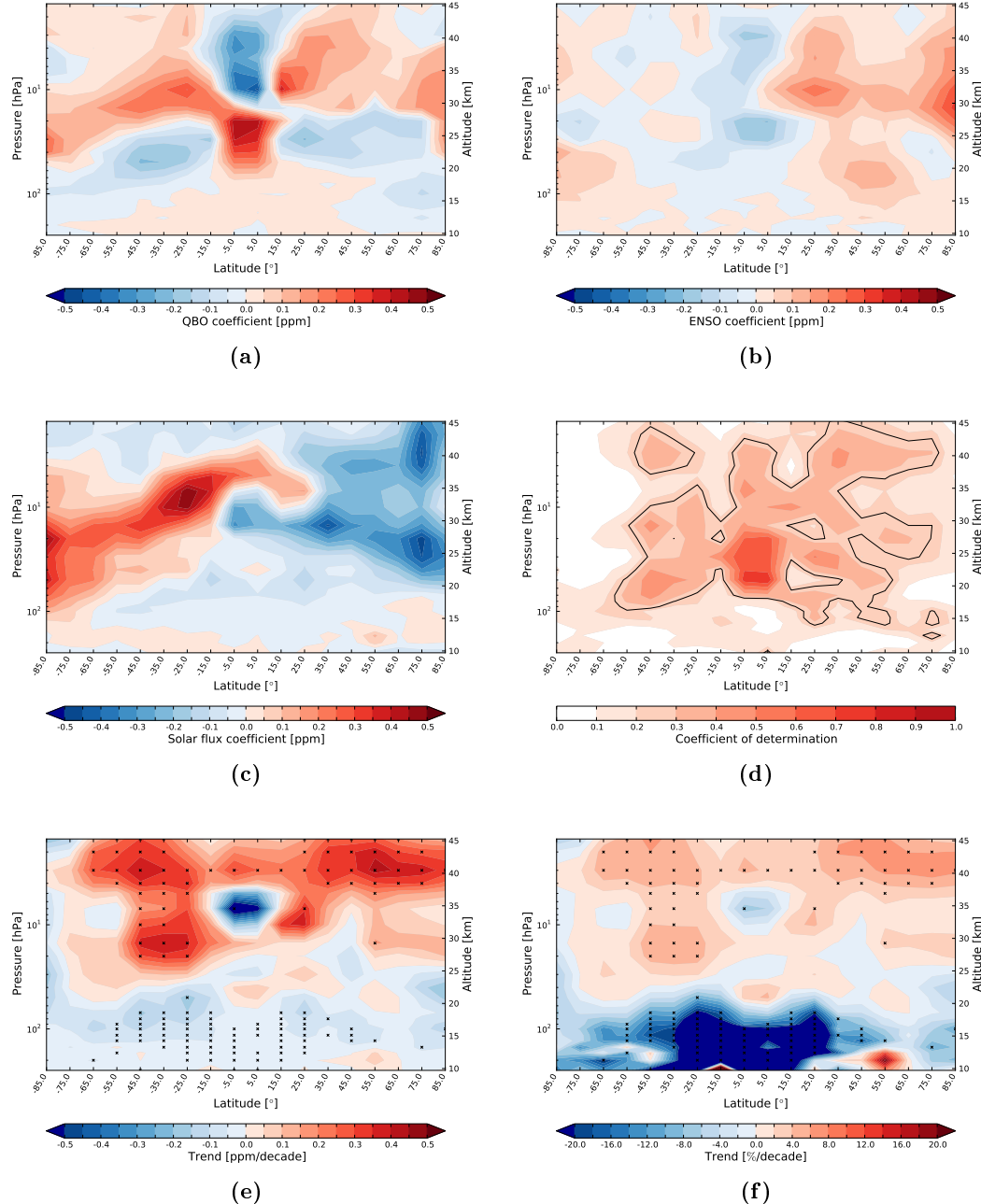
Figure D.2.: Results of the regression analysis for the ERA-Interim temperature data set in the RO period 2002 to 2012. Same layout as Fig. D.1.

(a)

(b)

(c)

(d)

(e)

(f)
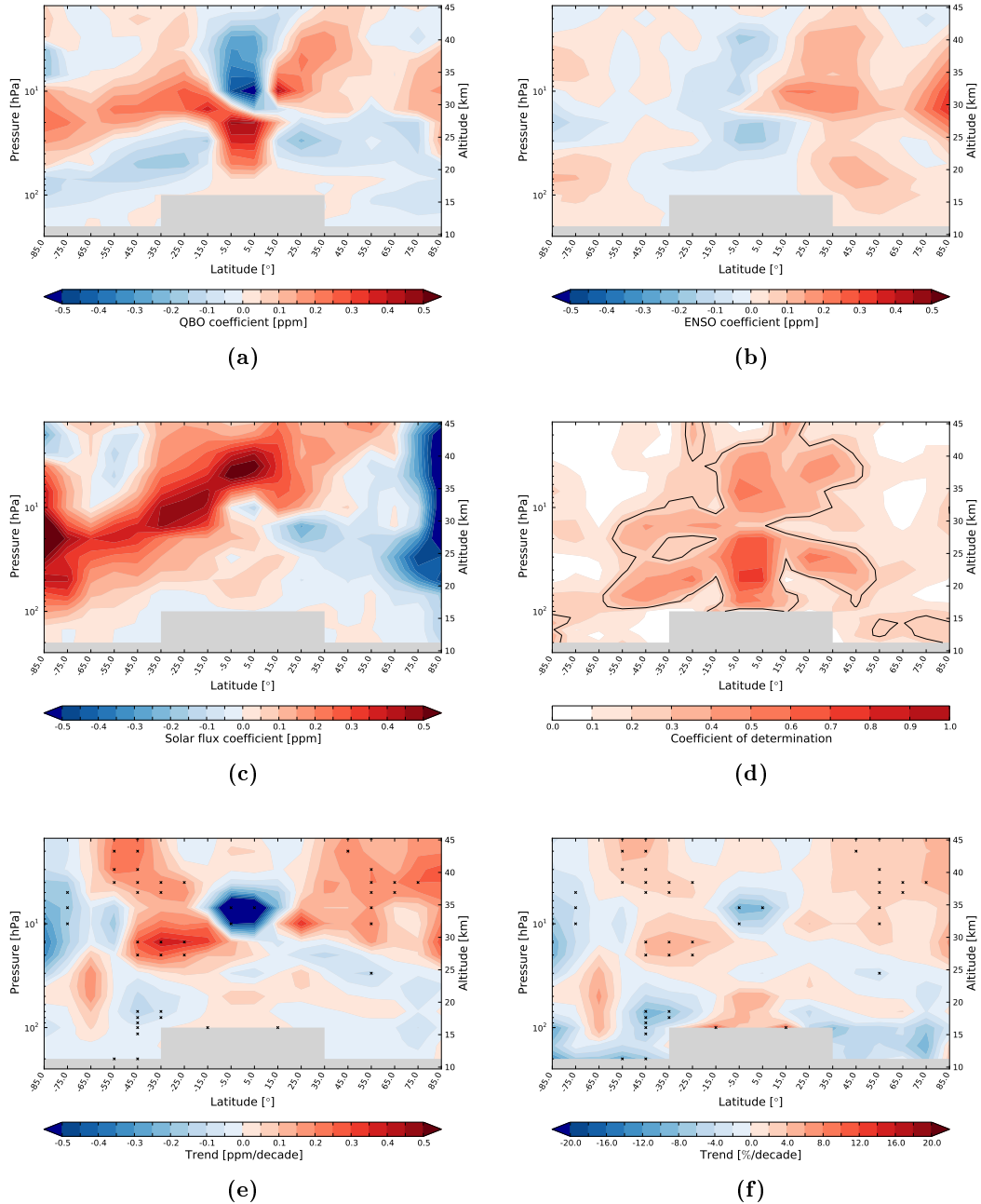
Figure D.3.: Results of the regression analysis for the RICH RS temperature data set in the RO period 2002 to 2012. Same layout as Fig. D.1.
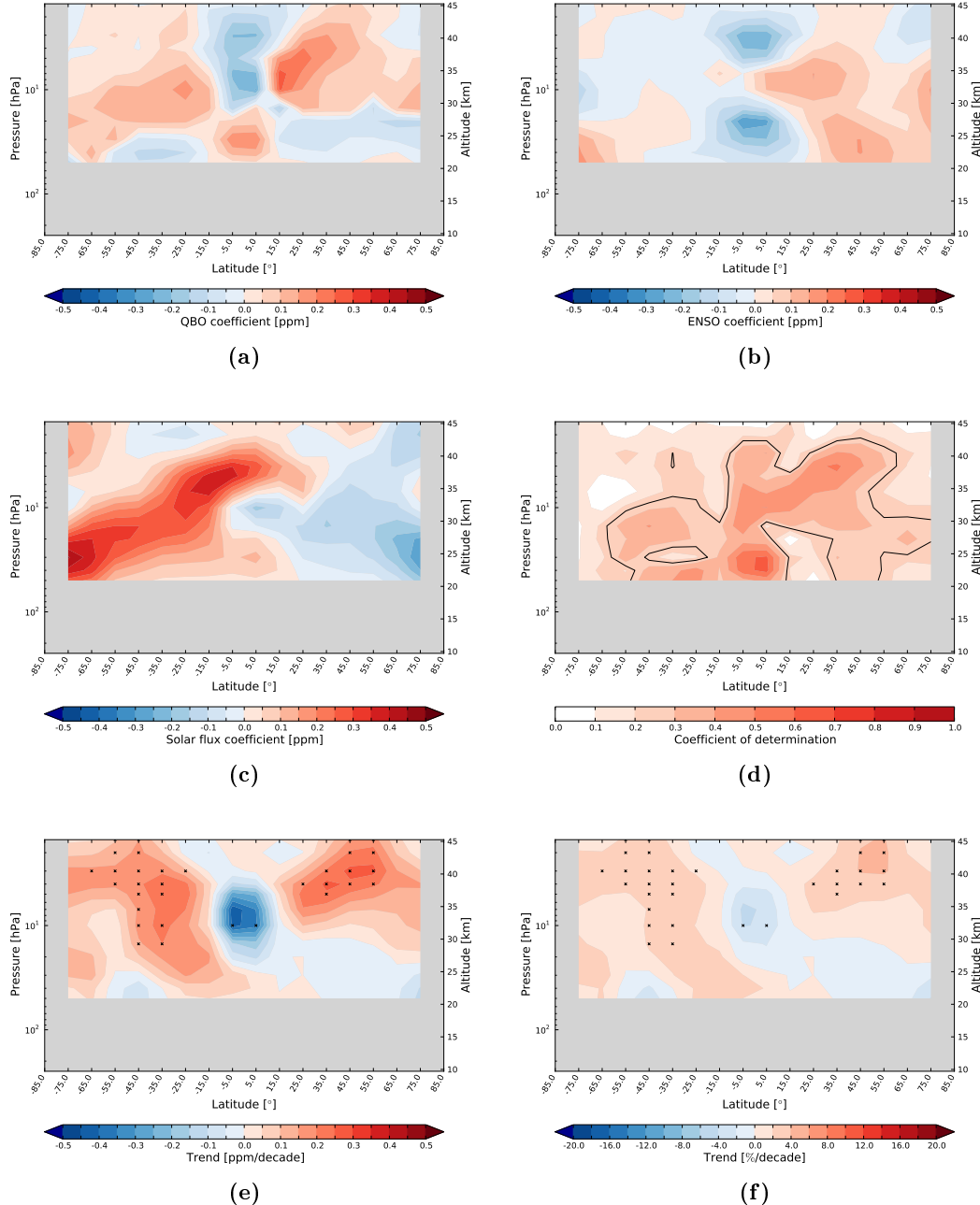
Figure D.4.: Results of the regression analysis for the HARMOZ ozone data set in the RO period 2002 to 2012. Same layout as Fig. D.1.
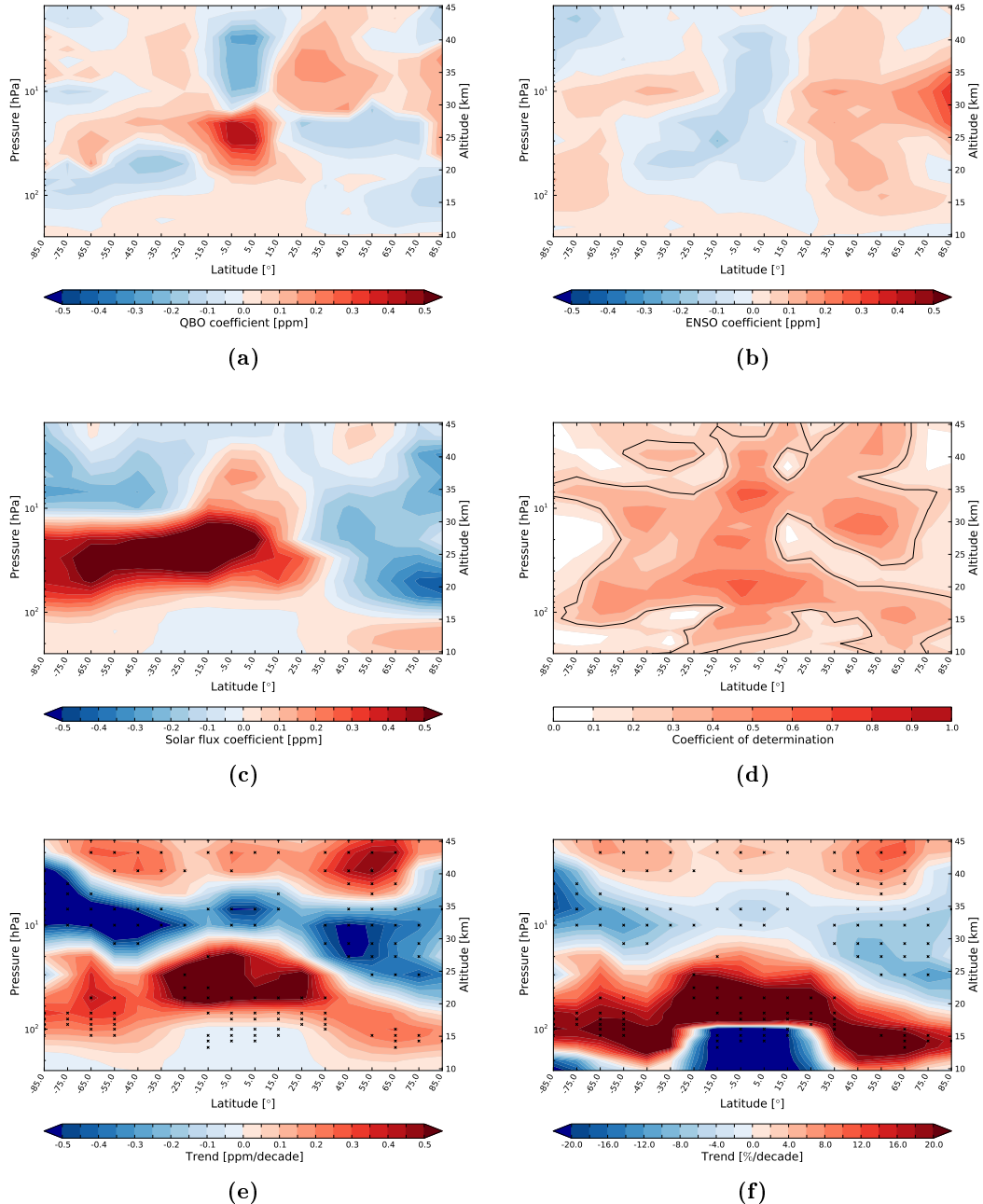
Figure D.5.: Results of the regression analysis for the GOZCARDS ozone data set in the RO period 2002 to 2012. Same layout as Fig. D.1.
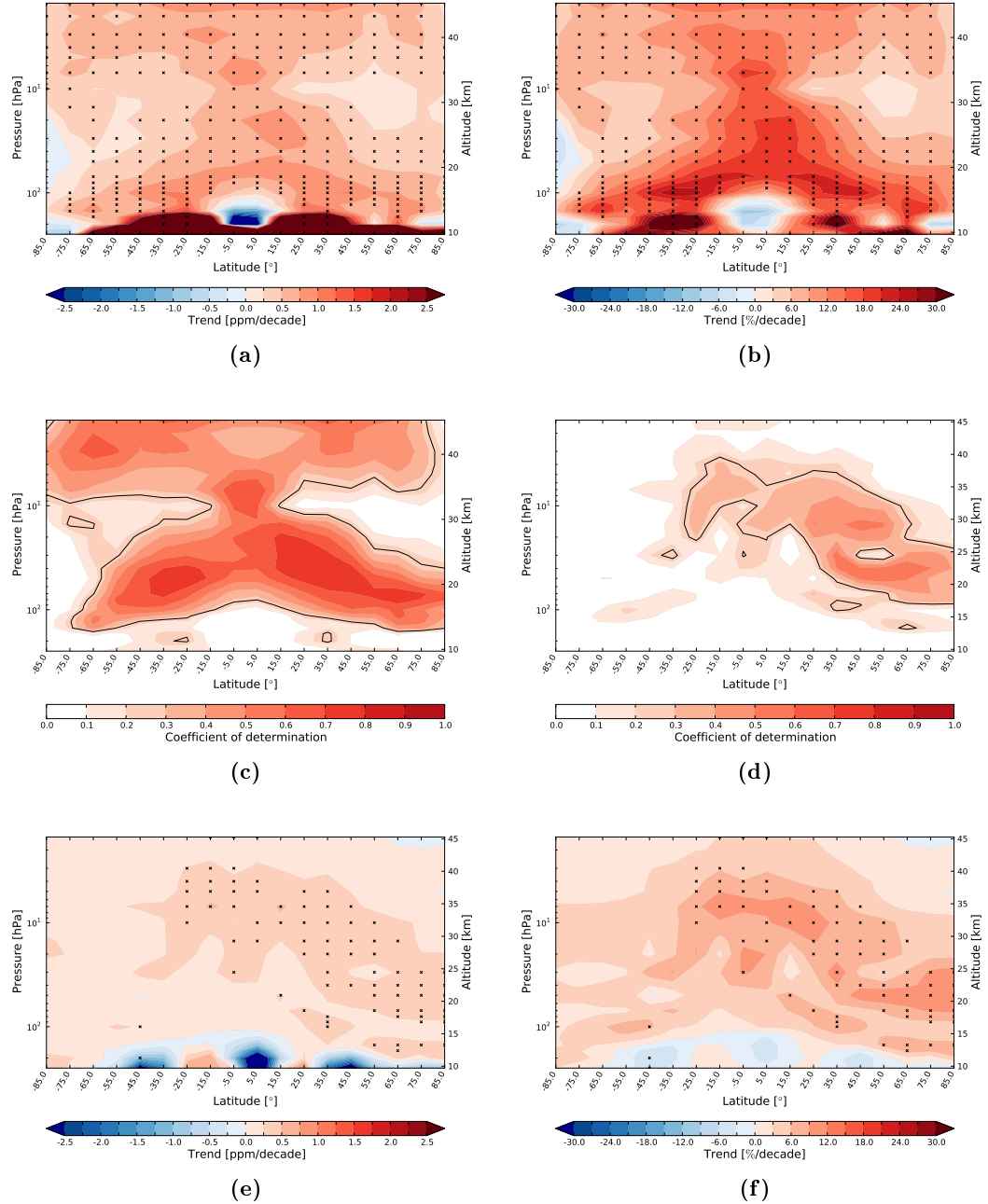
Figure D.6.: Results of the regression analysis for the NOAA SBUV ozone data set in the RO period 2002 to 2012. Same layout as Fig. D.1.

(a)

(b)

(c)

(d)

(e)

(f)

Figure D.7.: Results of the regression analysis for the ERA-Interim ozone data set in the RO period 2002 to 2012. Same layout as Fig. D.1.

Figure D.8.: Results of the regression analysis for the GOZCARDS and ERA-Interim water vapor data set in the RO period 2002 to 2012. Absolute trends for GOZCARDS (a) and ERA-Interim (e), relative trends for GOZCARDS (b) and ERA-Interim (f), as well as coefficient for determination for GOZCARDS (c) and ERA-Interim (d).

Abstract:

Investigating ozone and temperature related processes in the stratosphere is crucial for our understanding of the Earth's climate system. In recent decades satellite-based remote sensing has created new opportunities to measure physical properties of the free atmosphere with global coverage. Ozone and temperature evolution in the stratosphere are closely connected. The stratospheric temperature structure is mainly determined by the ozone concentration. But temperature changes also feed back, influencing ozone variability.

In this thesis stratospheric ozone evolution from three observational data sets for 1979 to 2012 is investigated. Corresponding temperature changes are derived from radiosonde and GPS Radio Occultation (RO) measurements, covering 1979 to 2012 and 2002 to 2012, respectively. For comparison also ERA-Interim reanalysis fields are considered. All data sets have high vertical resolution allowing for distinction of trends in different altitudes.

Three different time periods are investigated, using multiple linear regression to separate trend signals from natural variability, accounting for El Nino-Southern Oscillation, the Quasi-Biennial Oscillation, and solar flux variations. From 1979 to 1996 decreasing ozone concentrations and statistically significant cooling are found in large regions of the stratosphere. For the period 1997 to 2012 ozone shows signs of recovery especially in mid latitudes, mitigating further cooling in most of the stratosphere. In the period 2002 to 2012, with RO data availability, no significant trends are found due to the large natural variability.

Zusammenfassung:

Detaillierte Untersuchungen von Ozon und Temperatur in der Stratosphäre sind von entscheidender Bedeutung für unser Verständnis des globalen Klimasystems. In den letzten Jahrzehnten hat die satellitengestützte Fernerkundung neue Möglichkeiten eröffnet physikalische Größen in der freien Atmosphäre mit globaler Abdeckung zu messen. Die stratosphärische Temperatur ist eng mit Ozon verknüpft, da Absorption von Strahlung durch Ozon die wichtigste Wärmequelle in der Stratosphäre darstellt. Andererseits beeinflussen Temperaturänderungen durch Rückkopplungen auch den Ozonzyklus.

Diese Arbeit untersucht die Entwicklung von stratosphärischem Ozon von 1979 bis 2012 basierend auf drei Beobachtungsdatensätzen. Die Temperaturdaten stammen von Radiosonden- (1979 bis 2012) und GPS Radiookkultationsmessungen (2002 bis 2012). Für einen weiteren Vergleich werden auch Ozon und Temperatur Reanalysen von ERA-Interim untersucht. Alle Datensätze haben eine hohe vertikale Auflösung, was eine Unterscheidung von Trends in verschiedenen Höhen ermöglicht.

Mittels multipler linearer Regression werden in drei Zeitperioden Trends von natürlicher Variabilität, wie ENSO, QBO und Sonnenzyklus, getrennt. Von 1979 bis 1996 sank die Ozonkonzentration ebenso wie die Temperatur in weiten Teilen der Stratosphäre. Für den Zeitraum von 1997 bis 2012 zeigt Ozon Zeichen von Regeneration, insbesondere in mittleren Breiten was eine weitere Abkühlung der Stratosphäre größtenteils verhindert. Von 2002 bis 2012 wurden aufgrund der hohen natürlichen Variabilität keine statistisch signifikanten Trends gefunden.